

Relaxation de spin dans du CuCl massif
et des puits quantiques de CdTe



Hamid Rahimpour Soleimani

Thèse de doctorat de l'Université Louis Pasteur

Mars 2005

THÈSE DE DOCTORAT

Présentée à
l'U.F.R. des Sciences Physiques
de l'Université Strasbourg I

pour obtenir le titre de

**DOCTEUR DE L'UNIVERSITÉ LOUIS PASTEUR DE
STRASBOURG**

Spécialité Physique du Solide

Par
Hamid Rahimpour Soleimani

Sujet de la thèse:
**RELAXATION DE SPIN
DANS DU CuCl MASSIF
ET DES PUIITS QUANTIQUES DE CdTe**

Soutenue le 4 mars 2005 devant la commission d'examen

A. BIEBER	(Rapporteur interne)
I. PELANT	(Rapporteur externe)
D. SCALBERT	(Rapporteur externe)
B. HÖNERLAGE	(Directeur de thèse)
P. GILLIOT	(Examineur)

Remerciements

Ce travail de thèse a été effectué au sein du *Groupe d'Optique Non Linéaire et d'Optoélectronique de l'IPCMS de Strasbourg* sous la direction de Bernd Hönerlage.

Je tiens d'abord à remercier les membres de mon jury, D. Scalbert, I. Pelant et A. Bieber d'avoir accepté la charge d'être rapporteur de mon jury de thèse.

J'exprime toute ma gratitude à Bernd Hönerlage et Pierre Gilliot pour m'avoir permis d'effectuer ma thèse au sein de leur équipe. Votre pédagogie, vos connaissances scientifiques, m'ont fait passer, sous votre direction, quatre années de thèse enrichissantes.

Je tiens à exprimer ma profonde reconnaissance à Bernd Hönerlage, qui par ses qualités humaines a su être patient et à l'écoute et qui par son soutien et son savoir scientifique m'a permis de surmonter de nombreux problèmes.

Je suis très reconnaissant à Pierre Gilliot pour m'avoir aidé à comprendre certains processus, pour sa contribution à ce travail, et surtout pour ses encouragements lors de ma première année de thèse.

Mes remerciements vont également à Jean-Pierre Likforman avec qui j'ai réalisé avec plaisir des expériences qui constitue une part importante de mon travail.

J'ai tout particulièrement apprécié la précieuse aide que m'a apportée Olivier Cregut dans la solution des problèmes d'optique en général.

Steeve Cronenberger a été durant mes années de thèse mon coéquipier durant de nombreuses expériences. Son aide, ses nombreuses discussions enrichissantes et le temps qu'il a bien voulu dédié à la correction de ma présentation m'ont été précieux. Qu'il en soit remercié.

Je remercie également Mathieu Gallart pour nos diverses conversations et avoir relu mon mémoire.

Christelle Brimont a su animer le bureau par sa personnalité et je la remercie d'avoir été disponible pour mes nombreuses questions de français, pour la correction de ma présentation et pour sa patience lors des écoutes de cette dernière!!!

Je remercie aussi Janine Joseph, Jeannine Drivon et Béatrice Masson pour les nombreux services qu'elles m'ont rendus.

Il est très difficile de dresser une liste de toutes les personnes qui, de près ou de loin, m'ont accompagné durant cette thèse, sans risquer d'en oublier. Qu'ils sachent que je les en remercie.

Résumé

Nous présentons dans ce travail, une étude de la dynamique de population des polaritons-excitoniques et de leur spin dans le CuCl massif ainsi qu'une étude de la relaxation des spins électroniques dans des puits quantiques piézo-électriques de CdTe/CdMnTe.

Pendant la dernière décennie, les processus de relaxation du spin des électrons, des trous et des excitons ont été intensivement étudiés dans les semi-conducteurs III-V et II-VI et dans d'autres matériaux afin d'identifier les mécanismes responsables de l'évolution temporelle du moment angulaire total (ou pseudo-spin) d'un état excité. À notre connaissance, peu d'études ont été réalisées jusqu'ici sur des composés I-VII massifs. Il est important de comprendre cette dynamique puisque le pseudo-spin peut transporter et stocker l'information sur des échelles de temps assez longues, plus longues que la durée de cohérence d'une excitation élémentaire et comparable au temps de

vie.

Afin de déterminer le temps de relaxation de spin sur une échelle de temps sub-picoseconde dans les deux matériaux que nous avons étudiés, nous avons appliqué une technique pompe-sonde non-dégénérée. Cette technique est basée sur des mesures de changements, induits par une impulsion pompe, de la transmission d'une impulsion sonde retardée, avec un contrôle de la polarisation relative des deux faisceaux.

A : Expériences pompe-sonde non-dégénérées : CuCl

CuCl est un semi-conducteur à gap direct qui a une structure de bande particulièrement simple. Il montre des résonances excitoniques à une énergie de photon de l'ordre de 3,2 eV. Ces excitons sont dipolairement actifs et peuvent être excités par des faisceaux polarisés linéairement ou circulairement. De plus, dans CuCl, des biexcitons (ayant une énergie de liaison d'une trentaine de meV par rapport au continuum à deux excitons) peuvent être excités à partir de l'état fondamental du semi-conducteur. Ceci peut être réalisé par une absorption simultanée de deux photons ou bien par absorption successive

en créant d'abord des exciton-polaritons par une impulsion pompe : une deuxième impulsion fournie par un faisceau sonde peut alors induire la transition vers les biexcitons. Cette transition donne lieu à une absorption induite que nous analysons. Les règles de sélection indiquent que la transition est uniquement permise si les deux faisceaux pompe et sonde sont polarisés contra-circulairement. En utilisant cette technique, nous présentons les premières mesures des temps de relaxation de spin dans CuCl. De plus, l'évolution temporelle de l'absorption induite résolue spectralement nous fournit des informations sur l'évolution temporelle des populations des états excitoniques et biexcitoniques. Ceci se manifeste aussi dans la variation de la transmission qui peut passer d'une absorption induite à du gain, selon l'intensité de l'excitation que nous utilisons. Dans nos expériences, un faisceau pompe excite d'abord une population d'excitons polarisée en spin. Puis, nous mesurons l'absorption induite d'un faisceau sonde dont la direction de propagation est colinéaire avec celle du faisceau pompe mais qui est non dégénéré en fréquence. Ce faisceau est, lui aussi, polarisé circulairement et teste la transition exciton-biexciton.

Si les polaritons ont gardé leur polarisation de spin après leur excitation par l'impulsion pompe, une absorption induite n'apparaît que quand pompe et sonde sont polarisés contra-circulairement ($\sigma^+\sigma^-$). Si les polaritons créés par la pompe ont changé leur polarisation de spin, une absorption induite apparaît dans la configuration ($\sigma^+\sigma^+$). Ainsi, l'absorption induite fournit des informations sur l'état de spin de la population des exciton-polaritons. En comparant des résultats obtenus dans les deux configurations, nous déterminons l'évolution temporelle du spin des polaritons (caractérisé par la constante de T_s) ainsi que leur temps de vie (constante de temps T_r). Nous obtenons $T_s = 120 \pm 10$ ps et $T_r = 80 \pm 10$ ps. Ces valeurs demeurent valides si l'intensité d'excitation est inférieure à $0.5\text{mW}/\text{cm}^2$.

À des intensités plus élevées, la dynamique devient plus rapide. Nous montrons en particulier que si les dynamiques de relaxation du spin et de la population des exciton-polaritons peuvent être déterminées par des mesures d'absorption induite non-dégénérées, ceci est surtout possible dans la région du *spin-flip* située juste en dessous du polariton-

bottleneck où les polaritons étudiés sont assez lents et se propagent librement. Dans ces conditions, leur densité d'états et leur taux de collisions mutuel sont faibles et les effets de surface, auxquels leur dynamique est très sensible, ne les perturbent pas. Leur temps de relaxation de spin est long pour les températures en dessous de 40K et à basse intensité. Les processus de collision exciton-exciton n'influencent pas de manière significative ces longs temps de relaxation du spin. Par contre, de plus grandes énergies de photon, dans la région du *bottleneck*, la polarisation en spin du système de quasi-particules est principalement détruite par le fait que des biexcitons peuvent être créés : ils subissent alors une relaxation d'énergie en se recombinaison radiativement, générant une nouvelle population de polariton qui n'est plus polarisée en spin.

Comme nous le discutons dans notre travail, le fait que CuCl possède une structure de bande simple et des résonances électroniques bien séparés spectralement est techniquement utile mais pas nécessaire pour l'application de cette méthode de mesure. En général, il est

seulement nécessaire qu'un système possède des transitions, qui sont mutuellement permises ou interdites pour les différentes polarisations de spin.

Dans la suite de notre travail, nous présentons une discussion théorique du temps de relaxation de spin excitonique dans CuCl basée sur la méthode des invariants. La méthode des invariants permet de construire un hamiltonien électronique sans calculer explicitement les valeurs numériques des termes d'interactions. Nous considérons le centre de masse du vecteur d'onde Q de l'exciton ou ses produits (Q^n) comme perturbations internes. Pour les termes quadratiques en Q nous construisons un hamiltonien effectif pour les termes d'interaction, qui demeurent invariants pour toutes les opérations du groupe de symétrie (Γ_1) du cristal et par renversement du temps (K^+).

Nous envisageons en particulier le cas d'une expérience où les polaritons se propagent initialement dans la direction $[111]$. Pour une lumière polarisée circulairement, le hamiltonien est diagonal dans la base des états $|+1\rangle$ et $|-1\rangle$, qui ne sont donc pas couplés en-

tre eux. C'est à dire qu'aucun terme du hamiltonien, semblable à celui produit par un champ magnétique effectif, ne couple ces états. La dispersion des excitons transverses est également dégénérée dans la direction de haute symétrie [100], mais dans toutes les autres directions les états de polarisation circulaire $| +1 \rangle$ et $| -1 \rangle$ sont couplés.

Nous obtenons la représentation matricielle du hamiltonien pour la direction [110] lorsque la lumière est polarisée circulairement. Dans cette direction les états $| +1 \rangle$ et $| -1 \rangle$ sont couplés entre eux. Les termes correspondants dans le hamiltonien peuvent être vus comme induits par un champ magnétique effectif autour duquel précessent les spins. La relaxation du spin de l'exciton dans CuCl peut donc être due aux processus de collisions dans lesquels la direction de Q est changée. Les polaritons sont longitudinaux ou transverses en fonction de la direction de propagation et des projections de leurs composantes de polarisation sur les directions de propagation. Celles-ci changent à cause des processus de collision : un changement de la direction

de propagation mène immédiatement à la relaxation partielle du spin pour les polaritons circulairement polarisés. Une telle diffusion quasi-élastique étant possible pour les états polaritoniques, le taux de relaxation de spin de l'exciton est directement lié au temps de relaxation du vecteur d'onde de l'exciton.

B : Expériences pompe-sonde non-dégénérées : CdTe/CdMnTe

Nous avons mené une étude de la relaxation des spins électroniques similaire à celle décrite ci-dessus, dans des puits quantiques piézo-électriques de CdTe/CdMnTe. Pour accéder aux dynamiques individuelles des spins des électrons et des trous et non plus seulement à leur dynamique de relaxation conjointe à l'intérieur d'un exciton, deux types de techniques sont habituellement mis en œuvre. On utilise tout d'abord des échantillons dopés, qui contiennent un gaz des porteurs dont on veut mesurer la dynamique de spin. Le dopage modifie cependant les caractéristiques magnétiques et optiques de ce type de matériaux. On peut aussi appliquer un champ magnétique externe autour lequel les spins des porteurs vont précesser. Là aussi le champ

magnétique va influencer la dynamique qui nous intéresse. La technique que nous avons mise en œuvre s'affranchit de ces problèmes en mettant à profit le champ piézo-électrique présent dans un échantillon contenant des puits quantiques de CdTe. Normalement, la transition excitonique impliquant la bande électronique E_1 et de trou HH_1 les première sous-bande de trou lourd HH_1 est permise tandis que $E_1 - HH_2$ est interdite (HH_2 désigne la deuxième sous-bande du trou lourd). En présence du champ piézo-électrique que, cette transition E_1-HH_2 devient permise. Dans nos expériences, la transition $E_1 - HH_1$ est excitée par une impulsion pompe polarisée circulairement qui crée en conséquence une population d'excitons de spins bien définis. On compare les variations de transmission d'une impulsion test pour deux polarisations circulaires différentes (co- et contre-polarisée par rapport à la pompe) et sur les deux transitions excitoniques ($E_1 - HH_1$ et $E_1 - HH_2$). La variation de transmission est analysée en terme de remplissage de l'espace des phases. L'excitation et le test de deux transitions excitoniques différentes partageant une même bande électronique E_1 permettent ainsi de remonter aux dy-

namiques de relaxation individuelles des électrons et des trous. Nous obtenons un temps de relaxation de spin de 8 ps pour les électrons et de 40 ps pour les trous, tandis que le temps de recombinaison excitonique est estimé à 400 ps. Ce temps de relaxation de spin plus long pour les spins des trous que pour celui des électrons est expliqué d'une part par la diminution de l'interaction d'échange électron-trou dans les puits piézo-électriques due à la séparation spatiale des deux types de porteurs. D'autre part, il est dû, comme on le prévoit pour un puits quantique, à la levée de dégénérescence entre les bandes de trous lourds et légers induite par le confinement, affaiblissant ainsi un des principaux mécanismes de relaxation des trous.

Contents

1	Introduction	23
1.1	Thesis layout	24
2	Material description	28
2.1	CuCl : Valence and conduction band states	28
2.2	Excitons	31
2.3	Exciton polaritons	35
2.3.1	Polariton dispersion	36
2.4	Biexcitons	42
2.4.1	The polarization selection rules	44
2.4.2	Biexciton Luminescence	44
2.5	CdTe : Valence and conduction band states	48
2.6	CdTe /CdMnTe quantum wells	48
2.7	Band structure in strained quantum wells	50
2.8	Piezoelectric effect in (111)-oriented CdTe/CdMnTe strained quantum wells	54
2.8.1	The effect of internal electric fields	57
2.9	Spin relaxation	58
2.10	Longitudinal and transverse spin relaxation times	60
2.11	Spin relaxation mechanisms	62
2.11.1	Spin relaxation in semimagnetic semiconductors	64
3	General Experimental Methods	66
3.1	Pump-Probe spectroscopy	66
3.2	The laser source	68

3.2.1	Femtosecond pulse generation	68
3.2.2	Ultrafast laser system	70
3.2.3	Group Velocity Dispersion Compensation	71
3.3	Pulse-Duration Measurement	72
3.4	Cryostat	73
3.5	The experimental set-up and sample: CuCl	75
3.6	The experimental set-up and sample: CdTe/CdMnTe multiple quantum well	77
4	Spin population and propagation dynamics of polaritons in CuCl	80
4.1	A new method to determine the spin-relaxation dynamics	80
4.2	Region A (Surface effects)	86
4.2.1	Modeling of region A (Surface effects)	88
4.3	Region B (Spin-flip region)	89
4.3.1	Modeling of experimental results for region B (Spin-flip region)	90
4.4	III-C Region C-I (The polariton bottleneck region)	93
4.4.1	Modeling of experimental results for region C-I (polariton bottleneck)	94
4.5	Region C-II (Gain)	95
4.6	Absorption bleaching and phonon replica	98
4.7	Conclusions	99
5	Spin relaxation and symmetry breaking effects	102
5.1	The invariant expansion method of an effective Hamiltonian	102
5.2	Formulation of invariant expansion	107
5.3	Exciton-spin relaxation in CuCl	112
5.4	Conclusions	117
6	Experimental Results : CdTe quantum wells	119
6.1	Introduction	119
6.2	Excitonic optical nonlinearities in multiple quantum wells	121
6.2.1	Optical nonlinearities due to screening	121
6.2.2	Optical nonlinearities due to the bandfilling effect	122

6.3	Principle of the experiment	124
6.4	Conclusions	133
7	Conclusions	134
A	D'yakonov-Perel mechanisms	139
B	Elliott-Yafet mechanisms	143
C	Bir-Aronov-Pikus mechanism	146
D	Spin relaxation mechanisms in quantum wells	149
D.1	Symmetric quantum well	149
D.2	Asymmetric quantum well	153
E	Hyperfine interaction	155

List of Figures

2.1	Arrangement of atoms in CuCl crystals.	29
2.2	Schematic band structure of CdTe and CuCl near the Γ point, at the center of the Brillouin zone.	29
2.3	The polariton dispersion curve in CuCl.	39
2.4	The polariton group velocity calculated from the dispersion.	41
2.5	Elementary process leading to biexciton luminescence.	45
2.6	The luminescence spectra of our sample (CuCl) at 5K. Annihilation of biexciton in CuCl give rise to M_T and M_L emissions.	47
2.7	Level scheme for a single quantum well of CdTe sandwiched between two CdMnTe barriers.	49
2.8	Schematic representation of unstrained CdTe and CdMnTe and strained CdTe\CdMnTe	50
2.9	Splitting of the energy in the strained-layer CdTe/CdMnTe quantum wells due to a hydrostatic deformation potential and shear deformation potentials	51
2.10	Polarization, electrical charges, and fields in a strained B layer on an A unstrained layer.	55
2.11	The effect of strain-induced polarization fields on the energy levels and the bands of a CdTe/CdMnTe quantum well.	56
3.1	Schematic diagram of the laser.	69
3.2	Schematic setup of an autocorrelation technique for measuring the pulse duration.	73
3.3	The vacuum loading MicrostatHe cryostat.	74

LIST OF FIGURES

3.4	The pump pulse spectral intensity, in resonance with the exciton transition, and the probe pulse covers the exciton-biexciton transition for experimentals on CuCl.	75
3.5	Experimental setup : CuCl	77
3.6	Absorption profile of the CdTe/CdMnTe multiple quantum well structure at the $HH_1 - E_1$ and $HH_2 - E_1$ transition and the pump pulse spectral intensity, in resonance with the $HH_1 - E_1$ transition	78
3.7	The experimental set-up: CdTe/CdMnTe multiple quantum wells	78
3.8	The CdTe/CdMnTe multiple quantum well consisting of 40 periods of 10.1-nm-wide CdTe quantum wells, with 95 nm $Cd_{0.83}Mn_{0.17}Te$ barriers.	79
4.1	Linear transmission spectrum of CuCl at 5 K.	81
4.2	Level scheme of excitons and biexcitons together with the optical transitions used in the experiments (pump σ^+ , probe σ^+ or σ^-).	82
4.3	Differential transmission of a CuCl pletelet and luminescence spectrum at 4K ($\sigma^+\sigma^-$ configuration).	84
4.4	Differential transmission of a CuCl pletelet and luminescence spectrum at 4K ($\sigma^+\sigma^+$ configuration).	85
4.5	Polariton dispersion $E(K)$ in the vicinity of the bottleneck region calculated from the parameters of CuCl using the one oscillator model and different relaxation times and the probability of biexciton formation.	87
4.6	Induced transmission changes for the $\sigma^+\sigma^+$ configuration, for the $\sigma^+\sigma^-$ configuration, and their sum as function of time delay between the pulses. The photon energy of the probe beam is $E_t = 3.178\text{eV}$. The polaritons of the pump pulse which are tested have photon energies $E_p = 3.194\text{eV}$	89
4.7	Induced transmission changes for the $\sigma^+\sigma^+$ configuration, for the $\sigma^+\sigma^-$ configuration, for $E_t = 3.1715\text{eV}$ (corresponding to $E_p = 3.2005\text{eV}$) together with the fit.	90

LIST OF FIGURES

4.8	Sum and difference of induced transmission changes for the $\sigma^+\sigma^+$ configuration, for the $\sigma^+\sigma^-$ configuration, for $E_t = 3.1715\text{eV}$ (corresponding to $E_p = 3.2005\text{eV}$) together with the fit using Eq. 4.3. A rate of sum/difference is shown in the inset.	91
4.9	Induced transmission changes for the $\sigma^+\sigma^+$ configuration and for the $\sigma^+\sigma^-$ configuration for $T=40\text{K}$ and $E_t = 3.1777\text{eV}$ together with the fit.	92
4.10	Induced transmission changes for the $\sigma^+\sigma^+$ configuration and for the $\sigma^+\sigma^-$ configuration for $T=4\text{K}$ and $E_t = 3.1655\text{eV}$ (corresponding to $E_p = 3.2066\text{eV}$) together with the fit	94
4.11	Induced transmission changes for the $\sigma^+\sigma^+$ configuration a) and for the $\sigma^+\sigma^-$ configuration b) for $T=4\text{K}$ and $E_t = 3.16002\text{eV}$ (corresponding to $E_p = 3.2112\text{ eV}$) together with the fit using Eq.4.7.	97
6.1	Scheme of the energy levels involved in the experiment and optical selection rules.	125
6.2	Differential transmission spectra for same and opposite circular polarizations of the pump and probe pulses.	127
6.3	Differential transmission signal after spectral integration of the $HH_1 - E_1$ and $HH_2 - E_1$ transitions as a function of the pump-probe time-delay. Fits of data are shown as thin lines.	131

List of Tables

2.1	Correlation between atomic s- and p-level conduction- and valence band-symmetries, for the point group T_d	28
5.1	Transformation properties of different quantities in crystals with T_d point-group symmetry. K^+ and K^- denote symmetry under time reversal, see text.	103
5.2	Multiplication table for the group T_d	105
5.3	Multiplication scheme for the different components of irreducible representations in crystals with T_d -symmetry.	106

Chapter 1

Introduction

The electron spin is becoming increasingly important in electronics. New devices, now generally referred to as spintronics (1; 2; 3), exploit the ability of conduction electrons in metals and semiconductors to carry spin-polarized currents. Possible applications of spintronics include high speed magnetic filters, sensors, quantum transistors, etc. In addition, semiconductor spintronics may also allow us to develop the basic elements needed for quantum computation and communication (spin qubits, quantum gates, etc (4)). More fundamental research will, however, be needed before practical spintronic devices can be demonstrated, as much remains to be understood about spin coherence and relaxation, spin dynamics, and spin injection and transport.

Electron- and hole-spin relaxation in semiconductors has been investigated for more than four decades. In bulk and heterostructure semiconductors, mechanisms of electron- and hole-spin relaxation have been studied, both theoretically and experimentally (see reference (2) and references cited therein). In spite of this intense activity concerning electrons or holes in semiconductors, exciton-spin (pseudo-spin) relaxation has rarely been studied. For resonantly created excitons, a specific theory of spin relaxation including the excitonic effect is needed (5).

On excitation, semiconductors can exhibit large changes in their optical prop-

erties near the band edge, where excitonic effects are predominant. Excitons are the lowest lying electronic excitations in semiconductors. They can be described as a bound state of an electron in the conduction band and a hole in a valence band, interacting via Coulomb interaction. Excitons are considered as quasiparticles: they have a wave vector dependent energy and possess an internal structure, characterized by their total angular momentum (or pseudo-spin) which combines the individual electron and hole spin states. Dispersion, internal structure, and resulting residual (exchange) interactions are mainly determined by the crystal symmetry and the one-particle band structure. When compared to the spin of free carriers, the exciton pseudo-spin is not defined in a unique way for all excitons but may depend on the direction of propagation of the excitons. As we will see, this has important consequences for the spin relaxation in scattering processes. The keynote of this thesis is to show that the spin relaxation dynamics of quasiparticles can be determined from induced absorption measurements. This is possible if transitions from degenerate states to other states are mutually allowed or forbidden for circularly polarized light with different helicities. This is illustrated here in bulk CuCl crystals and CdTe/CdMnTe quantum wells.

1.1 Thesis layout

The thesis layout with a brief summary for each chapter is as follows:

In chapter two, we will briefly spell out the optical properties, band structure, excitonic and biexcitonic properties of CuCl and the optical properties of strained CdTe/CdMnTe. To provide the basis for the analysis of our experimental results, it is necessary to study the basic optical properties of these materials.

We start with the direct-band gap semiconductor CuCl. The reason is that it is useful to study simple systems showing well-resolved excitonic lines, which

are already understood in a linear (or weakly nonlinear) regime, and CuCl is such a material. It has a direct band gap and a very simple structure with bands of symmetry Γ_7 and Γ_8 for the two upper valence bands and Γ_6 for the conduction band. Two strong optically allowed exciton series are observed in absorption. Furthermore, two excitons can couple and form biexcitons. The symmetry of the exciton and biexciton states are well known and transition between the states are allowed. Binding energies of excitons and biexcitons and the spin-orbit coupling are large. All this makes CuCl a model semiconductor in which only a few number of well separated energy levels have to be considered. Because of strong coupling with light, excitons show a pronounced polariton character. The exciton-photon interaction in semiconductors is attractive for potential applications to optoelectronic devices. We will review these effects in section 2.3 and 2.4, respectively.

We will next study general properties of strained CdTe/CdMnTe quantum wells. Optical spectroscopy of excitons in II-VI semiconductor quantum wells has attracted increasing interest due to the technological progress in the growth of the respective heterostructures and their possible applications. Large piezoelectric fields appear when strained heterostructures are grown along a polar axis in semiconductors with zinc-blende structure. This field strongly modifies the band structure and induces a spatial separation of electrons and holes (see section 2.8 and chapter 6). Finally, we will review the concept of mechanisms of spin relaxation in section 2.9 and 2.10. Readers who are interested in more details are to refered the Appendixes A, B, C, D and E.

In chapter three, we will discuss the general experimental techniques and apparatus which have been applied to the study of population and spin dynamics in bulk and multiple quantum well semiconductors.

In chapter four, we present a new method to determine the polariton spin-relaxation dynamics. In this chapter we discuss the dynamics of a system consisting of exciton polaritons and biexcitons in bulk CuCl samples on a subpicosecond time scale. The polariton dispersion curve is scanned in a pump and probe experiment by looking at different excitation and detection wavelengths. This allows us to determine the influence of the polariton wave vector on polariton-spin relaxation processes and on their overall population dynamics. We evaluate how the optical properties close to the exciton resonance develop in time from induced absorption to gain, depending on the wavelength and the intensity of excitation. This allows us to determine the polariton- and biexciton-population relaxation dynamics inside the bottleneck spectral region, their spin dynamics, and reveals the importance of propagation effects.

In chapter five, the invariant expansion of an effective Hamiltonian is used to establish the exciton - spin (pseudo - spin) relaxation processes for systems with a simple band structure. Since dipole active excitons couple to the light field, the wave functions of transverse or longitudinal excitons have to be defined with respect to their direction of propagation. Then scattering processes, in which the direction of propagation is changed, lead to a relaxation of the pseudo - spin. In addition, compared to the situation at the Γ -point, the point group symmetry of a crystal is broken at finite wave vectors. As a consequence, the exchange interaction between electrons and holes in conjunction with the center-of-mass motion of the excitons can mix different states. Depending on the propagation direction, dipole active exciton states with opposite circular polarization can become coupled, resulting into a spin dephasing. We consider exchange terms linear, quadratic, and cubic in the wave vector of the propagating quasiparticles and we discuss their importance for spin relaxation mechanisms observed in CuCl and

shown in chapter four.

In chapter six we present direct measurements of the electron- and hole-spin relaxation times in undoped piezoelectric CdTe/CdMnTe multiple quantum wells. In this case, two heavy-hole exciton transitions are sharing a common electronic energy level in the conduction band. Comparing the dynamics of these transitions, studied in a non-degenerate pump-probe experiment, enables us to determine the spin relaxation time of the two types of carriers.

Chapter 2

Material description

2.1 CuCl : Valence and conduction band states

Copper chloride is a I-VII compound semiconductor. Such crystals have in general large energy gaps, $E_g \gtrsim 3\text{V}$ (6), and are transparent to visible radiation. Below 400°C , the crystal structure of CuCl is zinc blende, like GaAs, with T_d point-group symmetry (see table 2.1).

Table 2.1: Correlation between atomic s-and p-level conduction- and valence band-symmetries, for the point group T_d

Atomic level	Orbital angular momentum l	Irreducible representation	Degeneracy	Spin	Total angular momentum j	Irreducible representation	Degeneracy
s	0	Γ_1	1	1/2	1/2	Γ_6	2
					3/2	Γ_8	4
p	1	Γ_5	3	1/2	1/2	Γ_7	2

Fig. 2.1 shows the arrangement of atoms in CuCl. The lattice constant of CuCl at room temperature is $a=0.5406\text{ nm}$. A schematic band structure is shown in Fig 2.2. Extrema of the lowest conduction band and the highest valence

2.1 CuCl : Valence and conduction band states

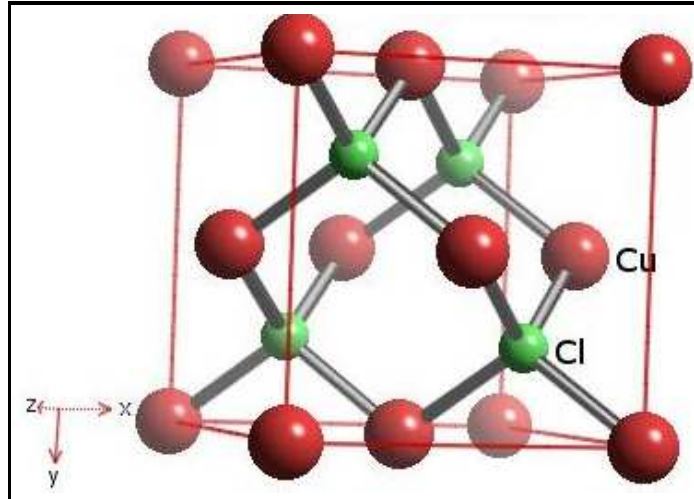


Figure 2.1: Arrangement of atoms in CuCl crystals.

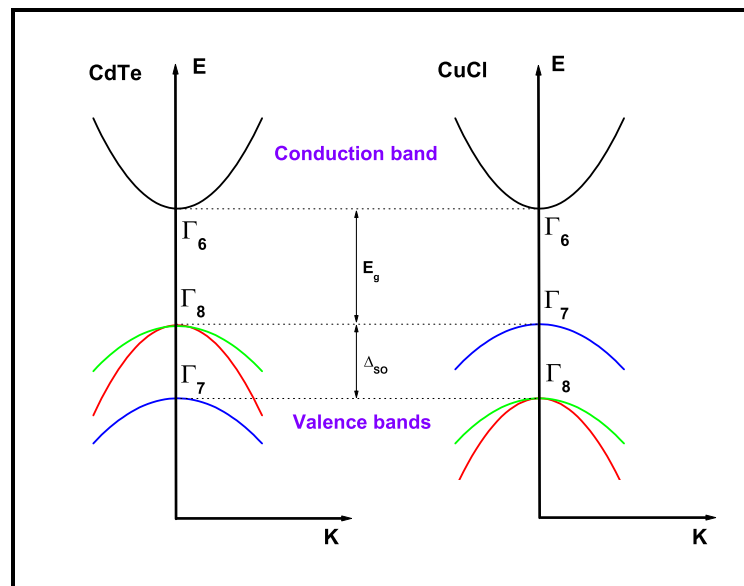


Figure 2.2: Schematic band structure of CdTe and CuCl near the Γ point. CdTe shows the normal ordering of the upper valence bands, the fourfold degenerate Γ_8 band has a higher energy than the twofold degenerate Γ_7 band. Apart from $K = 0$, the degeneracy of the Γ_8 band is lifted.

2.1 CuCl : Valence and conduction band states

band are located at the center of the Brillouin zone, at the Γ point. Because of lack of inversion symmetry, no parity can be assigned to the bands at $K = 0$. The conduction band is derived from s orbitals of the Cu 4s levels. The highest valence bands, having irreducible representations Γ_7 and Γ_8 respectively, are derived principally from 3d orbitals of Cu ions, with about 24% admixture of p-orbitals of the chlorine ion (7). The energy separation Δ_{so} between the two upper valence bands due to spin-orbit coupling is 93.4meV (8). The ordering of the valence bands in CuCl is different from that of typical zinc blende materials, such as the compounds CdTe or GaAs (see Fig. 2.2). The twofold degenerate Γ_7 band has a higher energy than the fourfold Γ_8 band. This is due to the strong d-like character of the valence bands, which inverts the sign of the spin-orbit splitting (9) .

CuCl has strong exciton absorption lines and large absorption coefficients $\alpha \sim 10^5 \text{ cm}^{-1}$ (see Fig. 4.1) . The conduction band at $K = 0$ has Γ_6 symmetry and can be written as

$$\begin{aligned}\phi_1^c\left(\frac{1}{2}\right) &= |S \uparrow\rangle \equiv |\alpha^e\rangle \\ \phi_2^c\left(\frac{-1}{2}\right) &= |S \downarrow\rangle \equiv |\beta^e\rangle,\end{aligned}\tag{2.1}$$

or in matrix form

$$\phi_1^c\left(\frac{1}{2}\right) = S \begin{pmatrix} 1 \\ 0 \end{pmatrix} \quad \phi_2^c\left(\frac{-1}{2}\right) = S \begin{pmatrix} 0 \\ 1 \end{pmatrix}$$

where S can be identified with the 4s function originating from Cu. The wave function of the valence-band states at $K = 0$ with Γ_7 symmetry have the form

$$\begin{aligned}\phi_5^v\left(\frac{1}{2}; \frac{1}{2}\right) &= \frac{1}{\sqrt{3}} | (X + iY) \downarrow + Z \uparrow \rangle \\ \phi_6^v\left(\frac{1}{2}; \frac{-1}{2}\right) &= \frac{1}{\sqrt{3}} | (X - iY) \uparrow - Z \downarrow \rangle\end{aligned}\tag{2.2}$$

or in matrix form

$$\phi_5^v\left(\frac{1}{2}; \frac{1}{2}\right) = \frac{1}{\sqrt{3}} \begin{pmatrix} Z \\ X + iY \end{pmatrix} \quad \phi_6^v\left(\frac{1}{2}; \frac{-1}{2}\right) = \frac{1}{\sqrt{3}} \begin{pmatrix} X - iY \\ -Z \end{pmatrix}$$

The wave function of the valence-band states at $K = 0$ with Γ_8 symmetry have the form

$$\begin{aligned} \phi_1^v\left(\frac{3}{2}; \frac{3}{2}\right) &= \frac{1}{\sqrt{2}} | (X + iY) \uparrow \rangle \\ \phi_2^v\left(\frac{3}{2}; \frac{1}{2}\right) &= \frac{1}{\sqrt{6}} | (X + iY) \downarrow -2Z \uparrow \rangle \\ \phi_3^v\left(\frac{3}{2}; \frac{-1}{2}\right) &= \frac{1}{\sqrt{6}} | (X - iY) \uparrow +2Z \downarrow \rangle \\ \phi_4^v\left(\frac{3}{2}; \frac{-3}{2}\right) &= \frac{1}{\sqrt{2}} | (X - iY) \downarrow \rangle, \end{aligned} \quad (2.3)$$

or in matrix form

$$\begin{aligned} \phi_1^v\left(\frac{3}{2}; \frac{3}{2}\right) &= \frac{1}{\sqrt{2}} \begin{pmatrix} X + iY \\ 0 \end{pmatrix} & \phi_2^v\left(\frac{3}{2}; \frac{1}{2}\right) &= \frac{1}{\sqrt{6}} \begin{pmatrix} -2Z \\ X + iY \end{pmatrix} \\ \phi_3^v\left(\frac{3}{2}; \frac{-1}{2}\right) &= \frac{1}{\sqrt{6}} \begin{pmatrix} X - iY \\ +2Z \end{pmatrix} & \phi_4^v\left(\frac{3}{2}; \frac{-3}{2}\right) &= \frac{1}{\sqrt{2}} \begin{pmatrix} 0 \\ X - iY \end{pmatrix} \end{aligned}$$

Where X, Y, and Z denote orbitals, which transform as the components of the position vector \vec{r} .

2.2 Excitons

When computing the minimum energy required to excite an electron-hole pair in a semiconductor, it is necessary to include the Coulomb attraction between the conduction-band electron and the valence-band hole. The inclusion of the Coulomb interaction results in the formation of bound electron-hole pairs, which are called *excitons*.

Excitons are responsible for intense absorption lines below the bandgap energy in a region expected to be transparent. Less photon energy is required for the exciton transition compared with the bandgap transition because of the binding energy of the electron-hole pair in the final state. The process of absorption of one photon corresponds to the direct creation of an exciton inside the crystal.

The twofold degenerate conduction band and the six valence bands give rise to a rich structure of the exciton or polariton levels in CuCl and CdTe. In semiconductors, the binding energy of the exciton ground state is small compared to the widths of valence and /or conduction band, and the mean distance between electron and hole is large compared to the lattice constant. Therefore, if the bands are only spin degenerate, the exciton can be described in the effective-mass approximation, i.e. electron and hole are considered as quasiparticles whose inverse mass is given by the curvature of conduction and valence band, respectively, and the electron-hole interaction can be described by a Coulomb potential screened by the dielectric constant ϵ of the solid.

The possible symmetries at (or close to) the Γ -point are found from the reduction of the direct product of the irreducible representations of the conduction band, of the valence bands and of the envelope function. The symmetry of the total wavefunction is therefore given by

$$\Gamma^{cond} \otimes \left(\sum \Gamma^{hole} \right) \otimes \Gamma^{env} = \sum_i a_i \Gamma_i^{exciton}, \quad a_i = 0, 1, 2, \dots \quad (2.4)$$

We restrict ourselves to the exciton states with a Γ_1 envelope function. Therefore, we obtain twelve exciton levels i.e. $\sum a_i g_i = 12$ where g_i gives the degeneracy of the irreducible representation Γ_i of the exciton state i . We introduce the following twelve electron-hole pair states

$$\psi_1 = | \phi_1^c \phi_1^v | \quad \psi_5 = | \phi_2^c \phi_1^v | \quad \Phi_1 = | \phi_1^c \phi_5^v |$$

$$\begin{aligned}
 \psi_2 &= | \phi_1^c \phi_2^v | & \psi_6 &= | \phi_2^c \phi_2^v | & \Phi_2 &= | \phi_1^c \phi_6^v | \\
 \psi_3 &= | \phi_1^c \phi_3^v | & \psi_7 &= | \phi_2^c \phi_3^v | & \Phi_3 &= | \phi_2^c \phi_5^v | \\
 \psi_4 &= | \phi_1^c \phi_4^v | & \psi_8 &= | \phi_2^c \phi_4^v | & \Phi_4 &= | \phi_2^c \phi_6^v | .
 \end{aligned} \tag{2.5}$$

For simplicity, the wave vector of each Bloch state is not explicitly written. In CuCl, we obtain two exciton series from the two uppermost valence and the lowest conduction band. Their ground states are transforming as (10)

$$\begin{aligned}
 Z_{1,2} &: \Gamma_6^{cond} \otimes \Gamma_8^{hole} \otimes \Gamma_1^{env} = \Gamma_3 \oplus \Gamma_4 \oplus \Gamma_5, \\
 Z_3 &: \Gamma_6^{cond} \otimes \Gamma_7^{hole} \otimes \Gamma_1^{env} = \Gamma_2 \oplus \Gamma_5.
 \end{aligned} \tag{2.6}$$

Exciton from the Γ_7 and Γ_8 valence bands and the lowest conduction band are often referred to as Z_3 and Z_{12} excitons (9), respectively. These exciton series are well separated from each other due to the spin-orbit interaction which separates the valence bands of Γ_7 - and Γ_8 -symmetry. The Γ_7 levels form the uppermost valence bands (because of a negative spin-orbit coupling).

The exciton ground state (Z_3) is only fourfold degenerate with a binding energy of about 197 meV at 4 K (6; 11; 12; 13; 14; 15). Therefore, we restrict ourselves to the Z_3 exciton ground state. Γ_2 and Γ_5 can be classified according to the system's total angular momentum J and its z component m_j . The triplet Γ_2 exciton state (corresponding to $J=0$) has an energy of $E_{Triplet} = 3.200\text{eV}$ at 4K and does not carry a dipole moment. The exciton state with Γ_5 -symmetry (corresponding to $J=1$) consists of three states. From (10) we find for the angular part of the exciton wavefunction at $K=0$ for the state transforming like Γ_2 and $J = 0$:

$$\psi_{ex}(\Gamma_2) = \frac{1}{\sqrt{2}}(\phi_2^c \phi_6^v + \phi_1^c \phi_5^v), \tag{2.7}$$

and for states transforming as Γ_5 and $J=1$ in the basis $| J, m_j \rangle$:

$$| 1, +1 \rangle = \Phi_2 = | \phi_1^c \phi_6^v |$$

$$\begin{aligned}
 |1, 0\rangle &= \frac{1}{\sqrt{2}}(\Phi_4 - \Phi_1) = \frac{1}{\sqrt{2}}(|\phi_2^c\phi_6^v\rangle - |\phi_1^c\phi_5^v\rangle) \\
 |1, -1\rangle &= -\Phi_3 = -|\phi_2^c\phi_5^v\rangle.
 \end{aligned} \tag{2.8}$$

In the basis vectors along the cubic axes:

$$\begin{aligned}
 \psi_{ex}(x) &= -\frac{i}{\sqrt{2}}(\phi_2^c\phi_5^v + \phi_1^c\phi_6^v) \\
 \psi_{ex}(y) &= \frac{1}{\sqrt{2}}(\phi_2^c\phi_5^v - \phi_1^c\phi_6^v) \\
 \psi_{ex}(z) &= -\frac{1}{\sqrt{2}}(-\phi_2^c\phi_6^v + \phi_1^c\phi_5^v).
 \end{aligned} \tag{2.9}$$

We shall return to these exciton wavefunctions in Section 5.2, where we formulate the invariant expansion method of the Hamiltonian (see page 109).

Due to the analytical and the non-analytical exchange interactions, the degeneracy of the exciton ground state is partially lifted. Then, the energy of the triplet exciton remains unchanged and the energies of the Γ_5 excitons increase. The analytical exchange interactions, leads to splitting Δ_{ST} of the Γ_5 exciton and the triplet exciton Γ_2 . The non-analytical exchange interaction removes the degeneracy of the Γ_5 exciton giving rises to longitudinal-transverse splitting (Δ_{LT}). The non-analytical exchange interaction has only an influence on states in which the exciton dipole moments is oriented parallel to the direction of propagation (16) given by the wave vector \vec{K} . These states are called "longitudinal" excitons, while excitons with a dipole moment perpendicular to \vec{K} are called "transverse". The energies of the transverse excitons and of the longitudinal increase in CuCl to $E_T = 3.2025\text{eV}$ and $E_L = 3.2080\text{eV}$ (17). The dipole active transverse excitons are coupled strongly to the light field, giving rises to exciton polaritons as propagating modes.

2.3 Exciton polaritons

There are two situations in which the interaction of light with matter can be described differently. One is a weak coupling case which can be treated by perturbation theory. In this approach, the electromagnetic field and the excitations of the matter are treated as independent quantities. This approach is sufficient for many purposes. The other one occurs in the case of strong coupling between light and matter as it is the case of bulk semiconductors. It leads to the polariton concept. The optically excited state of matter is connected with some polarization P , otherwise the transition would be optically forbidden, i.e., it would not couple to the electromagnetic field via the dipole-operator. On the other hand, we know that every oscillating polarization emits an electromagnetic wave which may act back onto the incident electromagnetic field. If one transition is coupled only to one mode of the field, we are in the case of the strong coupling limit between light and matter. The correct description of an optically active exciton in bulk semiconductors must include the polariton concept.

Exciton polaritons were intensively studied in the 60's and 70's, their manifestation in various optical phenomena, including light reflection and transmission, photoluminescence and resonant light scattering, are well-established and documented (see Ref (18) and references therein). Renewed interest and recent important developments in this field were stimulated by technological achievements in fabrication of high-quality multi-layered heterostructures, multiple quantum wells and superlattices. Because of the lack of translational invariance in one direction the polariton concept has to be modified. We will consider in the following in some detail the exciton-polariton effect and recall the main results obtained from a phenomenological theory.

2.3.1 Polariton dispersion

In a phenomenological approach, the electronic excitations are replaced by a set of oscillators of identical frequency. One can either calculate the dielectric constant and the resulting dispersion relation, or write the Lagrangian or the quantized Hamiltonian of the modes and calculate explicitly the eigenstates. Concerning the dispersion relation, both methods give the same results. They show, however, different aspects of the problem. In first step, we shall regard excitons as a collection of identical, harmonic oscillators. Electrons and holes are charged and have together the mass m . We couple this independent oscillators to the electric light field. The equation of motion is given by

$$m\ddot{x}(t) - \gamma m\dot{x}(t) + m\omega_0 x(t) = eE_0 e^{-i\omega t}, \quad (2.10)$$

where $x(t)$ is the separation from their equilibrium position and $E_0 e^{-i\omega t}$ is the incident oscillating electric field and ω_0 is the resonance frequency. We have included a phenomenological damping constant γ . The general solution is

$$x(t) = x_0 \exp[-i(\omega_0^2 - \gamma^2/4)^{1/2}t] \exp(-t\gamma/2) + x_p e^{-i\omega t}. \quad (2.11)$$

Inserting this solution into Eq. (2.10) we find

$$x_p = \frac{eE_0}{m} (\omega_0^2 - \omega^2 - i\omega\gamma)^{-1}. \quad (2.12)$$

This oscillation is connected with a dipole moment at every oscillator of

$$p_x = ex_p, \quad (2.13)$$

and the polarizability

$$\alpha(\omega) = \frac{ex_p}{E_0} = \frac{e^2}{m} (\omega_0^2 - \omega^2 - i\omega\gamma)^{-1}. \quad (2.14)$$

2.3 Exciton polaritons

If we use a three-dimensional array of oscillators with density N , the result is the same and we obtain a polarization density \mathbf{P}

$$\mathbf{P} = N\alpha\mathbf{E}_0 = \frac{Ne^2}{m}(\omega_0^2 - \omega^2 - i\omega\gamma)^{-1}E_0. \quad (2.15)$$

where N is the number of oscillators per unit volume. In the one oscillator model we can find the following expressions for the dielectric displacement \mathbf{D} , the dielectric function $\epsilon(\omega)$, and the susceptibility $\chi(\omega)$:

$$\mathbf{D} = \epsilon_0\mathbf{E} + \mathbf{P} = \epsilon_0\left[1 + \frac{Ne^2}{m}(\omega_0^2 - \omega^2 - i\omega\gamma)^{-1}\right]E_0, \quad (2.16)$$

and

$$\epsilon(\omega) = 1 + \frac{Ne^2}{m}(\omega_0^2 - \omega^2 - i\omega\gamma)^{-1} = \chi(\omega) + 1, \quad (2.17)$$

The term Ne^2m^{-1} in Eq. (2.15) gives the coupling strength of the electromagnetic field to the oscillators in our mechanical model. In this simple model $\epsilon(\omega)$ and the susceptibility $\chi(\omega)$ are scalar functions.

In quantum mechanics, this coupling is given by the square of the transition matrix element. For dipole-allowed transitions this reads

$$|H_{ij}|^2 = |\langle i | \vec{\mathbf{d}} | j \rangle|^2, \quad (2.18)$$

where i and j stand for initial and final states and $\vec{\mathbf{d}}$ for the dipole operator. We obtain for the oscillator strength f_{ij}

$$f_{ij} \propto |H_{ij}|^2 \frac{Ne^2}{m}. \quad (2.19)$$

Let us consider transitions from the ground state and drop the index i . A semiconductor contains not only one type of oscillators and one resonance frequency ω_0 . In order to take this fact into account we have to sum over all resonances. In the case of isolated resonances this lead to

$$\epsilon(\omega) = \sum_j \left(1 + \frac{f_j}{\omega_{0j}^2 - \omega^2 - i\omega\gamma_j}\right), \quad (2.20)$$

2.3 Exciton polaritons

For fields whose frequency ω is close to states with energy $\hbar\omega_0$ this function is approximated by

$$\epsilon(\omega) = \epsilon_b \left(1 + \frac{f}{\omega_0^2 - \omega^2 - i\omega\gamma} \right), \quad (2.21)$$

where ϵ_b is the background dielectric constant which account for all other oscillators not explicitly considered in the model. All wave-like excitations can be described by two quantities, namely their (angular) frequency ω which is connected with energy by $E = \hbar\omega$ and their wave vector \mathbf{k} which gives the (quasi-) momentum $\hbar\mathbf{k}$. The relation which connects ω and \mathbf{k} is usually called dispersion relation $E(\mathbf{k})$ or $\omega(\mathbf{k})$. For photons in vacuum it is a straight line with slope hc . The relation between ω and \mathbf{k} for polaritons, i.e., for the light quanta in matter, can be derived from quantum-mechanic and agrees with the results of the classical physics treatment outlined above. We obtain

$$\frac{c^2 k^2}{\omega^2} = \epsilon(\omega). \quad (2.22)$$

This is the so-called polariton equation. We know $\epsilon(\omega)$ which is given in the vicinity of an isolated resonance by Eq. (2.21). Putting Eq. (2.21) and Eq. (2.22) together we find

$$\frac{c^2 k^2}{\omega^2} = \epsilon_b \left(1 + \frac{f}{\omega_0^2 - \omega^2 - i\omega\gamma} \right). \quad (2.23)$$

This is an implicit representation of $\omega(\mathbf{k})$ for the polaritons in the frame of a one oscillator model. The dielectric function given in Eq. (2.21) for the simple case of an isolated resonance has to be modified if the oscillators are coupled. This leads to spatial dispersion. In this case, the exciton eigenfrequency ω_0 has to be replaced by $\omega_0(\mathbf{k})$ and the damping γ may also depend on \mathbf{k} . Then, $\epsilon(\omega, \mathbf{k})$ reads

$$\epsilon(\omega, \mathbf{k}) = \epsilon_b \left(1 + \frac{f E_T^2(\mathbf{k} = 0)}{\hbar^2 \omega_0^2(\mathbf{k}) - \hbar^2 \omega^2 - i \hbar^2 \omega \gamma(\mathbf{k})} \right). \quad (2.24)$$

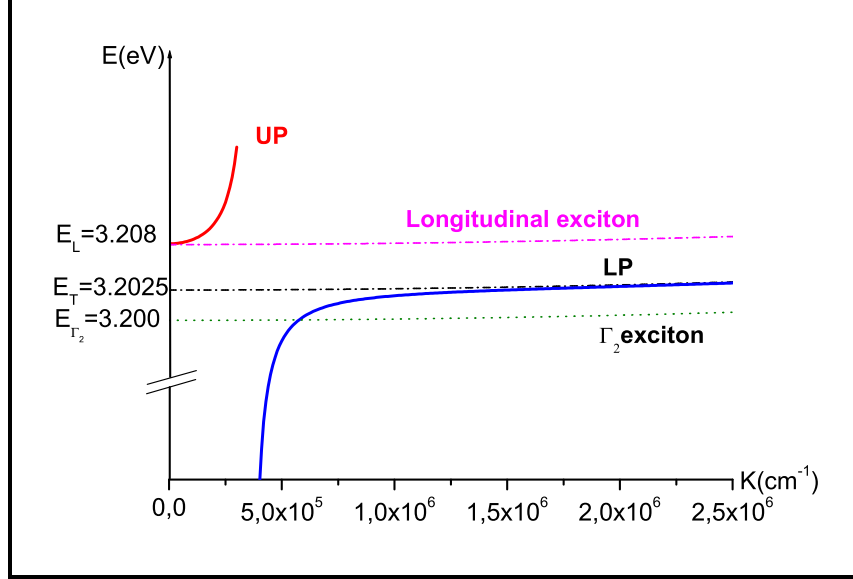


Figure 2.3: The polariton dispersion curve in CuCl.

The most significant change is the fact that ϵ is now a function of two variables, ω and \mathbf{k} .

Along with the transverse eigenfrequency that of the longitudinal exciton also becomes \mathbf{k} -dependent, i.e., $\omega_L = \omega_L(\mathbf{k})$. It is well known that the oscillator strength is proportional to the longitudinal-transverse splitting of dipole-allowed excitons (19) at $\mathbf{k}=0$. In principle all of the above quantities have to be given as a function of \mathbf{k} . We will consider the case of vanishing damping. The oscillator strength is related to nonanalytic exchange interaction, and

$$f = \frac{E_L^2(\mathbf{k}=0) - E_T^2(\mathbf{k}=0)}{E_T^2(\mathbf{k}=0)}. \quad (2.25)$$

We can rewrite the Eq. (2.24) as a function of energies

$$\epsilon(\mathbf{k}, E_i) = \left(\frac{\hbar^2 c^2 k^2}{E_i^2(\mathbf{k})} \right) = \epsilon_b \left[1 + \frac{E_L^2(\mathbf{k}=0) - E_T^2(\mathbf{k}=0)}{E_T^2(\mathbf{k}) - E_i^2(\mathbf{k})} \right], \quad (2.26)$$

the index i labels the upper branch polariton (UP) and the lower branch polariton (LP). In the case of CuCl, equation (2.26) may be solved analytically, and we

obtain for the polariton dispersion, including spatial dispersion

$$E_i(\mathbf{k}) = \frac{1}{\sqrt{2}}(A \pm \sqrt{A^2 - 4B^2})^{1/2} \quad i = UP, LP \quad (2.27)$$

with

$$A = \frac{\hbar^2 c^2 \mathbf{k}^2}{\epsilon_b} + E_T^2(\mathbf{k})(1 + f) \quad B^2 = \frac{\hbar^2 c^2 \mathbf{k}^2 E_T \mathbf{k}}{\epsilon_b}, \quad (2.28)$$

where the exciton dispersion is given by (see chapter 5)

$$E_T(\mathbf{k}) = \Delta_{ST} + E_{ex} + \frac{\hbar^2 \mathbf{k}^2}{2M}. \quad (2.29)$$

Where M is the exciton effective mass. The dispersion of Eq. (2.27) is shown in Fig. 2.3. We obtain two polariton branches, which are separated by an energy gap in the absence of spatial dispersion. Their character changes with photon energy. Close to the exciton resonance, the branches are more exciton like and outside more photon like. For the lower energy branch in the transparent region, the polaritons are photon like and their dispersion curve is a straight line, representing the dispersion of light. In the crossing region, called "bottleneck region" the polaritons become more exciton like. The exciton polariton has the following characteristics :

- The bare photon and exciton branches are pushed apart as usual for coupled modes and an anticrossing appears at the resonance.
- For small wavevectors, the exciton branch (upper branch) is pushed up by an amount which is that of the transverse-longitudinal exciton splitting, while the photon branch (lower polaritons) still goes to zero.

As shown in Fig. 2.4 the polariton dispersion gives rise to a strong energy dependence of the group velocity

$$v_g = \frac{1}{\hbar} \frac{dE_i(\mathbf{K})}{d\mathbf{K}}. \quad (2.30)$$

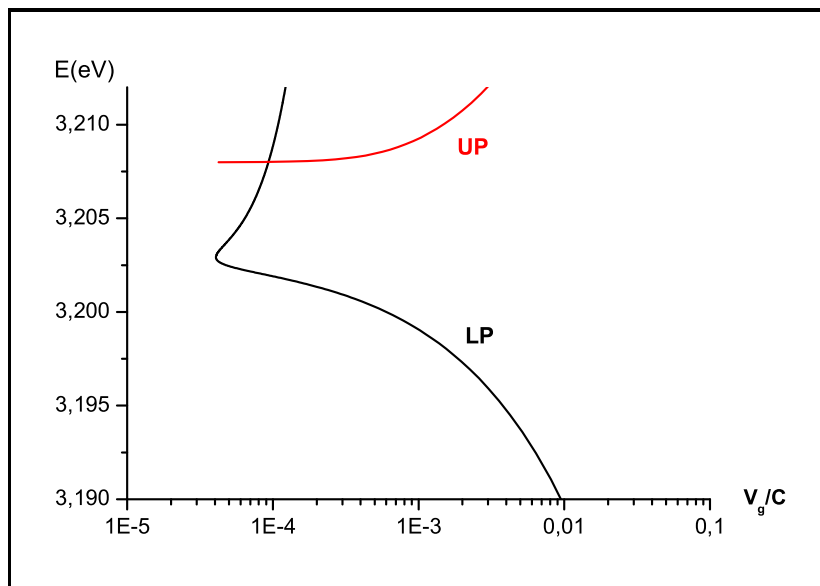


Figure 2.4: The polariton group velocity calculated from the dispersion.

We shall return to this concept in Section 4.2, where we take a closer look on its consequences for spin relaxation in our experimental situation.

In the case of quantum wells, due to the lack of translational invariance along the growth direction, the coupling between excitons and photons is substantially modified from that of bulk material. Now one is no-longer in the strong-coupling regime for this direction. The polariton modes are unstable and very fast intrinsic recombination processes are expected (20; 21; 22). These processes must be included in a complete analysis of the time-resolved luminescence data. Only excitons close to the minimum of the kinetic energy, i.e. excitons with wavevector $\vec{K} \approx 0$, are able to couple to radiation, those thermalized to larger-K states cannot recombine until they are scattered back to lower energy, inside the light cone.

2.4 Biexcitons

Light absorption by a semiconductor can be described basically in terms of generation of electron-hole pairs. Electron-hole pairs created by photons with energy $\hbar\omega$, which is larger than the exciton ground states energy ε_1 by an excess amount $\Delta\varepsilon = \hbar\omega - \varepsilon_1$, rapidly lose their excess energy by emission of optical and acoustic phonons until they reach the lowest exciton level $n = 1$. Thus, after fast energy relaxation (the process of dissipation of excess energy) and before recombination (the process of annihilation of an electron-hole pair either by emission of photons or through a nonradiative process), the ensemble of excitons forms a gas similar to a gas of free hydrogen atoms.

As the excitons density increases as a result of increased excitation intensity the excitons can bind to form excitonic molecules, also called biexcitons. Their spin structure is similar to that of hydrogen molecules. The formation of a biexciton due to the coupling of a pair of excitons and its analogy to a hydrogen molecule have been experimentally established. Evidence for the existence of such biexciton states in semiconductor was first seen in CuCl, and later in a large number of other materials. In the case of a simple band structure, such as CuCl, only one molecular excited level has been observed, in contrast to hydrogen molecules which show a rich manifold of excited levels.

Concerning the biexciton wavefunction, it has to be an antisymmetric function with respect to the exchange of the two electrons and the holes because of the Pauli principle. In analogy with the hydrogen molecule, one assumes the spin part of the biexciton wavefunction of the ground state to be antisymmetric with respect to the exchange of two identical particles. A symmetrical spin configuration leads to excited biexciton states which correspond to the rotational states of the molecule. In the case of the biexciton ground state, the envelope function is a

symmetric (s-type) function and transform like Γ_1 . We then obtain for the total symmetry of the biexciton wavefunction

$$\Gamma_{Bi} = \Gamma_{env}^{++} \otimes (\Gamma_e \otimes \Gamma_e)^- \otimes (\Gamma_h \otimes \Gamma_h)^-, \quad (2.31)$$

Where the upper index denotes the transformation properties with respect to the exchange of two identical particles (+symmetric, - antisymmetric). Considering the band structure of CuCl, we find for the case where both holes are in the valence band with Γ_7 -symmetry and the electrons in the conduction band with Γ_6 -symmetry:

$$(\Gamma_e \otimes \Gamma_e)^- \otimes (\Gamma_h \otimes \Gamma_h)^- = \Gamma_1. \quad (2.32)$$

Therefore, the biexciton ground state is transforming like Γ_1 and its Bloch functions are given by

$$\psi_{Bi}^{\Gamma_1} = \frac{1}{2}[\alpha_e(1)\beta_e(3) - \beta_e(1)\alpha_e(3)] \otimes [\phi_5(2)\phi_6(4) - \phi_6(2)\phi_5(4)], \quad (2.33)$$

where the indices (1),(3) and (2), (4) denote the electrons and holes, respectively. If we transform the wavefunction given in Eq. (2.7) and Eq. (2.9) , we obtain for the wavefunction of the biexciton ground state

$$\psi_{Bi}^{\Gamma_1} = \frac{1}{2}[\psi_{ex}^A(x)\psi_{ex}^B(x) + \psi_{ex}^A(y)\psi_{ex}^B(y) + \psi_{ex}^A(z)\psi_{ex}^B(z) + \psi_{ex}^A(\Gamma_2)\psi_{ex}^B(\Gamma_2)]. \quad (2.34)$$

Here, the excitons labeled A and B are formed by the electron-hole pairs (1,4) and (3,2), respectively.

The energy of biexciton is given by

$$\varepsilon_{xx} = 2\varepsilon_x^0 - E_{Bxx} + \frac{\hbar^2 K_{xx}^2}{2M_{xx}} = \varepsilon_{xx}^0 + \frac{\hbar^2 K_{xx}^2}{2M_{xx}}, \quad (2.35)$$

where $2\varepsilon_x^0 = 2(E_g - E_B)$ is the internal energy of two noninteracting excitons at zero wave vector, ε_{xx}^0 is the biexciton energy at zero wave vector, E_{Bxx} is the

biexciton binding energy and K_{xx} and M_{xx} are the center-of-mass wave vector and the effective mass of the biexciton, respectively. The biexciton effective mass is about twice the exciton mass, $M_{xx} = 2M$.

2.4.1 The polarization selection rules

To provide the basis for the analysis of our experimental results in CuCl, it is necessary to understand the polarization selection rules, for transitions between the crystal ground state and excitons and between excitons and biexcitons.

By using two independent laser beams so that one photon from each beam is absorbed in a two-photon absorption process, it is possible to create directly a biexciton. One can thus obtain information on the symmetry of the biexciton state by varying the polarization vector of each beam. For instance, if both laser beams are colinearly and have the same circular polarization, there is no allowed two-photon absorption to the biexciton state, while it is allowed if the two beams are oppositely circular polarized (we will use this concept in order to explain our experiments in Chapter 4). This confirms that the created biexciton state involves two electrons with opposite spin orientation. To understand this, we note that the angular momentum carried by each absorbed photon is transferred to the spin of the electrons and of the holes in the biexciton. Since the photon angular momenta are opposite, the spins of the electrons are also opposite. Therefore, the biexciton is a paramolecule, similar to the ground state of the hydrogen molecule.

2.4.2 Biexciton Luminescence

Luminescence studies provide an interesting method for the investigation of several properties of crystal, such as the excitonic and biexcitonic effects and the band structure. They also help to evaluate the quality of the crystal. Impurities

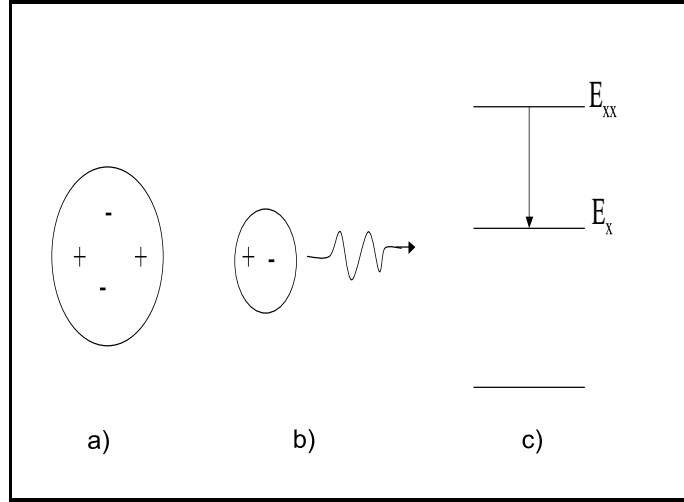


Figure 2.5: Elementary process leading to biexciton luminescence; a) A biexciton before radiative recombination and b) The state of the system after radiative recombination. c) Schematic representation of the energy levels involved in the optical transition leading to biexciton luminescence.

which act as substitutional atoms in the crystal, even in small quantities, give rise to intense luminescence lines with characteristic wavelengths, allowing the determination of their nature and concentration (like the ν_2 line in Fig.2.6).

After biexciton formation in CuCl by coupling of two exciton polaritons, they may emit a longitudinal optical phonon whose energy $\hbar\omega_{LO} = 26.0$ meV (23) is close to the biexciton binding energy ($E_b = 28$ meV). This process is very efficient because of its nearly resonant nature and because of the highly polar binding of CuCl, leading to a strong coupling between electrons and longitudinal optical phonon. Biexcitons may further thermalize on their dispersion curve by emission of acoustic phonons before they recombine radiatively. In this process, a photon-like polariton is generated together with a longitudinal exciton or a second, exciton-like polariton. An elementary step in the radiative decay process of a biexciton is shown in Fig 2.5. The recombination obeys to energy and

momentum conservation.

$$\varepsilon_{xx}(K_{xx}) = \hbar\omega + \varepsilon_x(K_x), \quad (2.36)$$

or

$$\varepsilon_{xx}^0 + \frac{\hbar^2 K_{xx}^2}{2M_{xx}} = \hbar\omega + \varepsilon_x^0 + \frac{\hbar^2 K_x^2}{2M}. \quad (2.37)$$

The momentum conservation is

$$\vec{K}_{xx} = \vec{K}_x + \vec{q}, \quad (2.38)$$

where \vec{q} is the wave vector of the photon-like polariton.

After thermalization, biexcitons are distributed on their dispersion relation like a classical gas with an effective temperature. They recombine and, since exciton and biexciton effective masses are different, the biexciton emission line takes the form of an inverted Maxwell-Boltzmann shape. Photons of lower energy correspond to decaying biexcitons with larger kinetic energy. In reality, the situation is more complex because of the longitudinal-transverse splitting of excitons. Therefore, there are two final exciton branches, as shown in Fig. 2.6.

Two corresponding emission bands appear for the decay of the biexcitons, which are called M_L and M_T . The emission from the M_T branch deviates from the inverted Maxwell-Boltzmann lineshape near $K_x = 0$ because of the strong dispersion change due to the polariton effect (see section 2.3). The longitudinal excitons or polaritons can further thermalize to lower branch polaritons by emission of acoustic or optical phonons. In addition, two excitons or exciton polaritons may couple and form again biexcitons which relax their energy as described above.

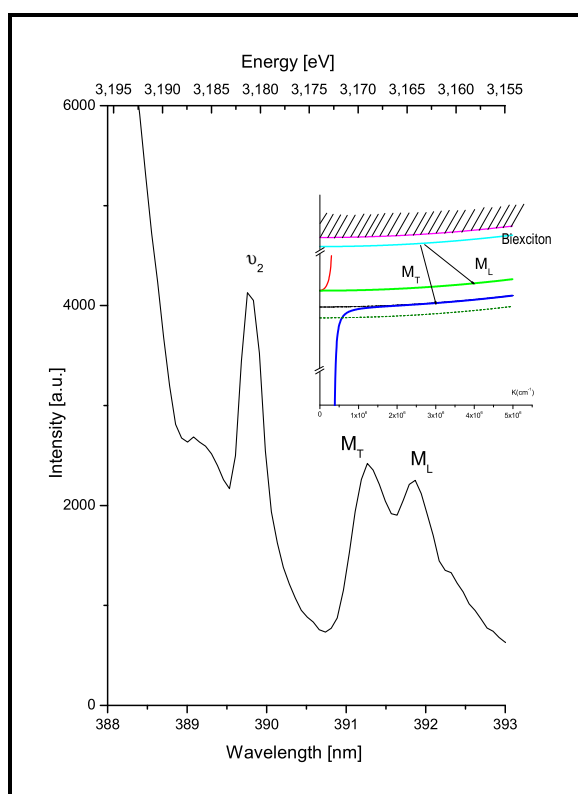


Figure 2.6: The luminescence spectra of our sample (CuCl) at 5K. The biexciton can decay to either the transverse or longitudinal exciton branch, giving rise to emitted at energies M_T or M_L , respectively. ν_2 is an impurity line.

2.5 CdTe : Valence and conduction band states

Bulk CdTe has also the zinc-blende structure shown in Fig. 2.1. The compound has an energy gap E_g of about 1.6 eV between the valence band and the conduction band (24). Both, the top of the valence band and the bottom of the conduction band, are at the Γ point of the Brillouin zone. The conduction band is a spin degenerate band that, in a good approximation, is parabolic for not too large values of the wave vector K . The conduction band at $K = 0$ has Γ_6 symmetry, and the wave functions at $K = 0$ are s-like (mainly Cd-5s orbitals) and are similar to CuCl. The valence-band wave functions at $K = 0$ are P-type (mainly Te-5p orbitals), and the sixfold degenerate p-states split due to spin-orbit coupling into a fourfold degenerate state $\mathbf{j}=\frac{3}{2}$ with Γ_8 symmetry, and a twofold degenerate state $\mathbf{j}=\frac{1}{2}$ with Γ_7 symmetry [\mathbf{j} is the total angular momentum $\mathbf{j} = \mathbf{l} + \mathbf{s}$, \mathbf{l} is the angular momentum and \mathbf{s} is the spin; $l = 1$, $s = \frac{1}{2}$ for the top of the valence band].

The Γ_8 and Γ_7 states at $K = 0$ are separated by Δ_{so} , the spin-orbit parameter, which is quite large for Te-5p orbitals; in CdTe $\Delta_{so} = 0.949$ eV at $T=1.7$ K (25). The wave function of the valence-band states at $K = 0$ with Γ_8 symmetry ($j = \frac{3}{2}$) and Γ_7 symmetry ($j = \frac{1}{2}$) are similar to those with Γ_8 and Γ_7 symmetry in CuCl (see Eq.2.3 and Eq.2.2).

2.6 CdTe /CdMnTe quantum wells

Modern growth techniques such as Molecular Beam Epitaxy (MBE) and Metal Organic Chemical Vapor Deposition (MOCVD) make it possible to manufacture ultrathin semiconductor structures of high quality. Ultrathin refers to a film

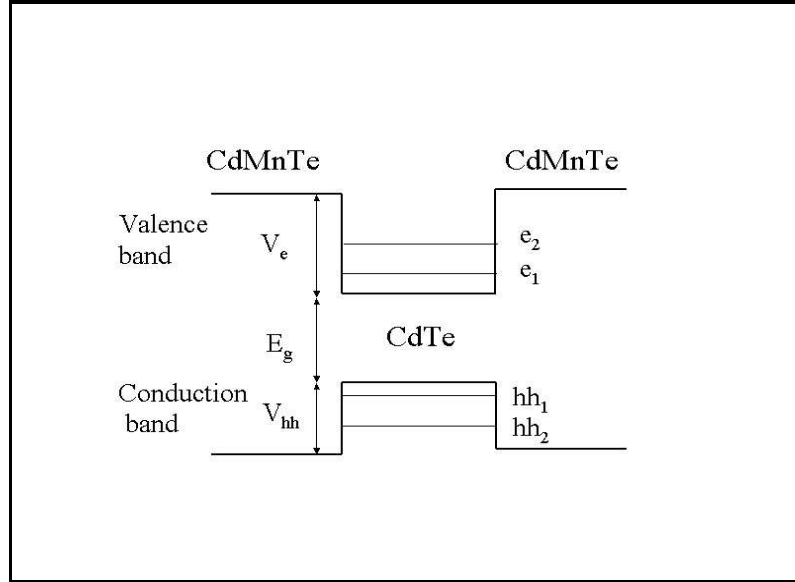


Figure 2.7: Level scheme for a single quantum well of CdTe sandwiched between two CdMnTe barriers.

thickness which is comparable to the de Broglie wavelength of electrons and holes. Semiconductor films of thicknesses less than 100\AA are referred to as quantum-confined quasi-two-dimensional systems. To one class of such artificially grown quasi-two-dimensional systems belong quantum-well structures.

A single quantum well consists of an ultrathin layer ($d \leq 100 \text{\AA}$) of a semiconductor sandwiched between thin layers of a larger gap semiconductor with matching or mismatching lattice constants. If we have several quantum wells in a material with barriers which are so thick that the wavefunctions of electrons of adjacent wells do not overlap, we speak about multiple quantum wells.¹ Multiple quantum wells are currently attracting considerable interest, both from a fundamental point of view, as well as for their potential applications as efficient, active devices in optoelectronics. Ideally, multiple quantum wells display the optical properties of a single quantum well, except that the optical density of the

¹If the barriers are thin enough to allow overlap, one has a superlattice.

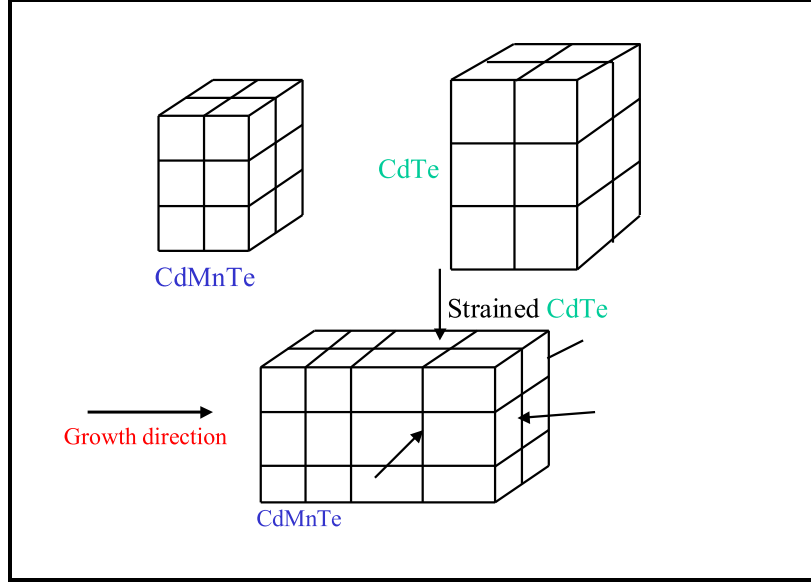


Figure 2.8: Schematic representation of unstrained CdTe and CdMnTe and strained CdTe/CdMnTe

structure along the growth axis is multiplied by n , the total number of periods.

2.7 Band structure in strained quantum wells

The characteristics of a semiconductor are greatly influenced by the presence of strains, which change the lattice constant and reduce the symmetry of the crystal. Strains modify energy gaps and lift partly degeneracies. Most strains in semiconductor heterostructures occur because the different alloys in the heterostructures have different atomic spacings, hence different lattice constants. This is called lattice mismatch (Fig. (2.8)). For the case of strained-layer semiconductor quantum wells in which we are interested, the total Hamiltonian H_{total} for the valence band can be written as two parts:

$$H_{total}^v = H_{Luttinger-Kohn} + H_{strain}^v. \quad (2.39)$$

2.7 Band structure in strained quantum wells

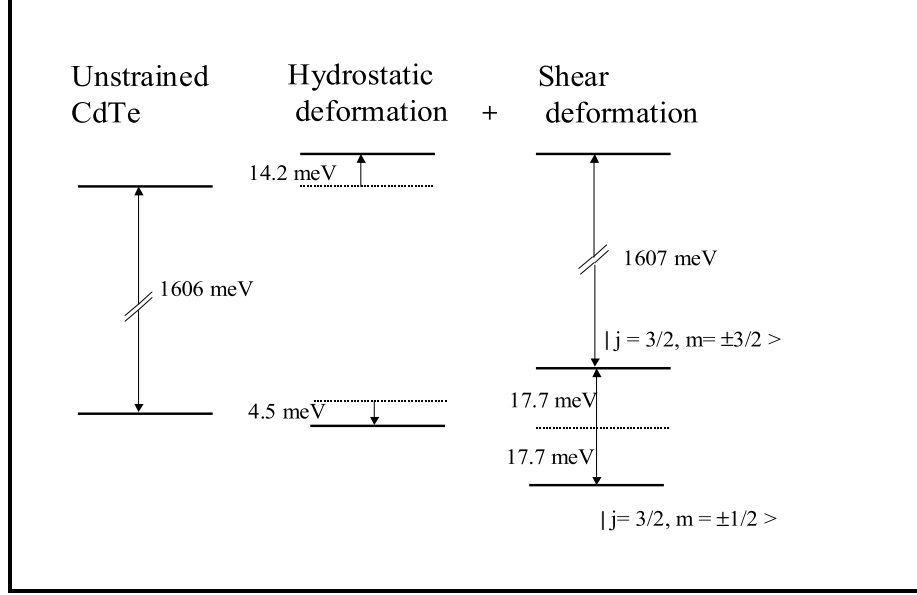


Figure 2.9: Splitting of the energy in the strained-layer CdTe/CdMnTe quantum wells due to a hydrostatic deformation potential and shear deformation potentials (Ref. (26)).

Neglecting k -linear terms, the first part depends quadratically on the components of the wave vector k_x , k_y and k_z . The 4×4 Luttinger-Kohn Hamiltonian in the basis of the total angular momentum $j=3/2$ (Eq. 2.3) quantized along z , is given by as

$$\begin{aligned}
 H_{Luttinger-Kohn} &= \frac{1}{2}(\gamma_1 + \frac{5}{2}\gamma_2)k^2 - \gamma_2[k_x^2 J_x^2 + c.p.] \\
 &- \gamma_3[k_x k_y (J_x J_y + J_y J_x) + c.p.].
 \end{aligned} \tag{2.40}$$

In eq. (2.40) the axes x , y , and z are, respectively, parallel to $[001]$, $[010]$, and $[001]$ as usual. $c.p.$ means circular permutation and γ_i are the Luttinger parameters. The 4×4 Luttinger-Kohn Hamiltonian in the $[111]$ direction can be expressed by (27)

2.7 Band structure in strained quantum wells

$$\begin{array}{c} \phi_1^v \\ \phi_2^v \\ \phi_3^v \\ \phi_4^v \end{array} \begin{pmatrix} \phi_1^v & \phi_2^v & \phi_3^v & \phi_4^v \\ P+Q & -S & R & 0 \\ -S^* & P-Q & 0 & R \\ R^* & 0 & P-Q & S \\ 0 & R^* & S^* & P+Q \end{pmatrix}, \quad (2.41)$$

with

$$\begin{aligned} P \pm Q &= \frac{1}{2}(\gamma_1 \mp 2\gamma_3)k_z^2 + \frac{1}{2}(\gamma_1 \pm \gamma_3)k_{\parallel}^2, \\ R &= -\frac{\sqrt{3}}{6}(2\gamma_3 + \gamma_2)k_-^2 - \frac{\sqrt{3}}{4}(\gamma_3 - \gamma_2)k_+k_z \\ S &= \frac{\sqrt{3}}{3}(\gamma_3 + \gamma_2)k_-k_z + \frac{\sqrt{6}}{6}(\gamma_3 - \gamma_2)k_+^2. \end{aligned} \quad (2.42)$$

Where k_{\parallel} and k_{\pm} are defined as $k_{\parallel}^2 = k_x^2 + k_y^2$ and $k_{\pm} = k_x \pm ik_y$.

The second part of the total Hamiltonian (Eq. 2.39), depends on the strain components ϵ_{ij} , with a one-to-one correspondence between terms $k_i k_j$ and ϵ_{ij} (28; 29; 30; 31). The valence-band Luttinger Hamiltonian (32) is modified by the Pikus-Bir strain Hamiltonian (28; 29). In this description, we have a transformation of the coordinate system of the strained crystal \mathbf{x}_{ϵ} with respect to that of the unstrained one \mathbf{x} : $\mathbf{x}_{\epsilon} = (1 + \epsilon) \cdot \mathbf{x}$, where ϵ is the strain tensor. Correspondingly, the crystal momentum is transformed as $\mathbf{k}_{\epsilon} = (1 - \epsilon) \cdot \mathbf{k}$. Most results of $k \cdot p$ theory can be carried over from the unstrained to the strained case. For valence band (heavy-hole and light-hole), the Pikus-Bir strain Hamiltonian [001] is given by

$$\begin{aligned} H_{strain}^v &= -a_v(\epsilon_{xx} + \epsilon_{yy} + \epsilon_{zz}) \\ &- b[(J_x^2 - J^2/3)\epsilon_{xx} + c.p.] \\ &- \frac{2}{\sqrt{3}}d[(J_x, J_y)\epsilon_{xy} + c.p.], \end{aligned} \quad (2.43)$$

where a_v is the hydrostatic deformation potential, b and d the shear deformation potentials, and e_{ij} the strain tensor. The 4×4 strain Hamiltonian can be expressed

2.7 Band structure in strained quantum wells

by

$$\begin{matrix} \phi_1^v \\ \phi_2^v \\ \phi_3^v \\ \phi_4^v \end{matrix} \begin{pmatrix} \phi_1^v & \phi_2^v & \phi_3^v & \phi_4^v \\ P_\varepsilon + Q_\varepsilon & -S_\varepsilon & R_\varepsilon & 0 \\ -S_\varepsilon^* & P_\varepsilon - Q_\varepsilon & 0 & R_\varepsilon \\ R_\varepsilon^* & 0 & P_\varepsilon - Q_\varepsilon & S_\varepsilon \\ 0 & R_\varepsilon^* & S_\varepsilon^* & P_\varepsilon + Q_\varepsilon \end{pmatrix}, \quad (2.44)$$

with

$$\begin{aligned} P_\varepsilon &= -a_v(\varepsilon_{xx} + \varepsilon_{yy} + \varepsilon_{zz}) \\ Q_\varepsilon &= \frac{b}{2}(\varepsilon_{xx} + \varepsilon_{yy} - 2\varepsilon_{zz}) \\ R_\varepsilon &= \frac{b\sqrt{3}}{2}(\varepsilon_{xx} - \varepsilon_{yy}) - id\varepsilon_{xy} \\ S_\varepsilon &= d(\varepsilon_{xz} - i\varepsilon_{yz}). \end{aligned} \quad (2.45)$$

We need the ε_{ij} components for each [111] direction. We write

$$\begin{aligned} \varepsilon_{xx} &= \varepsilon_{xx} = \varepsilon_{\parallel} \\ \varepsilon_{\perp} &= \varepsilon_{zz} \\ \varepsilon_{\parallel\perp} &= \varepsilon_{\parallel} - \varepsilon_{\perp}. \end{aligned} \quad (2.46)$$

We deal in this thesis with a strained CdTe well and unstrained CdMnTe barriers so that

$$\varepsilon_{\parallel} = \frac{a(Cd_{1-x}Mn_xTe) - a(CdTe)}{a(CdTe)}, \quad (2.47)$$

where $a(X)$ is the cell parameter of the X compound. For [111] directions, the strain Hamiltonian [A.5](#)) can be rewritten as [\(27\)](#)

$$\begin{matrix} \phi_3^v \\ \phi_4^v \\ \phi_5^v \\ \phi_6^v \end{matrix} \begin{pmatrix} \phi_3^v & \phi_4^v & \phi_5^v & \phi_6^v \\ P_\varepsilon + Q_\varepsilon & 0 & 0 & 0 \\ 0 & P_\varepsilon - Q_\varepsilon & 0 & 0 \\ 0 & 0 & P_\varepsilon - Q_\varepsilon & 0 \\ 0 & 0 & 0 & P_\varepsilon + Q_\varepsilon \end{pmatrix}, \quad (2.48)$$

2.8 Piezoelectric effect in (111)-oriented CdTe/CdMnTe strained quantum wells

with

$$\begin{aligned}
 P_\varepsilon \pm Q_\varepsilon &= a_v \varepsilon_\parallel \left(\frac{8C_{44}}{C_{11} + 2C_{12} + 4C_{44}} \right) \\
 &\pm \sqrt{3}d \varepsilon_\parallel \left(\frac{C_{11} + 2C_{12}}{C_{11} + 2C_{12} + 4C_{44}} \right).
 \end{aligned} \tag{2.49}$$

The conduction-band Hamiltonian is given by

$$\begin{aligned}
 H_{total}^c &= H_k^c + H_{strain}^c \\
 &= \frac{\hbar^2}{2m^*} (k_x^2 + k_y^2 + k_z^2) + a_c (\varepsilon_{xx} + \varepsilon_{yy} + \varepsilon_{zz}),
 \end{aligned} \tag{2.50}$$

where m^* is the electron effective mass, and a_c is the hydrostatic deformation potential for the conduction band. For [111] directions, the strain Hamiltonian can be rewritten as (26)

$$H_{strain}^c = a_c \left(\frac{12C_{44}}{C_{11} + 2C_{12} + 4C_{44}} \varepsilon_\parallel \right) \tag{2.51}$$

2.8 Piezoelectric effect in (111)-oriented CdTe/CdMnTe strained quantum wells

In 1986, Smith (33) predicted the existence of large piezoelectric fields in strained semiconductor structures with [111]-growth-axis. Four years later, Caridi *et al.*(34) reported experimental evidence supporting the existence of a piezoelectric field in a GaAs diode. The sign and magnitude of the piezoelectric field induced in strained-layer heterostructures, as well as their consequences to the electronic structure and optical properties of the [111]-grown superlattices, have been analyzed in a series of papers by Mailhot and Smith (35; 36; 37). Screening effects, of such piezoelectrically induced fields on strained-layer superlattice (39; 40; 41) and quantum wells have also been studied.

Zinc-blende-structure semiconductors are piezoelectric materials. Off-diagonal

2.8 Piezoelectric effect in (111)-oriented CdTe/CdMnTe strained quantum wells

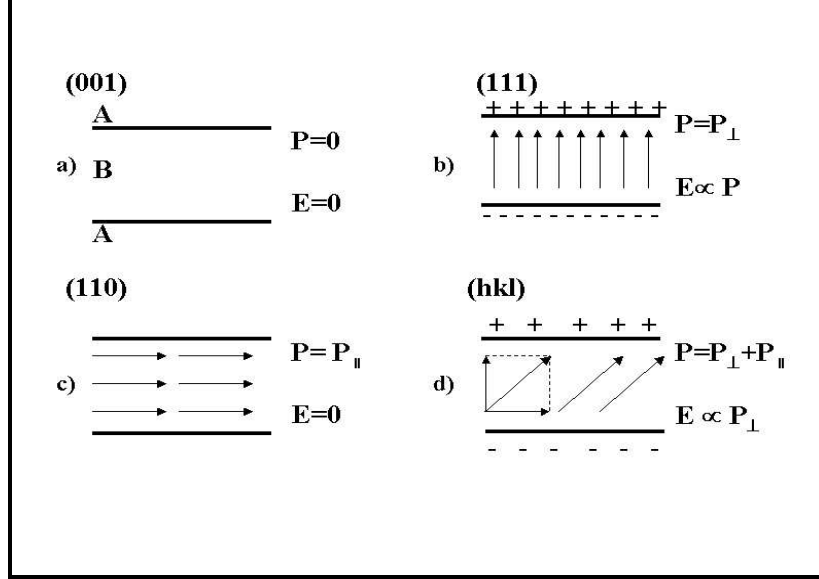


Figure 2.10: Polarization, electrical charges, and fields in a strained layer B grown on an A unstrained substrate for a) [001], b) [111], and c) [110] orientation. d) Shows the general case of a (hkl) orientation (Ref. (38)).

strains induce a polarization given by (42)

$$P_i^s = 2e_{14}\epsilon_{jk}, \quad (2.52)$$

where P_i^s is the induced polarization, e_{14} is the piezoelectric constant, and ϵ_{jk} is a symmetrized strain component. However, diagonal strains (e.g., ϵ_{xx}) do not induce a polarization (i.e., $e_{11}=0$) in these materials (42). A strained-layer superlattice with [001]-growth direction will induce only diagonal strains; but, in any other growth direction, off-diagonal strains also occur. Thus [001]-growth axis strained-layer will not have strain-induced polarization fields, but any other growth direction will lead to these polarization fields (see Fig 2.10).

Starting from the strain components, the strain-induced polarization P^s is determined from Eq. (2.52). The polarization vector is constant in each material layer and changes abruptly at the interfaces. As shown in Fig. 2.10, for a [001]-growth axis, P^s vanishes, for a [111]-growth axis, P^s is parallel to the growth axis; for a

2.8 Piezoelectric effect in (111)-oriented CdTe/CdMnTe strained quantum wells

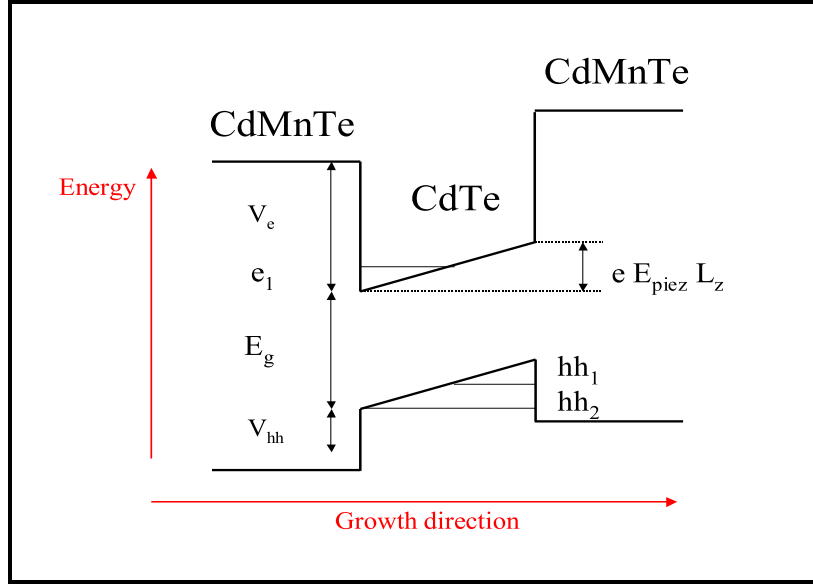


Figure 2.11: The effect of strain-induced polarization fields on the energy levels and the bands of a CdTe/CdMnTe quantum well

[110]-growth axis P^s is in the plane.

For a general growth axis, P^s has components both parallel and perpendicular to the growth axis. The strain-induced electric polarization P^s will lead to an electric field E given by (42)

$$D_i = \varepsilon_0 E_i + \varepsilon_0 \chi E_i + 2e_{14} \varepsilon_{jk}, \quad (2.53)$$

where χ is the dielectric susceptibility and D_i is the electric displacement. If there are no external charges, D_i vanishes, and the electric field reduces to

$$E_i = \frac{2e_{14} \varepsilon_{jk}}{\varepsilon_0 \varepsilon}, \quad (2.54)$$

where $\varepsilon = 1 + \chi$ is the low-frequency dielectric constant. Because strained layers in these systems are under compression, the strain tensor has off-diagonal components that lead to piezoelectric fields.

2.8.1 The effect of internal electric fields

The strain-induced electric fields can significantly modify static and dynamic response to optical excitation of the quantum well structure. Fig.2.11 shows the modified energy levels a potential well as a result of strain-induced polarization fields. The quantum well is skewed by the field as shown in figure. We consider three consequence of strain-induced polarization fields, which are important to explain our experimental results:

a) The internal electric field pushes the electrons and holes to the opposite walls of the well because of the opposite charge of the two particles, thereby modifying the overlap between the corresponding confined wave functions. Since the exchange interaction is proportional to the pair's wave function overlap, this effect strongly reduced the exciton spin flip (5; 43; 44) (see page 129).

b) Another effect of strain-induced polarization fields is the widening of the potential well, resulting a red shifting of the excitonic lines. The field ionization of the exciton, which is the dominant effect in three-dimensional bulk semiconductors, is inhibited in two dimensional systems by the walls of the quantum well. Therefore, the exciton shifts persists up to high field magnitudes. This is a result of the quantum-confined Stark effect which strongly localizes electrons and holes on opposite quantum well interfaces (45; 46). With the screening of the static piezo electric field, a blueshift of the excitonic lines is expected as we will see in our experimental results (see page 128).

c) Another important consequence of strain-induced polarization fields (or application of an external electric field) is the lowering of the symmetry and, thus, the removal of the strict transition selection rules. One of these selection rule is that the allowed transitions are those between electron and hole confined states with $\Delta n = 0$. In other words, the allowed transitions are those which occur

between the quantized electron and hole states with the same quantum number, n . Therefore, only transitions such as $H_1 \rightarrow E_1$, $H_2 \rightarrow E_2$, $H_3 \rightarrow E_3$ are allowed. The presence of a strain-induced polarization fields (or an external electric field) makes transitions with $\Delta n \neq 0$ allowed.

The appearance of $n \neq n'$ transitions can be understood in terms of deformation of the well potential by the electric field. In an unstrained quantum well (or for zero external electric field) the well potentials are perfectly square (Fig.2.7). In this case, the usual selection rule is valid for optical transitions between hole and electron subbands. In the presence of a strain-induced polarization fields, the electron and hole wave functions in the quantum well are deformed and wells (Fig.2.11), as a result of the spatial deformation of the wave functions, the overlap integral between electron and hole wave functions becomes different from zero, even for $n \neq n'$ transitions. Therefore the $n \neq n'$ transitions are no longer "forbidden". We make use of these concepts, to measure directly the individual spin relaxation times of the electrons and holes in a non-degenerate pump-probe experiment (see Chapter 6).

2.9 Spin relaxation

In the process of interband absorption of a photon in a semiconductor, an electron in the conduction band and a hole in the valence band are generated, the total spin of the electron and the hole being equal to the angular momentum of the photon absorbed. Photons of right or left circularly polarized light have a projection of the angular momentum on the direction of the wave vector equal to $+1$ or -1 , respectively. This angular momentum is distributed between the photoexcited electron and hole according to the selection rules determined by the band structure of the semiconductor. The photoexcited carriers live some time

τ_r before recombination. If during this time the spin orientation has not entirely disappeared, the recombination radiation will be partially circularly polarized.

Thus the process of optical orientation includes two stages (47): creation of spin-oriented carriers or excitons by absorption of circularly polarized light, and spin relaxation during the carriers' lifetime. Spin relaxation processes have significant effects on the optical and kinetic properties of semiconductors. Spin relaxation, i.e. disappearance of an initial non-equilibrium spin polarization, is the central issue for all spin phenomena.

In Ref. (48), M. I. Dyakonov, explains the history of spin relaxation as follows:

...The basic ideas concerning spin phenomena in semiconductor were developed both theoretically and experimentally 30 years ago. Some of these ideas have been rediscovered recently. The first experiment on optical spin orientation of electrons in semiconductor (Si) was done by Georges Lampel in 1968, as a direct application of the ideas of optical pumping in atomic physics. The important difference is that now these are the free conduction band electrons that get spin-polarized, rather than electrons bound in atoms. This pioneering work was followed by extensive experimental and theoretical studies mostly performed by small research groups at Ecole Polytechnique in Paris and Ioffe Institute in St Petersburg (Leningrad) in the 70ies and early 80ies.

Three factors, namely to store information, to transform information and optical detection, make the spin of conduction electrons attractive for future technology (49). It was discovered, however, that spins can be also measured electronically, through charge-spin coupling. Spin dynamics in semiconductor is, however, best studied by optical orientation where spin-polarized electrons and holes are created by circularly polarized light.

2.10 Longitudinal and transverse spin relaxation times

In general, the spin relaxation equation can be written in the form

$$\frac{dS}{dt} = - \sum_j \frac{S_j}{\tau_{ij}} \quad (2.55)$$

Where S_i is the spin density, and $(1/\tau_{ij})$ is a component of a second-rank tensor. The concrete form of the tensor $(1/\tau_{ij})$ depends on the symmetry of the system under study. Since in a $2D$ structure a privileged direction exists (the growth axis), spin relaxation processes are anisotropic.

2.10 Longitudinal and transverse spin relaxation times

The simplest non-trivial spin system is a two-state system, for example a spin $1/2$ for one electron. A nonequilibrium perturbation of a two-state system can have two general consequences: a change in the relative occupation of the two states, and a change in the coherence (phase) relationship in the two states. The evolution of these two components of the perturbation is described by the time T_1 or longitudinal spin relaxation time and the time T_2 or transverse spin relaxation time, respectively (1; 2). The time constant T_1 can be described as a lifetime (or relaxation time). In other words, time T_1 is the time it takes for the longitudinal magnetization to reach equilibrium. Equivalently, it is the time of thermal equilibration of the spin population with the lattice. In T_1 processes an energy has to be dissipated from the spin system, usually by phonons, to the lattice.

The time T_2 is a coherence time, T_2 is classically the time it takes for an ensemble of transverse electron spins, initially precessing in phase about the longitudinal field, to lose their phase due to spatial and temporal fluctuations of the precessing frequencies. In a population of two-state systems there is a qualitative

2.10 Longitudinal and transverse spin relaxation times

difference between T_1 and T_2 when the two states are different. In the presence of an external magnetic field the relaxation of a state occupation imbalance to equilibrium requires energy transfer between the spin system and another system and after the time T_1 have an inversion for state occupation. The decoherence of a phase relationship between the two states does not require energy transfer. In most cases, we have not real magnetic fields, but we can consider effective magnetic fields originating from the spin-orbit or exchange interaction. Then $B_{Ext} = 0$, but we have different energies for the two states due to the effective magnetic field (as discussed in appendices, Pages 139 and 149). After $T_1 \simeq T_2$ we have a state occupation balance.

We can define a randomly fluctuating magnetic field with a correlation time τ_c i.e. the time during which the field may be roughly considered as constant (50). The correlation time is of the order of the momentum relaxation time τ_p . The spin makes a precession around the (random) direction of the effective magnetic field with a typical frequency ω or period T_ω and during a typical time τ_c . After a time τ_c the direction and the absolute value of the field change randomly, and the spin starts its precession around the new direction of the field. After a certain number of such steps the initial spin direction will be completely forgotten. We can consider two limiting cases :

a) If $\tau_c \ll T_\omega$: In this case, the precession angle is small, so that the spin vector experiences a slow angular diffusion. During a time interval t , the number of random steps is t/τ_c and for each step the squared precession angle is $(\omega\tau_c)^2$. These steps are not correlated, so that the total squared angle after time t is $(\omega\tau_c)^2 t/\tau_c$. The spin relaxation time τ_s may be defined as the time at which this angle becomes of the order of unity: $1/\tau_s \sim \omega^2\tau_c$. This is the well-known expression for the spin relaxation time in the extreme motional narrowing case.

The D'yakonov-Perel mechanisms belong to this case.

b) If $\tau_c \gg T_\omega$: A spin will make many rotations around the direction of the magnetic field during the correlation time. During the time of the order of T_ω the average spin projection transverse to the random magnetic field is completely destroyed. After time τ_c the magnetic field changes its direction, and the initial spin polarization has disappear.

We can consider other possibilities, e.g. if the scattering mechanism itself has a finite probability of reversing the spin and the angle of rotation. The Elliot-Yafet, Bir-Aronov-Pikus mechanisms and the hyperfine interaction belong to this case. Where the spin relaxation time is proportional to the momentum relaxation time.

2.11 Spin relaxation mechanisms

We consider the five most important carrier spin relaxation scenarios for bulk materials and heterostructures :

1) The D'yakonov-Perel mechanisms for bulk material (51).

The main mechanism for electron-spin relaxation in semiconductor crystals lacking inversion symmetry is the D'yakonov and Perel mechanism. In this mechanism, the anisotropic term in the conduction-band dispersion, cubic in k , couples electron states of opposite spin. This interaction between conduction-band states may be looked at as an internal effective magnetic field, which is wave-vector dependent. At a given wave vector, the electron spin precesses around this field, which changes its direction with respect to the wave vector if the latter changes. Therefore, if the electron undergoes a scattering event, its momentum changes and the effective magnetic field fluctuates, causing spin relaxation. The spin-relaxation rate for this mechanism is predicted to be inversely proportional to

the carrier momentum relaxation time, leading to a phenomenon known as motional narrowing (see Appendix : [A](#)). We will use the concept of an "internal effective magnetic field" in order to explain exciton spin relaxation in CuCl (see chapter [5](#)).

2) Elliot-Yafet mechanisms ([52](#); [53](#); [54](#)).

The Elliot-Yafet mechanisms considers that coupling between conduction-band states with opposite spins becomes allowed because of a mixing of conduction-band and valence-band states with nonzero wave vector k . Using $k \cdot p$ perturbation theory, the spin-relaxation rate for this mechanism is predicted to be proportional to the carrier-momentum relaxation-time. This process is generally considered to be weak in bulk semiconductors when compared to the DP mechanism (see Appendix : [B](#)).

3) Bir-Aronov-Pikus mechanisms ([55](#)).

The BAP mechanism involves electron scattering on free or bound holes with spin flip. Scattering with paramagnetic impurities can play a similar role. This mechanism dominates at low temperatures and high doping levels (see Appendix [C](#)). The Bir-Aronov-Pikus mechanisms is essential only in p-doped samples, the study of which are beyond the scope of this thesis.

4) Spin relaxation mechanisms in symmetric and asymmetric quantum wells.

In two-dimensional systems the relative importance of the above mechanisms change dramatically because of the lifting of the degeneracy in the energy spectrum and because of spin-orbit interaction. A two-dimensional size-quantization suppresses the spin-orbit interaction for holes and increases its strength for electrons. For electrons in semiconductors with bulk inversion asymmetry, on the contrary to the three-dimensional case, the splitting between spin states becomes

a linear function of the wave vector (see Appendix : [D](#)).

5) Hyperfine interaction.

A serious possible limitation of spin coherence in semiconductors is the hyperfine interaction with surrounding nuclear spins. Hyperfine interaction is the coupling of a nuclear magnetic moment to the magnetic field provided by the (orbital and spin) magnetic moments of electrons. This is the magnetic interaction between electrons and nuclear spins, which may be quite important if the lattice nuclei in a semiconductor have non-zero spin (like in GaAs). If the nuclei get polarized, this interaction is equivalent to the existence of an effective nuclear field acting on the electron spin. Comparison with experiment shows that the hyperfine interaction with nuclei may be the dominant mechanism of electron spin relaxation in quantum dots. (see Appendix : [E](#)). To consider the hyperfine interaction is beyond the scope of this thesis.

2.11.1 Spin relaxation in semimagnetic semiconductors

Diluted magnetic or semimagnetic semiconductors such as $Cd_{1-x}Mn_xTe$ exhibit many interesting optical and magnetic properties. In this material, we have a spin-spin exchange interaction which exists between the carriers in the conduction and valence band (s- and p-like, respectively) of the host semiconductor with the local moments of the substitutional magnetic ions arising from the 3d electrons hence this interaction is referred to as sp-d exchange interaction. In 1990, Bastard and Chang ([56](#)) and in 1998 Linder and Sham ([57](#)) presented theoretical calculations of the spin-flip relaxation time of conduction electrons in $Cd_{1-x}Mn_xTe$ quantum wells and a theory of time-resolved Faraday rotation for semimagnetic quantum well, respectively. The Hamiltonian of a conduction electron in a semimagnetic quantum well such as $Cd_{1-x}Mn_xTe$ at zero magnetic field

is written as (57)

$$H = H_{QW} - \sum_{\vec{R}_i} J(\vec{r}_i - \vec{R}_i) (\vec{S}_i \cdot \vec{\sigma}_i) \quad (2.56)$$

Where \vec{S}_i and $\vec{\sigma}_i$ are the spin operators for the Mn^{++} ion and for the conduction band electron, respectively. $J(\vec{r}_i - \vec{R}_i)$ is the exchange integral, and \vec{r}_i and \vec{R}_i are the coordinates of the conduction band electron and the Mn^{++} ion, respectively. The summation is only over the lattice sites occupied by the Mn^{++} ions. Because of $(\vec{S}_i \cdot \vec{\sigma}_i)$ in the Hamiltonian, we have spin-flip transition probabilities which are $\neq 0$ (57). Recently, electron-and hole-spin relaxation times in n-type and p-type CdMnTe quantum wells with nonmagnetic barriers measured via the time-resolved magneto-optical Kerr effect, have been studied (58). They have found the fast increase of the electron relaxation rate τ_e^{-1} and the decrease of the hole relaxation rate τ_h^{-1} as the Mn concentration increases, respectively. In other words, τ_h becomes even longer than τ_e in undoped or p-doped samples. In our sample with nonmagnetic wells and semimagnetic barrier layers we can not consider this exchange scattering rate, but if the carrier wave functions penetrate into the barrier, this exchange scattering probability is important. In chapter 6, we consider this mechanism, as a possibility to explain long and short spin relaxations times of hole and electron, respectively.

Chapter 3

General Experimental Methods

In this chapter, we discuss the general experimental techniques and apparatus which have been applied to the study of population and spin dynamics in bulk and multiple quantum well semiconductors. Ultrafast lasers were used to produce short pulses of approximately 170 fs duration for studies of bulk CuCl and 30 fs for CdTe\CdMnTe multiple quantum well. This allows the resolution of carrier dynamics on this timescale.

3.1 Pump-Probe spectroscopy

In pump-probe spectroscopy, a light beam, referred to as the "probe" beam, is used to monitor the changes in the optical properties of a sample caused by a pump beam. The probe intensity is very small, not inducing any changes in the sample. The transmission spectrum of the probe beam detected in presence of the pump beam is compared to the spectrum without pump beam, giving the frequency-dependent transmission of the sample for different intensities of the pump. A differential transmission spectrum (DTS) is the difference between the

3.1 Pump-Probe spectroscopy

probe transmission with and without the pump,

$$DTS = \frac{|E(\omega)|_{\text{pump on}}^2 - |E(\omega)|_{\text{pump off}}^2}{|E(\omega)|_{\text{pump off}}^2} \quad (3.1)$$

Here $E(\omega)$ denotes the amplitude of the probe field after passing through the sample. The DTS described by Eq. (3.1) depends implicitly on the time delay T_P between pump and probe. In experiments, the DTS is measured at various time delays. To obtain the basic information contained in DTS, let us assume that the pump-induced changes in the probe transmission are small at early time delays. Then we can write

$$|E(\omega)|_{\text{pump off}}^2 = |E_0|^2 e^{-\alpha d}, \quad (3.2)$$

Where E_0 is the amplitude of the incident field, and α is the linear absorption coefficient. Furthermore,

$$|E(\omega)|_{\text{pump on}}^2 = |E_0|^2 e^{-(\alpha + \Delta\alpha)d}, \quad (3.3)$$

Where $\Delta\alpha$ are the pump-induced absorption changes. Inserting Eq. (3.2) and Eq. (3.3) into Eq. (3.1) yields

$$DTS = e^{-\Delta\alpha d} - 1, \quad (3.4)$$

If we again assume the pump-induced changes to be small, Eq. (3.4) becomes

$$DTS = -\Delta\alpha d, \quad (3.5)$$

indicating that for incoherent processes DTS is directly proportional to the absorption changes generated by the pump pulse.

3.2 The laser source

Ultrashort pulse sources are becoming increasingly more useful in various fields of research. For instance, pulses of such short duration can be used to achieve a remarkable time-resolution of processes occurring in semiconductors. During the 1980s new solid-state broad-bandwidth materials were developed. These new materials renewed the interest in ultrashort pulse generation since their broad fluorescence emission showed potential to support light pulses of only a few femtoseconds in duration. The most significant of these new transition-metal doped materials was titanium-doped sapphire. The wavelengths in which Ti:sapphire will produce gain stretch from 660 nm to 1180 nm, giving a bandwidth of over 400 nm. The material characteristics of Ti:sapphire, namely a broad gain bandwidth, a large energy storage density, and excellent thermal properties, make it an excellent candidate to be used in femtosecond laser and amplification systems. These lasers are much more stable than dye lasers which were used earlier. To investigate femtosecond dynamics we use an ultrafast Ti:sapphire laser system.

3.2.1 Femtosecond pulse generation

There are several methods by which pulsed output can be generated, for example Q-switching and mode-locking. A multi-mode laser is said mode-locked if its modes have a well-defined and fixed phase relationship in between each other. If the phases are locked in such a way that there is a constructive interference between the modes at an instant and a destructive interference at other times, the output will appear as a pulse. There are several techniques by which mode-locking can be achieved. In our experiment, we make use of a self-mode-locking mechanism that relies on the optical Kerr effect inside of the active medium. The optical Kerr effect is a third-order, non-linear effect which results in a change

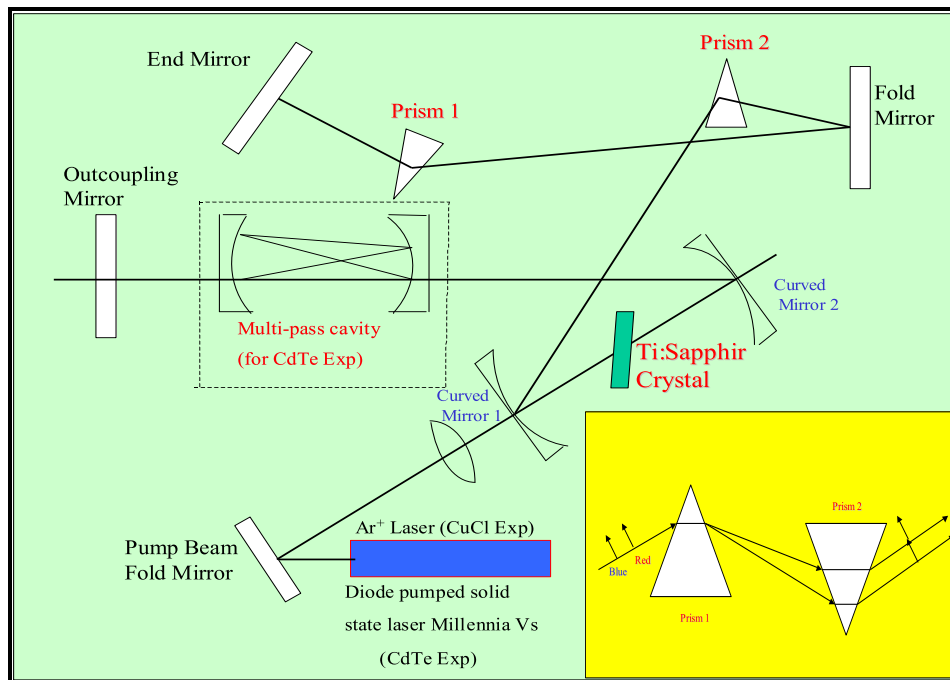


Figure 3.1: Schematic diagram of the laser. For CdTe\CdMnTe experiments we added a multi-pass cavity in order to reduce the repetition rate of the laser and increase the energy per pulse (59). The inset shows a prism pair for group velocity dispersion compensation. In front of prism 1, the red components of a pulse are ahead of the blue components and behind prism 2 red and blue components of the pulse coincid temporaly.

in the refractive index of a material induced by an applied high-intensity electromagnetic fields. The spatial modulation of the index of refraction results in creation of a “lens” in the medium and leads to self-focusing. The behavior of the refractive index under the Kerr effect is intensity dependent and can be described by:

$$n(I) = n_0 + n_2 I, \quad (3.6)$$

where n_0 is the linear refractive index, n_2 is the nonlinear refractive index coefficient, and I is the instantaneous beam intensity.

Let us consider a Gaussian mode in a nonlinear medium. Since the central portion of the mode has the highest intensity, it experiences a larger index of refraction than in the wings where the intensity is weaker. Thus the material itself acts as an intensity-dependent (Kerr) lens and the mode becomes “self-focused” within the crystal. Self focusing in the cavity leads directly to fast saturable absorption-type modelocking behavior. Kerr-lens modelocking of solid state lasers has been the most successful approach for short pulse generation.

3.2.2 Ultrafast laser system

The basic requirements of the lasers we used for the experiments are similar. If we consider the ensemble of our sources to produce ultrashort pulses, as “one laser”, they comprise:

1- A source of pumping energy :

For the CuCl experiments this source is a Ar^+ laser and for the CdTe\CdMnTe experiments this source is a diode pumped solid state laser (Millennia V_s).

2- An active medium :

For our experiments this active mediums are titanium-doped sapphire ($\text{Ti:Al}_2\text{O}_3$) crystals. Furthermore, these crystals play the role of Kerr-lenses in the cavity.

3-An optical cavity :

For CuCl experiments this optical cavity is a normal cavity. The total length of our cavity is about 3 m and it produces 80 fs pulses at a repetition rate of 80 MHz. This spectrally broad femtosecond pulses are amplified in a regenerative amplifier which produces 170 fs pulses of the frequency doubling at a repetition rate of 200 KHz. For CdTe\CdMnTe experiments we added a multi-pass cavity in order to reduce the repetition rate and to increase the energy per pulse (59). The total length of our cavity is about 11.6 m and it produces 30 fs pulses of 15nJ at a repetition rate of 13 MHz.

3.2.3 Group Velocity Dispersion Compensation

In order to successfully generate ultrashort pulses, the modes must retain their phase relationship over along time so that the mode-locking is stable. This requires that all modes experience the same round-trip cavity time, or, equivalently, that the optical length of the cavity is independent of frequency. In general, group velocity dispersion is detrimental to the stability of a short pulse system, since it introduces a phase delay between the different radiation modes and, therefore, it tends to destroy (after a few round trips) the positive interference. Undesirable group velocity dispersion can be compensated in a number of ways. Group velocity dispersion compensation is generally achieved by introducing a prism pair into the cavity. A pair of prisms compensates for normal group velocity dispersion, which leads to a delay of the red components of a pulse with respect to its blue components (see fig. 3.1).

3.3 Pulse-Duration Measurement

Since electronic devices are too slow for temporal measurements of femtosecond laser pulses, one must resort to nonlinear optical techniques. The basic idea is to convert a measurement in the time domain into a measurement in the space domain by increasing the path of part of the optical pulse with respect to the rest of the pulse, and to convert this path delay into an electric signal directly proportional to the path delay.

The most commonly used method is the autocorrelation technique based on second-harmonic generation. A transparent medium having no inversion symmetry generates light at the harmonic frequency 2ω , if it is irradiated with intense light at frequency ω . It is important to realize that this harmonic generation occurs only during the presence of the radiation at ω . Light at frequency 2ω will be emitted preferentially in certain directions that satisfy the phase-matching condition $n(\omega) = n(2\omega)$. The phase-matching condition translates the fact that both beams with ω and 2ω propagate with the same phase velocity, so that energy transfer can occur constructively from the beam with frequencies ω to 2ω . If the phase-matching condition is not satisfied, the harmonic generated light at a given location x in the crystal will interfere destructively with the harmonic generated at location $x+\delta$, where δ is the coherence length (defined as $\delta = 2\pi\Delta k$, where $\Delta k = k(2\omega) - 2k(\omega)$), with the net result that very little harmonic light will emerge from the crystal. To satisfy the phase-matching condition, one selects a birefringent crystal having two different refractive indices, the ordinary and extraordinary index for orthogonal polarization directions, and chooses the incident light propagation vector such that the ordinary index at ω and extraordinary index at 2ω are equal.

The principle of an autocorrelator is shown in Fig(3.2). The optical pulse

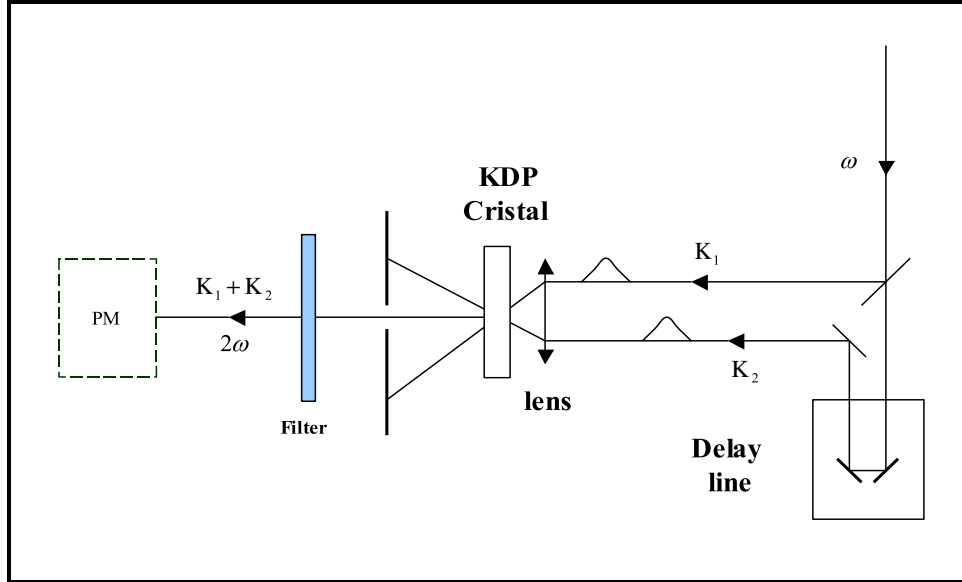


Figure 3.2: Schematic setup of an autocorrelation technique for measuring pulse durations. Beams K_1 and K_2 are focused on a second-harmonic generating crystal like BBO with a variable time delay.

to be measured is divided into two pulses of equal intensity. After delaying one pulse with respect to the other, both pulses are recombined in a nonlinear crystal, transparent at both frequencies ω and 2ω , usually a **BBO** crystal that is oriented for phase matching. This second-harmonic light resulting from the time overlap between both pulses is detected with a photodetector. Using this technique we determine pulse duration of 30 fs for test-pump experiments on CdTe\CdMnTe multiple quantum well. For test-pump experiments on CuCl, we use a similar cross-correlation technique between pulse at 390 nm and at 780 nm and we find 170 fs for the 390 nm pulse duration.

3.4 Cryostat

Our experimental results are measured at temperatures between $T=4$ and 40 K using a MicrostatHe cryostat. The vacuum loading MicrostatHe cryostat is

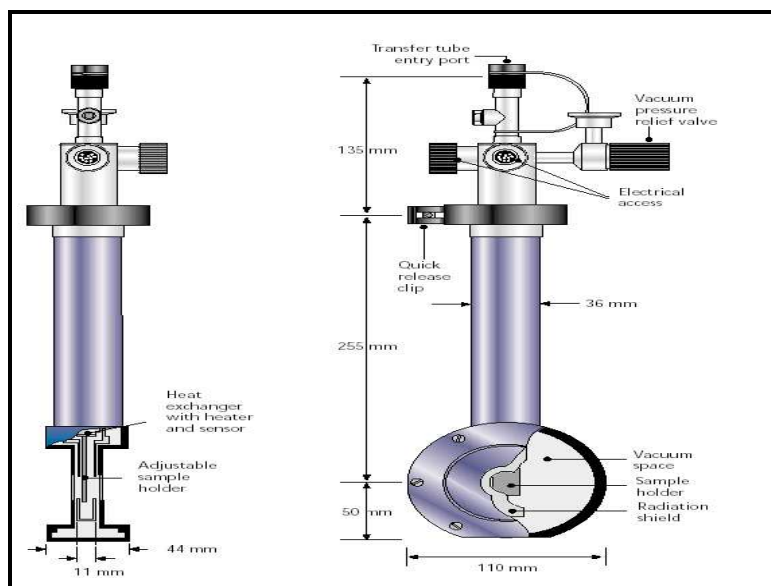


Figure 3.3: The vacuum loading MicrostatHe cryostat.

specifically designed for microscopy applications requiring temperatures down to 2.2 K. The MicrostatHe (Fig. 3.3) is a vacuum loading continuous flow cryostat. Liquid cryogen is drawn from a helium or nitrogen storage dewar and circulated through the heat exchanger in the cryostat. The cryogen flow is regulated by needle valves on the transfer tube and in the exhaust line. Precise temperature control is obtained using a temperature controller. The sample is positioned on the sample holder that is in good thermal contact with the heat exchanger. The sample holder is surrounded by the cryostat vacuum. To change the sample, the cryostat is warmed to room temperature, the vacuum released and the outer vacuum case and radiation shield removed. The cryostat may be operated in any orientation. The sample holder in the MicrostatHe is adjustable to optimise the optical access of the cryostat for different sample thicknesses.

3.5 The experimental set-up and sample: CuCl

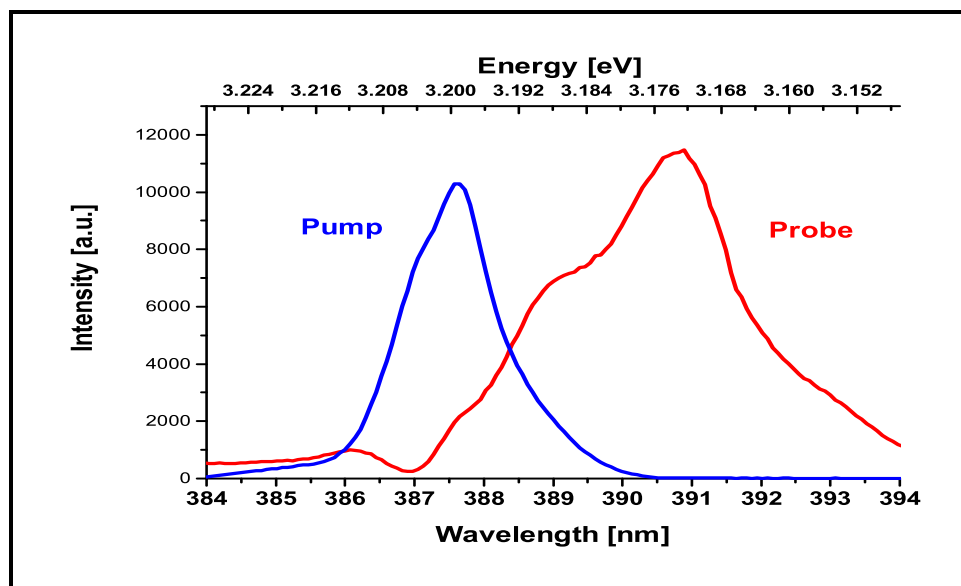


Figure 3.4: The pump pulse spectral intensity, in resonance with the exciton transition, and the probe pulse covers the exciton-biexciton transition for experiments on CuCl.

3.5 The experimental set-up and sample: CuCl

The experimental set-up used for experiments on CuCl is sketched in Figure (3.5): spectrally broad femtosecond pulses of a self mode-locked Ti: Sa laser are amplified in a regenerative amplifier and frequency doubled using a BBO crystal. The frequency of the pump laser pulses have a full width at half maximum (FWHM) of about 15 meV and the excitation covers entirely the exciton resonance (Fig.3.4).

When increasing the temperature, the photon energy of the central frequency of the laser is changed in order to follow the exciton resonance, which shifts towards higher photon energies in CuCl. The pump pulses pass an optical delay line and a linear polarizer, followed by a $\lambda/4$ plate. They are circularly polarized with σ^+ helicity and focused onto the sample surface into a spot of about 100m diameter. From the amplified laser emission a beam splitter separates a small part and a probe beam is generated using a second BBO crystal. The probe beam

3.5 The experimental set-up and sample: CuCl

(15 meV FWHM) is centered at the spectral position of the induced absorption band of the exciton-biexciton transition, which is situated around 3.1695 eV at 4K. The linearly polarized light passes successively a $\lambda/2$ plate and the $\lambda/4$ plate. It is focalized onto the surface of the CuCl crystal into the spot excited by the pump beam. The probe pulses have either σ^+ or σ^- helicities. Probe and pump pulses have a duration of 170 fs.

The crystal surfaces of the CuCl platelets have (111) orientation, and all polaritons propagate almost perpendicular to it. The probe transmitted by the sample is spatially filtered and time-integrated, but spectrally resolved by a spectrometer and a cooled CCD camera. We measure separately the intensity of the probe pulse when transmitted through the sample without excitation by the pump pulse (noted I_T) and with pump-pulse excitation at a time delay t between the pulses (noted $I_T^L(t)$). In addition, we determine the time integrated sample emission and the diffused light I_{Str} which are due to the pump-pulse excitation alone. We subtract I_{Str} from $I_T^L(t)$ and obtain the induced change of the transmitted intensity by:

$$I_{Ind}(t) = I_T^L(t) - I_{Str} - I_T \quad (3.7)$$

We then calculate its induced transmission change $\Delta T(t)$

$$\Delta T(t) = \frac{I_{Ind}(t)}{I_T} \quad (3.8)$$

ΔT is negative if the probe pulse is subject to induced absorption and positive if the pulse is amplified due to optical gain at the photon energy considered (60). Then, the induced probe-beam transmission is analyzed as function of time delay t between the two incident pulses for both polarization sequences $\sigma^+\sigma^+$ and $\sigma^+\sigma^-$. In addition, the measurements are repeated for different excitation intensities and sample temperatures. The overall temporal resolution is about

3.6 The experimental set-up and sample: CdTe/CdMnTe multiple quantum well

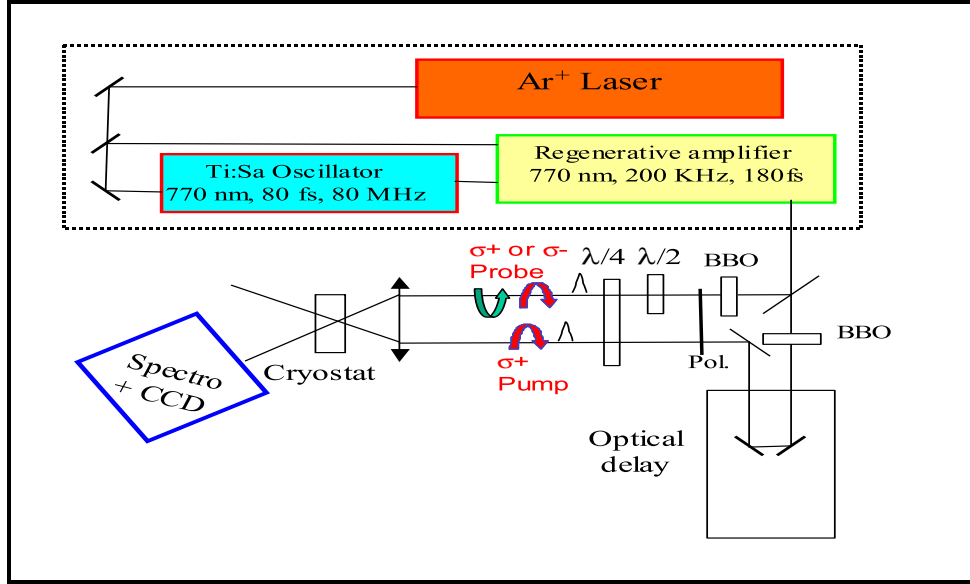


Figure 3.5: Experimental setup : CuCl

0.3ps and the spectral resolution 0.6meV.

We study freestanding CuCl platelets, which were grown by vapor phase transport in a closed tube containing H_2 and CuCl powder (23). From the study of interference fringes due to reflections from the front and rear surfaces of our samples, they turn out to be quite inhomogeneous in thickness with a mean value of about $20 \mu\text{m}$.

3.6 The experimental set-up and sample: CdTe/CdMnTe multiple quantum well

As shown in Fig. 3.6 along with the absorption of the sample, the pump pulse is in resonance with the $HH_1 - E_1$ transition, this permits the excitation of only the $HH_1 - E_1$ excitonic transition. The probe beam is linearly polarized, before impinging onto the sample Fig. 3.7. A quarter wave-plate transforms the two circular components of the transmitted probe beam into two linearly polarized,

3.6 The experimental set-up and sample: CdTe/CdMnTe multiple quantum well

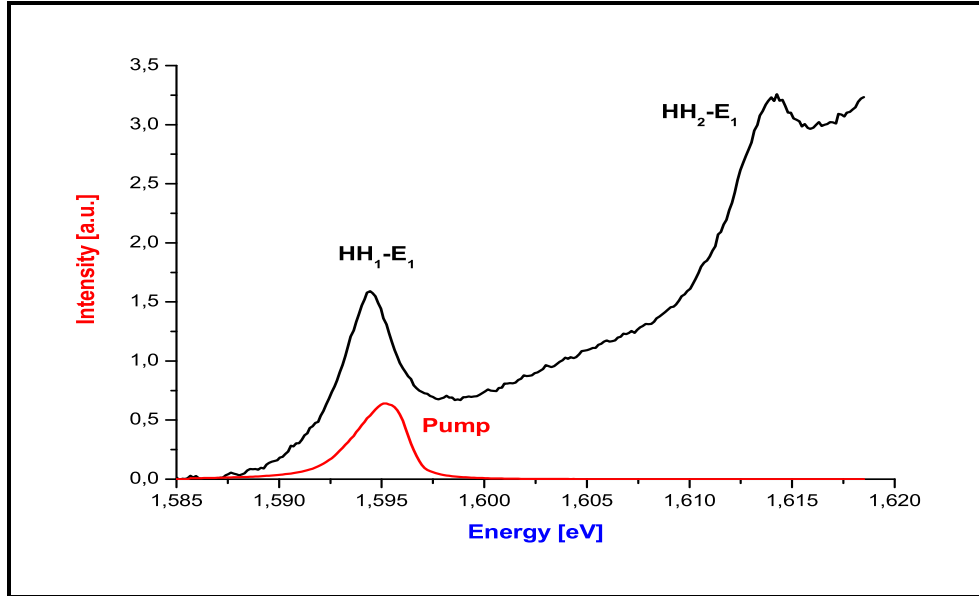


Figure 3.6: Absorption profile of the CdTe/CdMnTe multiple quantum well structure at the $HH_1 - E_1$ and $HH_2 - E_1$ transition. The pump pulse spectral intensity, in resonance with the $HH_1 - E_1$ transition, is also shown as a dotted line.

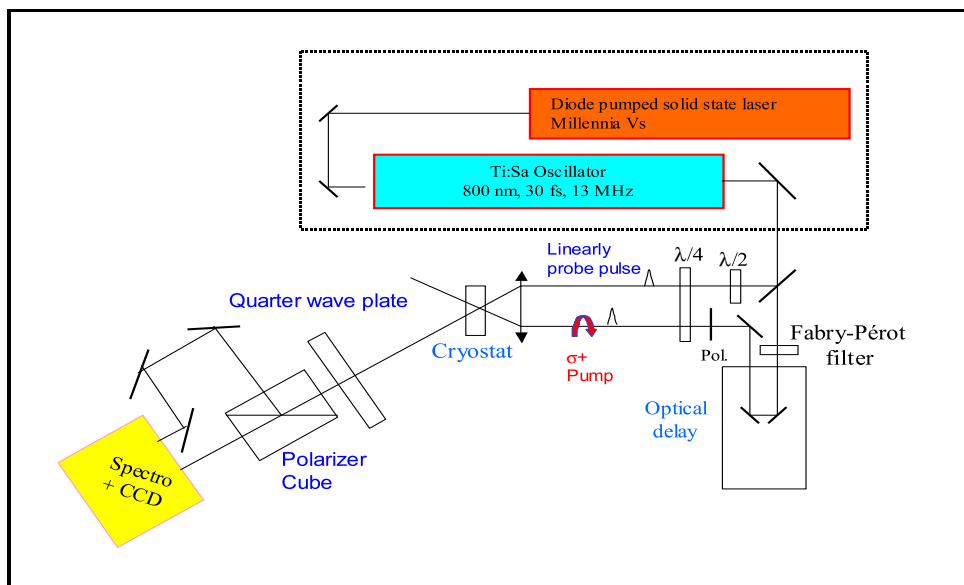


Figure 3.7: The experimental set-up: CdTe/CdMnTe multiple quantum wells

3.6 The experimental set-up and sample: CdTe/CdMnTe multiple quantum well

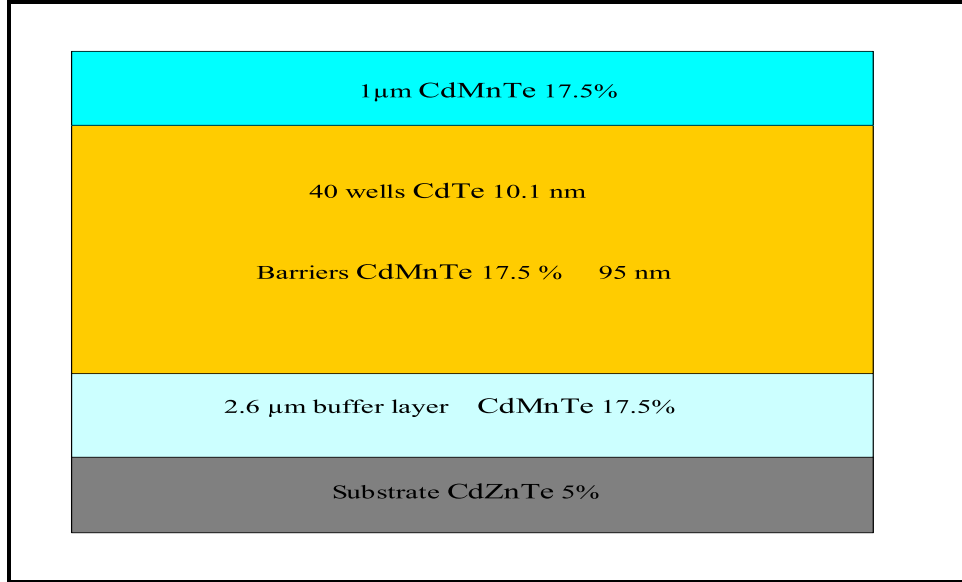


Figure 3.8: The CdTe/CdMnTe multiple quantum well consisting of 40 periods of 10.1-nm-wide CdTe quantum wells, with 95 nm $Cd_{0.83}Mn_{0.17}Te$ barriers, grown by molecular beam epitaxy on a 2.6- μ -thick $Cd_{0.83}Mn_{0.17}Te$ buffer layer and a $Cd_{0.95}Zn_{0.05}Te$ (111)-oriented substrate.

mutually perpendicular components, which are separated by a linear polarizer cube. The two beams are then directed at different heights onto the entrance slit of a spectrometer, and detected as two different spectra on our two dimensional CCD detector.

In this way, the two circular components of the transmitted probe are detected simultaneously as function of the pump-probe time-delay. Our sample (Fig. 3.8) consists of 40 periods of 10.1-nm-wide CdTe quantum wells, with 95 nm $Cd_{0.83}Mn_{0.17}Te$ barriers, grown by molecular beam epitaxy on a 2.6- μ m-thick $Cd_{0.83}Mn_{0.17}Te$ buffer layer and a $Cd_{0.95}Zn_{0.05}Te$ (111)-oriented substrate. A 1- μ m-thick $Cd_{0.83}Mn_{0.17}Te$ cap layer was added to eliminate the influence of the electric field due to surface charges on the quantum wells. For details of the growth conditions, see Ref. (61).

Chapter 4

Spin population and propagation dynamics of polaritons in CuCl

4.1 A new method to determine the spin-relaxation dynamics

The spin-relaxation processes of electrons, holes, and excitons have been intensively studied in III-V and II-VI semiconductors and in other materials in order to specify the mechanisms, responsible for the time evolution of the total angular momentum (or pseudo-spin) of an excited state.

To our knowledge, such studies have not been performed on I-VII compounds up to now. Direct, large band gap semiconductors show very high absorption coefficients (for CuCl we have: $\alpha \sim 10^5 \text{cm}^{-1}$) close to their band edge (see Fig. 4.1). Therefore, spin relaxation times can not be determined in such bulk material by classical methods as, for example, degenerate pump-probe experiments (62; 63; 64), time-resolved Faraday rotation (65; 66), or time-resolved photoluminescence measurements (67; 68; 69). In this thesis we present a new method to determine the spin-relaxation dynamics through induced absorption in non-degenerate pump-probe experiments (60). Using this method, we study the dynamics of a system consisting of exciton polaritons and biexcitons in bulk

4.1 A new method to determine the spin-relaxation dynamics

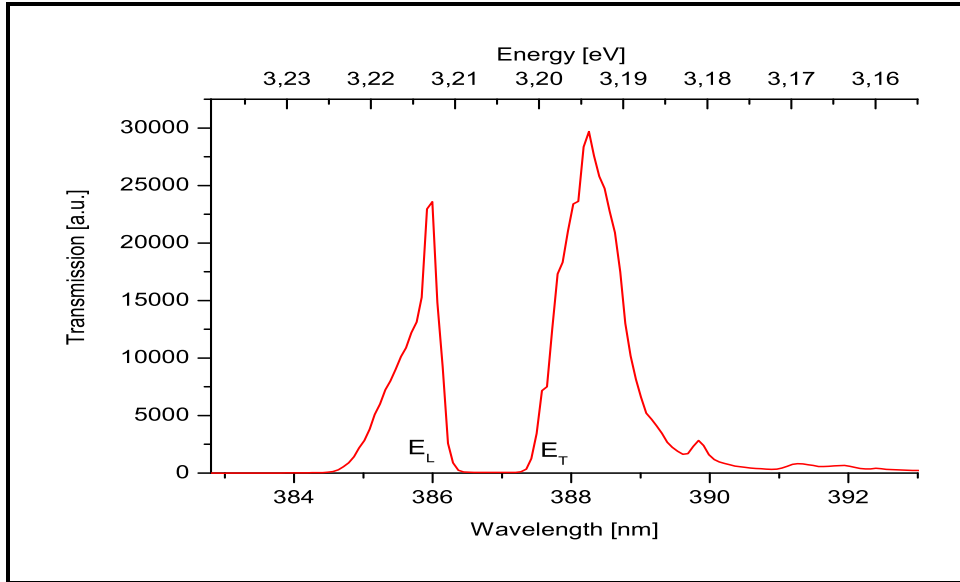


Figure 4.1: Linear transmission spectrum of CuCl at 5 K.

semiconductors. The polariton dispersion curve is scanned in a pump and probe experiment by looking at different excitation and detection wavelengths. This allows us to determine the influence of the polariton wave vector on polariton-spin relaxation processes and on their overall population dynamics. We evaluate how the optical properties close to the exciton resonance develop in time from induced absorption to gain, depending on the wavelength and the intensity of excitation. This allows us to determine the polariton- and biexciton-population relaxation dynamics inside the bottleneck spectral region, their spin dynamics, and reveals the importance of propagation effects.

As indicated schematically in Fig. 4.2, biexcitons may be excited from the crystal ground state either by two polaritons of parallel linear polarization or from two circularly polarized polaritons of *opposite helicity*. This absorption process can be performed either simultaneously as in a two-photon absorption or in a two-step process where first a population of polaritons of a well defined helicity

4.1 A new method to determine the spin-relaxation dynamics

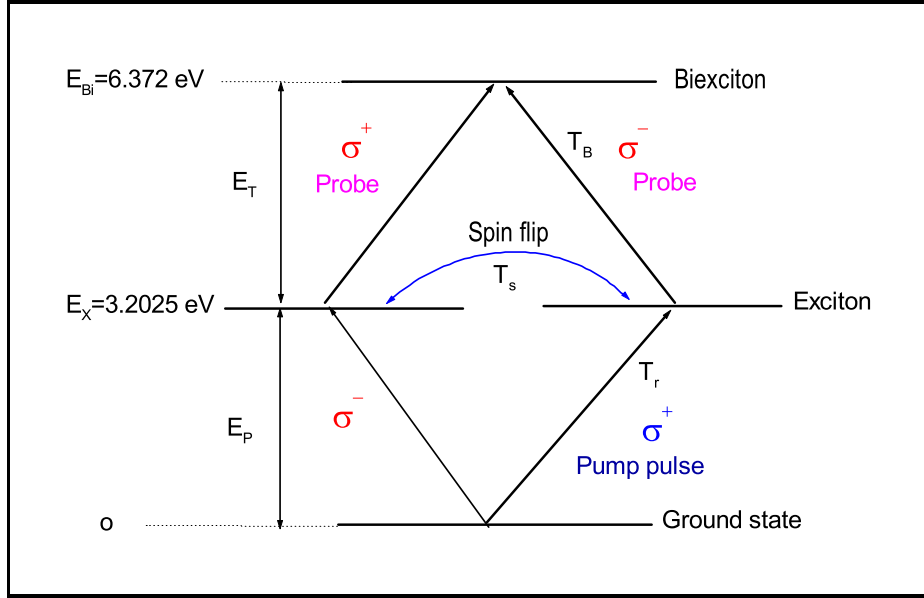


Figure 4.2: Level scheme of excitons and biexcitons together with the optical transitions used in the experiments

and energy is created. We will concentrate here on this second process. This population of polaritons with a well defined helicity, is probed by absorption of polaritons from a second pulse, which induces the transition to the biexciton state obeying to energy and momentum conservation. Depending on the polarization of the second (probe) pulse, its induced absorption at the exciton-biexciton transition will vary in time with the spin-flip of the exciton population. This allows to follow the dynamics of the exciton spin-relaxation.

We apply this technique to CuCl, which has a particularly simple band structure. This simplification is, however, not necessary for the application of this technique. In general, it is only necessary that systems possess transitions, which are mutually allowed or forbidden for the different spin polarizations. Using this technique, we perform the first measurements of spin-relaxation times in CuCl (60).

If E_p denotes the photon energy of polaritons created by the pump beam and

4.1 A new method to determine the spin-relaxation dynamics

E_t that from the probe beam, energy conservation implies that:

$$E_p(K_p) + E_t(K_t) = E_{Bi}(K_p + K_t) \quad (4.1)$$

We will make full use of Eq.4.1 throughout the analysis of our results. When discussing the absorption processes, we treat E_{Bi} as a constant, and neglect for sake of simplicity its wave vector dependence. This is possible since the biexciton dispersion is rather flat and the polariton wave vectors K_p and K_t are small, close to the center of the Brillouin zone. Fig. 4.3 gives the spectrally and temporally resolved transmission changes for the $\sigma^+\sigma^-$ configuration and Fig. 4.4 that for the $\sigma^+\sigma^+$ configuration measured under the same conditions at 4K and with an excitation intensity of 2.66 mW/cm² in a contour plot. The different colors are given in a linear scale between -0.15 (black, corresponding to induced absorption) and +0.1 (white, due to bleaching of absorption or optical gain). In order to facilitate the interpretation of the differential transmission spectra we give also the time integrated photoluminescence (PL) of the sample. The polarizations of the PL spectra are not resolved. The figures clearly indicate that the induced absorption is spin dependent. As discussed in more details in section 2.3, the polaritons have a group velocity and a density of states which depends on their photon energy. They are therefore influenced in different ways by surface effects, lattice defects, scattering with phonons or other excitons or polaritons. The competition between the scattering processes leads to different gain and induced absorption dynamics, which are characteristic for the spectral regions tested by the probe beam. We attribute the differences in the spectra to the propagation and collision properties of the polaritons in different spectral regions. They are noted A, B, C-I, and C-II in the following and are indicated schematically in Fig. 4.5.

4.1 A new method to determine the spin-relaxation dynamics

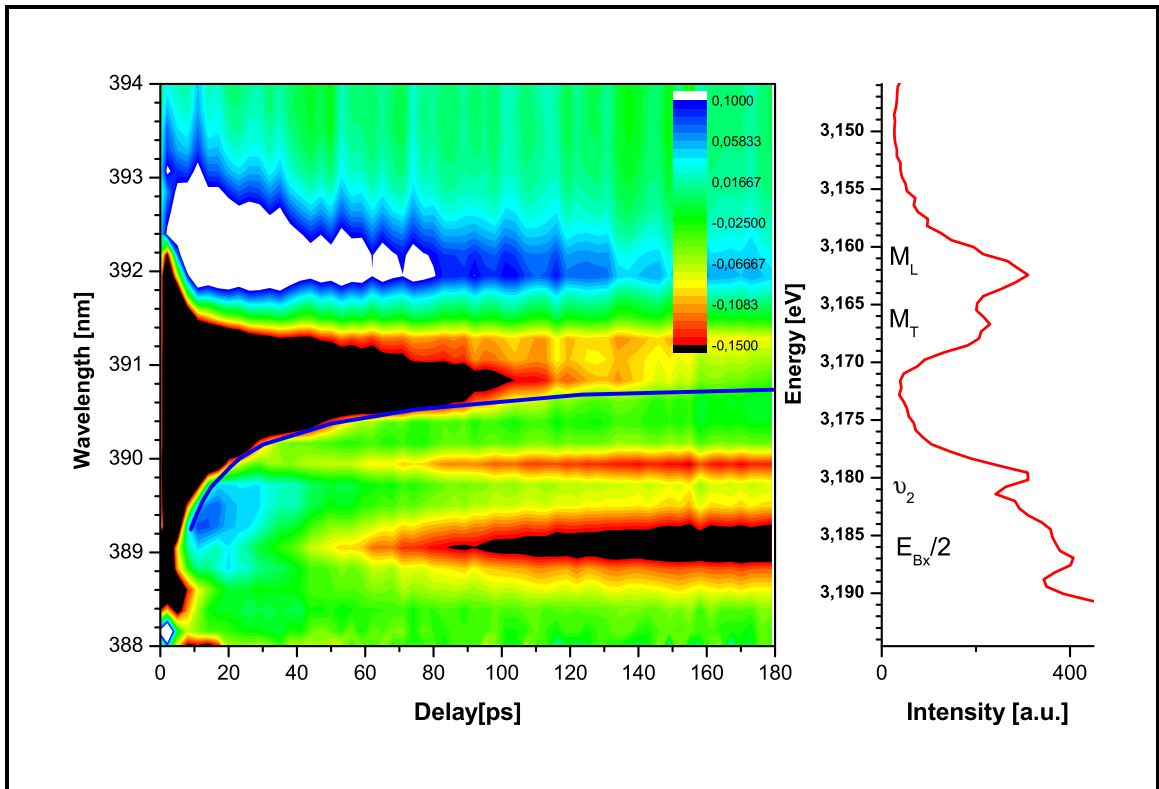


Figure 4.3: Left panel: Differential transmission of a CuCl platelet at 4K, measured the $\sigma^+\sigma^-$ configuration of the pump and probe beams, as a function of the delay between the pulses and of the wavelength of the transmitted light. The black line gives the time necessary for a polariton to cover $35 \mu\text{m}$, calculated from the group velocity. Right panel: Luminescence spectrum of the sample at 4 K showing important recombination lines.

4.1 A new method to determine the spin-relaxation dynamics

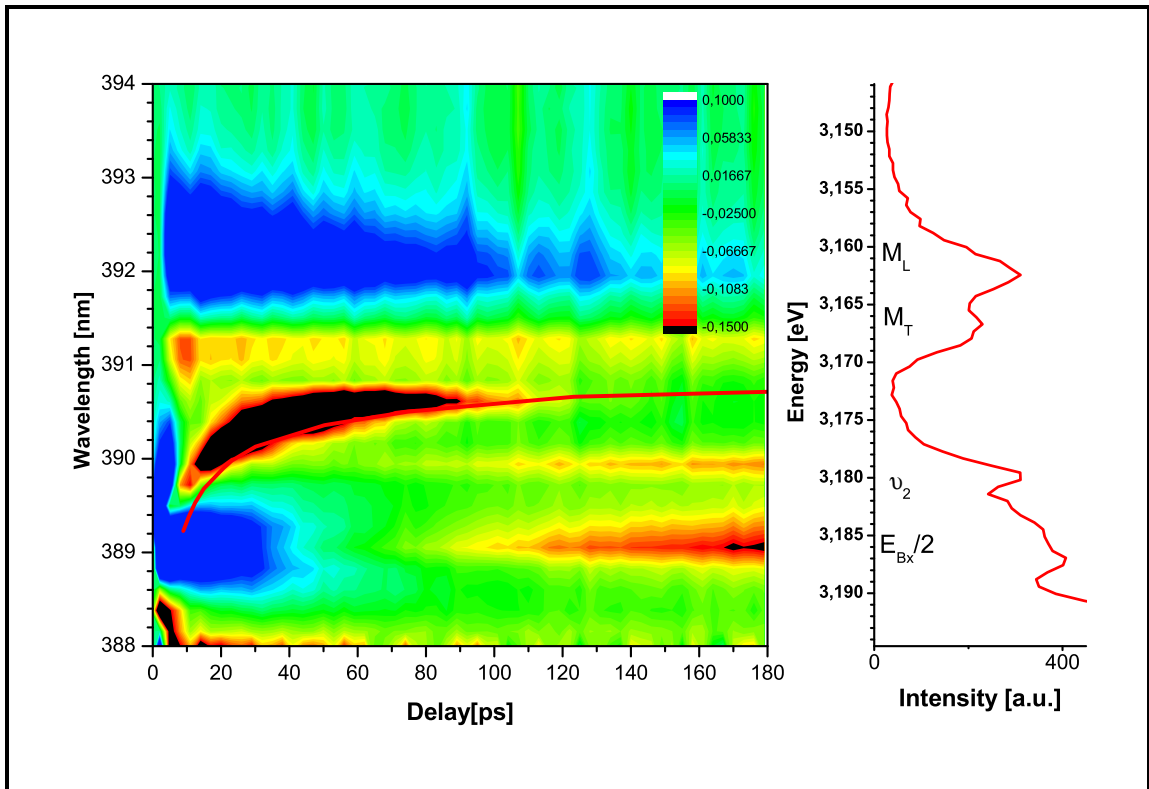


Figure 4.4: Left panel: Differential transmission of a CuCl platelet at 4K, measured the $\sigma^+\sigma^+$ configuration of the pump and probe beams, as a function of the delay between the pulses and of the wavelength of the transmitted light. The black line gives the time necessary for a polariton to cover $35 \mu\text{m}$, calculated from the group velocity. Right panel: Luminescence spectrum of the sample at 4 K showing important recombination lines.

4.2 Region A (Surface effects)

Let us first discuss our results obtained for 4K in region A. Fig. 4.6 shows the induced transmission changes for an excitation intensity of 0.5 mW/cm^2 for the $\sigma^+\sigma^+$ configuration (noted $\Delta T^{++}(t)/T$), for the $\sigma^+\sigma^-$ configuration (noted $\Delta T^{+-}(t)/T$), and their sum. The photon energy of the probe beam considered here is $E_t = 3.178\text{eV}$. Let us first consider the case that the probe pulse has a σ^- helicity. As discussed above, energy and wave vector conservation imply that $E_p(K) + E_t(K') = E_{Bi}(K + K')$ where $E_p(K)$ denotes the photon energy of the polaritons created by the pump beams with wave vector K and $E_t(K')$ that of the probe pulse with wave vector K' . Since the wave vectors of all polaritons are very small, $E_{Bi}(K + K') = E_{Bi}(0) = 6.372\text{eV}$ and the pump pulse polaritons, which have a photon energy $E_p = 3.194\text{eV}$ and were created with σ^+ helicity may undergo a transition to biexcitons by absorption of a polariton from the probe pulse which has a σ^- helicity. If polaritons from the pump pulse have performed a spin-flip process, the transition to biexcitons is forbidden in the $\sigma^+\sigma^-$ configuration and they do not contribute to induced absorption. They may, however, lead to induced absorption of polaritons from a probe pulse of σ^+ helicity. Fig. 4.6 shows that the quantity $\Delta T^{+-}(t)/T$ is minimum after the end of the pump pulse and then increases, corresponding to a diminishing of the initially by the pump pulse created density of polaritons. On the contrary, $\Delta T^{++}(t)/T$ is equal to 0 at the end of the pump pulse and then decreases. The sum of $\Delta T^{+-}(t)/T + \Delta T^{++}(t)/T$ remains almost constant. This indicates that a spin-flip occurs which is the main relaxation process, while the density of polaritons created by the pump pulse is constant on this time scale. Then, after about $t_d = 15\text{ps}$, the absolute value of transmission changes decrease drastically

4.2 Region A (Surface effects)

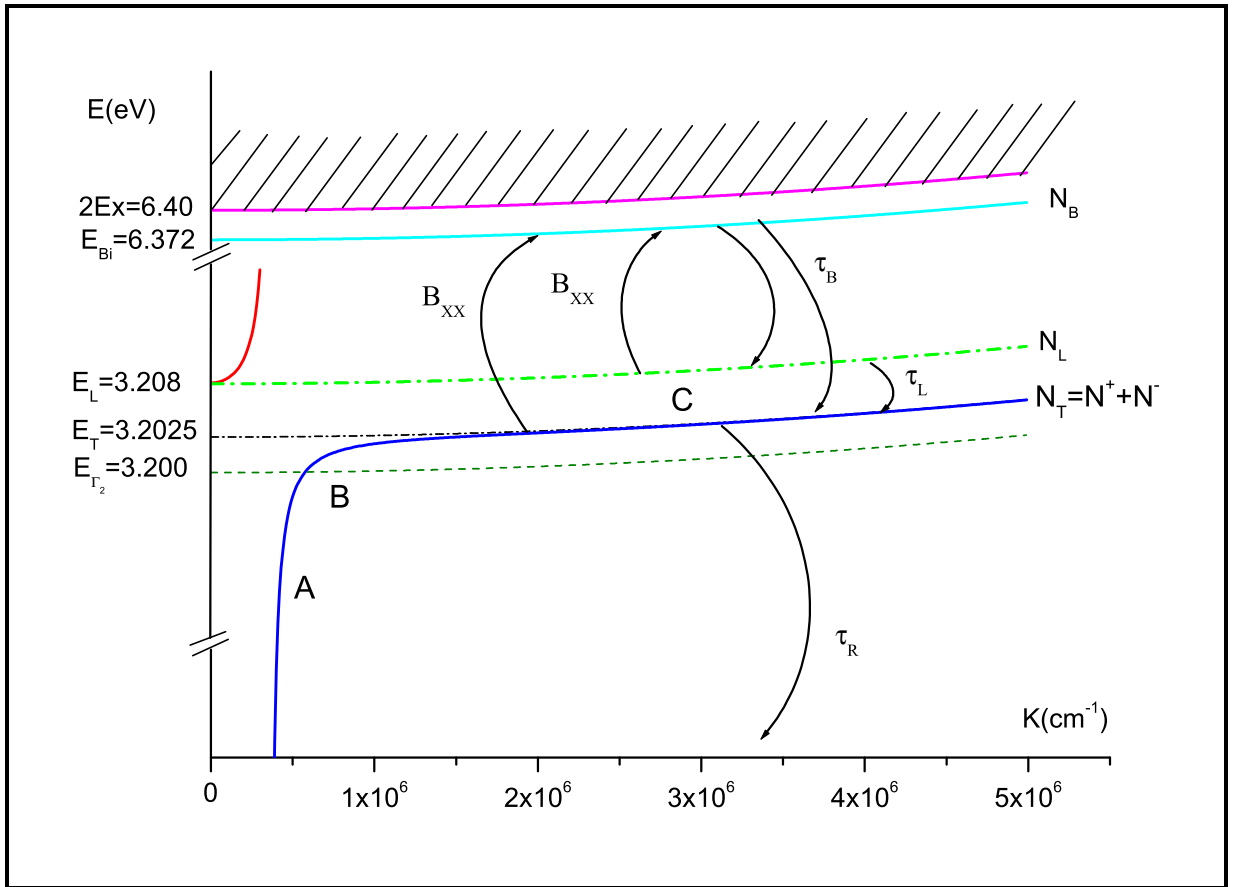


Figure 4.5: Polariton dispersion $E(K)$ in the vicinity of the bottleneck region calculated from the parameters of CuCl using the one oscillator model. A, B, and C denote the region of fast ballistic polaritons, the spin-flip region, and the bottleneck region, respectively (see text). N_i and τ_i denote different relaxation times and B_{XX} the probability of biexciton formation (see text).

for both configurations to values at which they remain almost constant. This scenario remains unchanged when pump pulse photons of higher energies (up to 3.1992eV) are analyzed. The main difference is that the drop at t_d happens later and the increase after t_d is slower.

4.2.1 Modeling of region A (Surface effects)

Our explanation for the results in region A is the following: The polaritons created by the pump pulse propagate almost freely before they arrive at the rear surface of the sample. Their propagation is ballistic, i. e. their wave vector is constant and we may call them ballistic polaritons. During the propagation time, these polaritons mainly undergo spin-flip scatterings. At the surface, they are either transmitted (and thus lost for the induced absorption of the polaritons from the test pulses) or they are scattered. In the latter case, as shown by the results in Fig. 4.6, their polarization memory is destroyed. As indicated schematically in Fig. 2.4 the group velocity of the polaritons in region A is very high. Due to the polariton effect it depends strongly on the photon energy and decreases when approaching the energy of the transverse exciton (70). We find, however, for pump photons with $E_p = 3.199$ eV (region A in Fig. 4.5) that the product: $V_g(E_p) \times t_d = 18.5 \pm 1.5 \mu m = d$ is constant and independent of the photon energy E_p . This value is in close agreement with that of the sample thickness d estimated from the observed interference fringes discussed above. The polaritons from the test pulses have group velocities, which are always at least one order of magnitude bigger than that of the pump pulses and their propagation time can be neglected.

4.3 Region B (Spin-flip region)

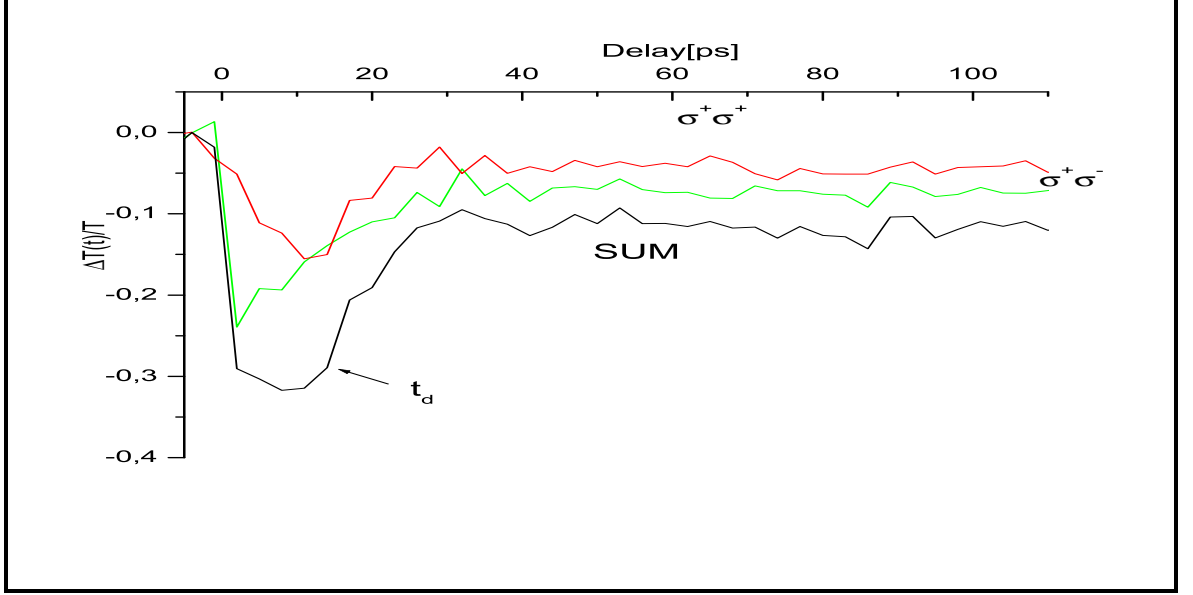


Figure 4.6: Induced transmission changes for the $\sigma^+\sigma^+$ configuration, for the $\sigma^+\sigma^-$ configuration, and their sum as function of time delay between the pulses. The photon energy of the probe beam is $E_t = 3.178\text{eV}$. The polaritons of the pump pulse which are tested have photon energies $E_p = 3.194\text{eV}$ (Region A).

4.3 Region B (Spin-flip region)

As shown in Fig. 4.7 for $E_t = 3.1715\text{ eV}$, the induced absorption dynamics change drastically if the photon energy of the probe beam is situated in-between the region $3.1728\text{eV} < E_t < 3.1697\text{eV}$. The tested pump-pulse polaritons have photon energies $3.1992\text{eV} < E_p < 3.2023\text{eV}$ (region B in Fig.4.5). In this region, the group velocity of the lower polaritons is so small that they do not reach the rear surface of the sample within 180ps and the spin memory is conserved over a long time. We call this region "spin-flip region". When comparing $\Delta T^{++}(t)/T$ and $\Delta T^{+-}(t)/T$, we nicely see how pump polaritons scatter from σ^+ to σ^- helicity and that their densities become equal at about 150ps. Then both densities decrease equally in time.

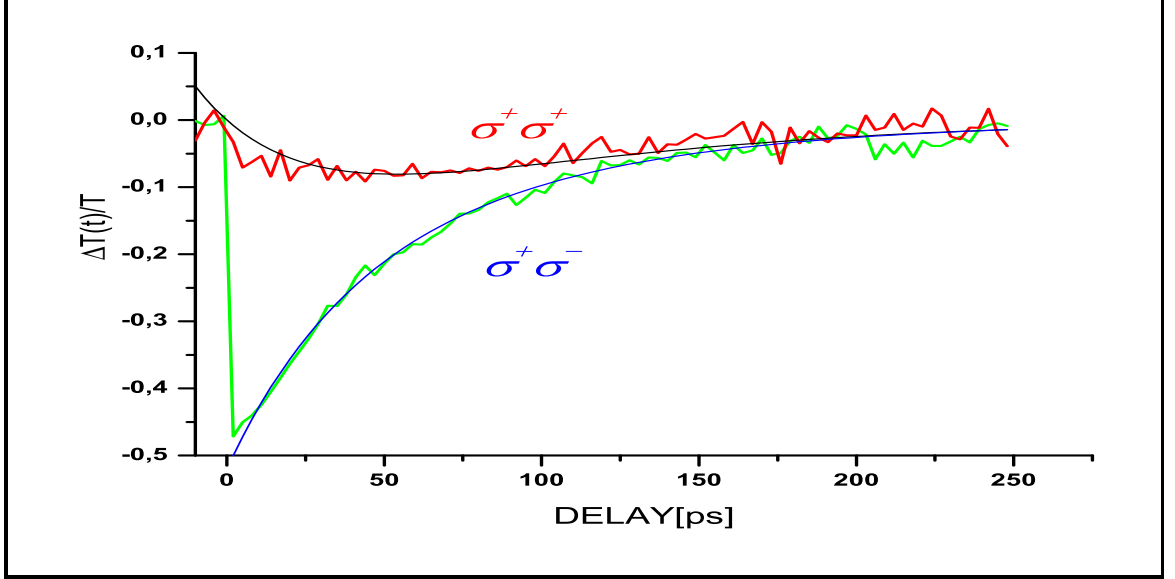


Figure 4.7: Induced transmission changes for the $\sigma^+\sigma^+$ configuration, for the $\sigma^+\sigma^-$ configuration, for $E_t = 3.1715\text{eV}$ (corresponding to $E_p = 3.2005\text{eV}$) together with the fit using Eq. 4.3(Region B).

4.3.1 Modeling of experimental results for region B (Spin-flip region)

Let us assume that polaritons can either undergo a spin-flip process characterized by the time constant τ_S or recombine or scatter (due to coupling with polaritons in the bottleneck region or biexcitons) to states with higher energies. In this case they are lost for the spin-flip process studied here. If τ_R is the characteristic time constant of these last processes, the corresponding rate equations are given by (60):

$$\frac{dN_{\pm}(t)}{dt} = -\frac{N_{\pm}(t)}{\tau_R} - \frac{N_{\pm}(t)}{\tau_S} + \frac{N_{\mp}(t)}{\tau_S} \quad (4.2)$$

where $N_+(t)$ and $N_-(t)$ denote the time dependent polariton populations with σ^+ and σ^- helicities, respectively. The solutions of the rate equations with the initial conditions $N_+(0) = N_0$ and $N_-(0) = 0$ are:

$$N_+(t) + N_-(t) = N_0 \exp(-t/\tau_R),$$

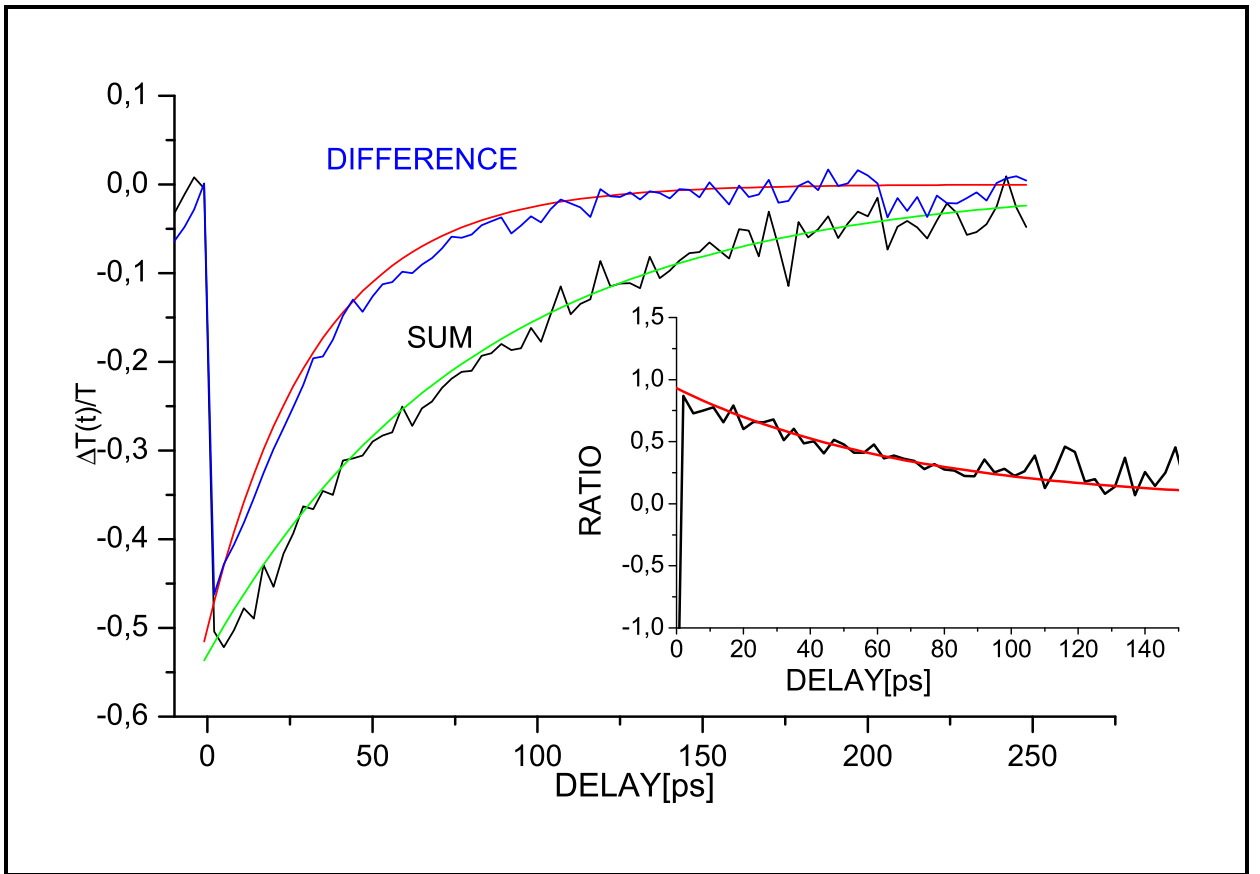


Figure 4.8: Sum and difference of induced transmission changes for the $\sigma^+\sigma^+$ configuration, for the $\sigma^+\sigma^-$ configuration, for $E_t = 3.1715\text{eV}$ (corresponding to $E_p = 3.2005\text{eV}$) together with the fit using Eq. 4.3. A ratio of sum/difference is shown in the inset (Region B).

4.3 Region B (Spin-flip region)

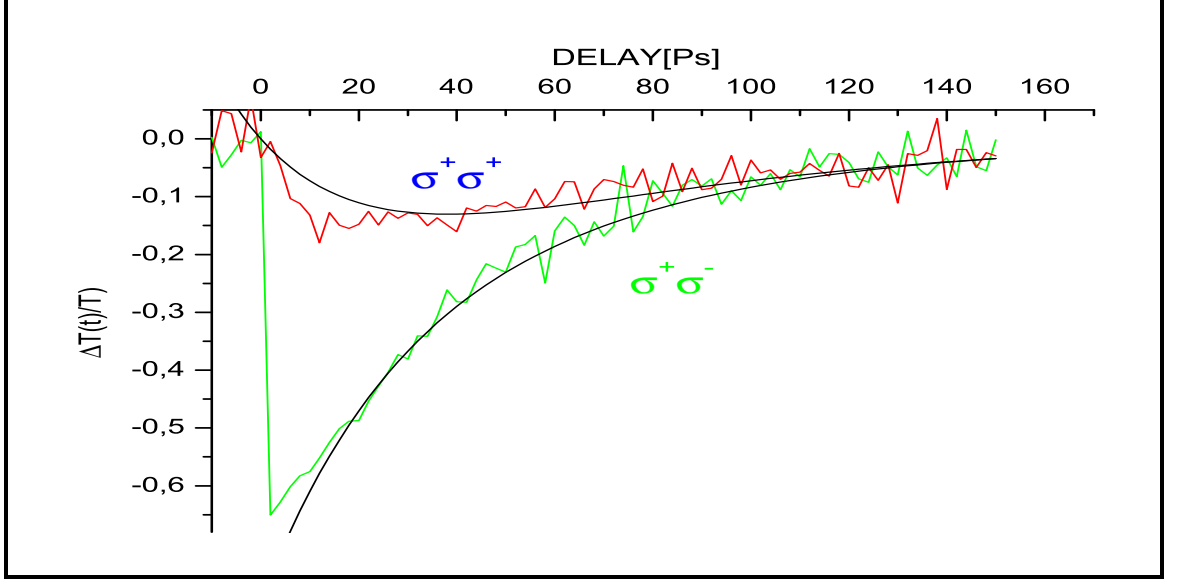


Figure 4.9: Induced transmission changes for the $\sigma^+\sigma^+$ configuration and for the $\sigma^+\sigma^-$ configuration for $T=40\text{K}$ and $E_t = 3.1777\text{eV}$ together with the fit using Eq. 4.3

$$N_+(t) - N_-(t) = N_0 \exp(-(1/\tau_R + 2/t_S)t). \quad (4.3)$$

In the case of linear absorption changes due to the pump pulses, the test beam transmission in the $\sigma^+\sigma^-$ configuration is given by:

$$T^{+-}(t) = \frac{I_T}{I_0} = \exp[-(\alpha_L + N_+(t) \cdot \sigma_p) \cdot d] \quad (4.4)$$

where I_0 is the intensity of the incident beam, α_L the linear absorption, and σ_p the induced absorption cross-section per polariton. Then,

$$\frac{\Delta T^{+-}(t)}{T} = \frac{I_{ind}(t)}{I_T} = (\exp[-(N_+(t) \cdot \sigma_p) \cdot d] - 1) \quad (4.5)$$

and similarly for $\Delta T^{++}(t)/T$ replacing $N_+(t)$ by $N_-(t)$. $I_{ind}(t)$ is the induced change of the transmitted intensity (see Eq. 3.7).

In Fig. 4.7 and Fig. 4.8 we show the fit of the induced transmission changes with expression 4.3, at 4K and with an excitation intensity of 0.5 mW/cm^2 .

4.4 III-C Region C-I (The polariton bottleneck region)

We obtain $\tau_S = 120 \pm 10\text{ps}$ and $\tau_e = 80 \pm 10\text{ps}$, respectively (60). These values remain valid if the excitation intensity remains lower than $1.5\text{mW}/\text{cm}^2$. At higher intensities, the dynamics is faster and a satisfactory fit of $\Delta T^{++}(t)$ and $\Delta T^{+-}(t)$ with our simple model is no longer possible.

As shown in Fig.4.9, when increasing the temperature up to 40K, τ_S remains unchanged but τ_R decreases to about 60ps (71). As mentioned above, the energy of the exciton resonance increases with temperature, implying a shift of the spin-flip region. This indicates that inelastic scattering with phonons, which is temperature dependent, becomes important.

4.4 III-C Region C-I (The polariton bottleneck region)

The spectral properties of the induced absorption changes once more drastically if the photon energy of the probe beam is situated below $E_t < 3.1694\text{eV}$ at 4K. In this case the pump-pulse polaritons have photon energies $E_p > 3.2026\text{eV}$, i. e. energies above that of the transverse exciton and inside the polariton bottleneck region (region C in Fig. 4.5). The polariton dispersion being almost flat in this region, one obtains a very high density of state, which causes a very important scattering rate between polaritons (71). For $E_t = 3.1673\text{eV}$ (corresponding to $E_p = 3.2047\text{eV}$) a temperature of 4K, and an excitation intensity of $0.5\text{mW}/\text{cm}^2$ Fig. 4.10 shows as an example that the absorption dynamics becomes faster when compared to region B and that the densities of polaritons with σ^+ and σ^- helicity become equal earlier, indicating that the spin memory is lost sooner.

4.4 III-C Region C-I (The polariton bottleneck region)

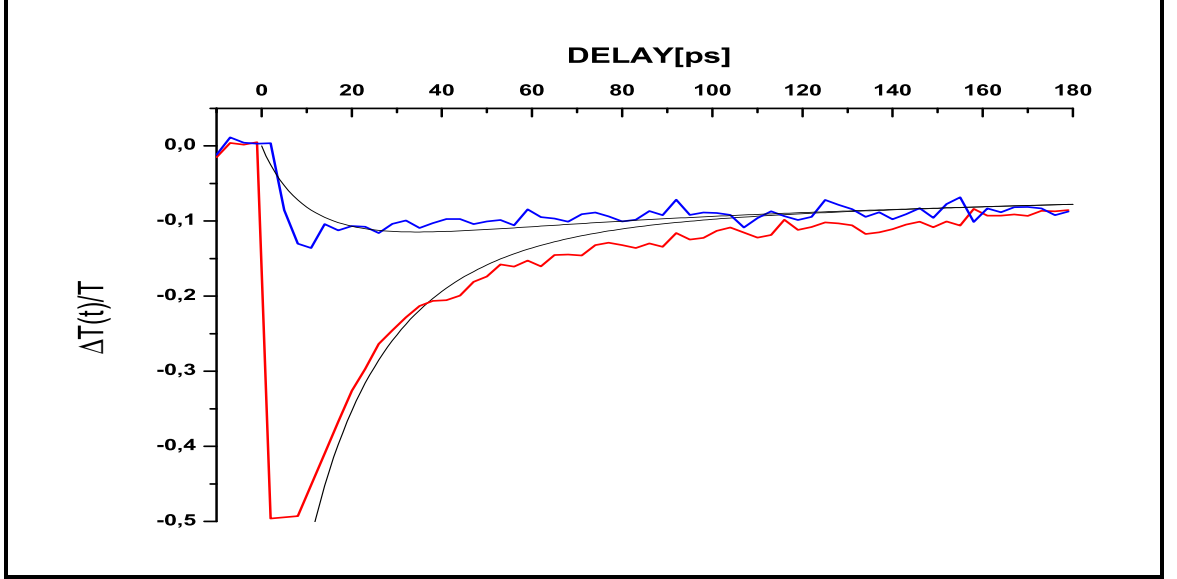


Figure 4.10: Induced transmission changes for the $\sigma^+\sigma^+$ configuration and for the $\sigma^+\sigma^-$ configuration for $T=4K$ and $E_t = 3.1673eV$ (corresponding to $E_p = 3.2047eV$) together with the fit using Eq. 4.6 (Region C-I).

4.4.1 Modeling of experimental results for region C-I (polariton bottleneck)

Because of the importance of scattering, the model established above is no longer valid in the bottleneck region. We extend it by including biexciton formation similar to (72; 73; 74). The corresponding rate equations are now given by:

$$\begin{aligned}
 \frac{dN_T^\pm(t)}{dt} &= +\frac{N_B(t)}{3\tau_B} - \frac{N_T^\pm(t)}{\tau_R} - \frac{N_T^\pm(t)}{\tau_S} + \frac{N_T^\mp(t)}{\tau_S} + \frac{N_L(t)}{2\tau_L} - B_{XX}N_T^\pm(N_T^+(t) + N_T^-(t) + N_L(t)) \\
 \frac{dN_L(t)}{dt} &= +\frac{N_B(t)}{3\tau_B} - \frac{N_L(t)}{\tau_R} - \frac{N_L(t)}{\tau_L} - B_{XX}N_L(N_T^+(t) + N_T^-(t) + N_L(t)) \\
 \frac{dN_B(t)}{dt} &= -\frac{N_B(t)}{\tau_B} + \frac{B_{XX}}{2}(N_T^+(t) + N_T^-(t) + N_L(t))^2
 \end{aligned} \tag{4.6}$$

As indicated in Fig. 4.5, B_{XX} , N_B and τ_B denote the biexciton formation probability through coupling of two excitons, their density, and lifetime, respectively. Biexcitons are created through binding of two excitons, which may be transverse (index + and -) or longitudinal (index L). It is important to notice

that in this relaxation channel (which is mainly achieved through emission of optical phonons followed by biexciton thermalization) the wave vector and the spin polarization of the initial excitons are not conserved. The biexcitons dissociate by emission of one photon in the spectral region of the induced absorption and by creation of a longitudinal or transverse exciton (75).

The transition probability to these states is assumed to be the same. In addition, we choose for the relaxation time of the longitudinal excitons to the transverse states (τ_L) the same value as for their lifetime, i. e. $\tau_L = \tau_R$. As shown in Fig.4.10 for $T = 4$ K and $E_t = 3.1673$ eV for a pump beam excitation intensity of 2.66 mW/cm², the induced absorption dynamics can be well explained by this model. We find for the spin-flip times $\tau_S = 70 \pm 10$ ps and transverse exciton lifetimes $\tau_R = 130 \pm 10$ ps. The parameters characterizing the biexcitons are : $B_{XX} = 1.5 \times 10^{-8}$ cm³/s and $\tau_B = 120 \pm 10$ ps. It is important to point out that a satisfactory fit of the induced transmission changes can not be obtained in the frame of the model described by Eq.4.3 (by reducing for example only the spin-flip time). One has to introduce the nonlinear term in order to explain the high values and the fast dynamics of $\Delta T^{++}(t)$ and $\Delta T^{+-}(t)$ which are measured independently. The success of the model indicates that the spin memory is lost through biexciton formation and an increase of the spin flip probability(71). The latter is due to the high density of states above the polariton bottleneck which favors exciton - exciton scattering processes.

4.5 Region C-II (Gain)

If the photon energy of the probe beam is situated below $E_t < 3.1640$ eV at 4K, the pump-pulse polaritons tested have photon energies $E_p > 3.2080$ eV, which correspond to energies above that of the longitudinal exciton and above the polariton

bottleneck region (region C-II in Fig. 4.5). Depending on the excitation intensity, at this and higher photon energies, the system can pass from induced absorption to gain due to induced recombination of biexcitons. Biexcitons formation is possible in CuCl by coupling of two excitons. They may emit a longitudinal optical phonon whose energy $\hbar\omega_{LO} = 26.0$ meV (13) is close to the biexciton binding energy ($E_b = 28$ meV). This process is very efficient because of its nearly resonant nature and because of the highly polar binding of CuCl, leading to a strong coupling between electrons and longitudinal optical phonon. Biexcitons are thus created at a wave vector $K \neq 0$ with an excess energy of several meV. They may further thermalize on their dispersion curve by emission of acoustical phonons. Their recombination to a longitudinal exciton and a polariton is stimulated by the probe beam with energy and momentum conservation. The longitudinal excitons rapidly thermalize to lower polaritons by emission of acoustical or optical phonons. This rapid thermalization assures that the population inversion between longitudinal excitons and biexcitons is maintained. Fig 4.11 shows an example for the rapid dynamics which is observed for $E_t = 3.1600$ eV, corresponding to tested polaritons at energies $E_p = 3.2112$ eV.

For photon energies $E_t < 3.1641$ eV the system can even pass from induced absorption (observed at low intensity of excitation) to stimulated emission for higher pump - pulse intensities. Since longitudinal excitons can thermalize efficiently to the lower polariton branch, the longitudinal exciton branch is unoccupied and a population inversion between biexcitons and longitudinal excitons is easily achieved. If we denote the density of photons at this frequency and polarization by N_A , we obtain the following set of rate equations (75):

$$\frac{dN_T^\pm(t)}{dt} = +\frac{N_B(t)}{3\tau_B} - \frac{N_T^\pm(t)}{\tau_R} - \frac{N_T^\pm(t)}{\tau_S} + \frac{N_T^\mp(t)}{2\tau_L} - B_{XX}N_T^\pm(N_T^+(t) + N_T^-(t) + N_L(t))$$

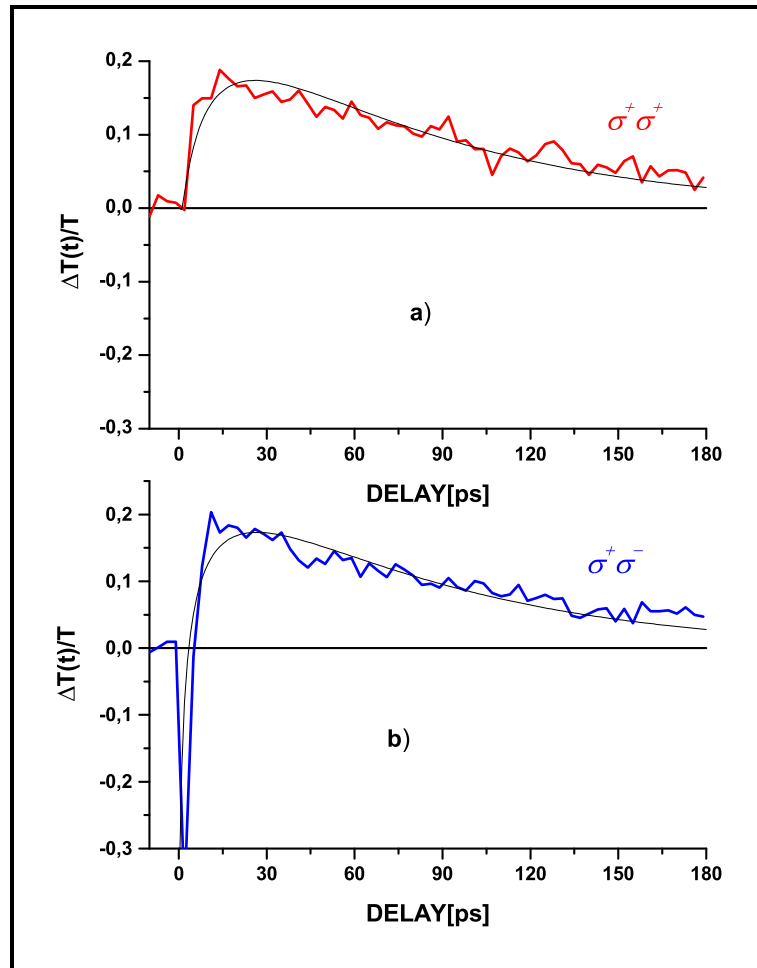


Figure 4.11: Induced transmission changes for the $\sigma^+\sigma^+$ configuration a) and for the $\sigma^+\sigma^-$ configuration b) for $T=4\text{K}$ and $E_t = 3.1600\text{eV}$ (corresponding to $E_p = 3.2112\text{ eV}$). together with the fit using Eq.4.7.

4.6 Absorption bleaching and phonon replica

$$\begin{aligned}
\frac{dN_L(t)}{dt} &= +\frac{N_B(t)}{3\tau_B} - \frac{N_L(t)}{\tau_R} - \frac{N_L(t)}{\tau_L} + \\
&\quad g(N_B(t) - N_L(t))N_A(t) - B_{XX}N_L(N_T^+(t) + N_T^-(t) + N_L(t)) \\
\frac{dN_B(t)}{dt} &= -\frac{N_B(t)}{\tau_B} + \frac{B_{XX}}{2}(N_T^+(t) + N_T^-(t) + N_L(t))^2 - g(N_B(t) - N_L(t))N_A(t) \\
\frac{dN_A(t)}{dt} &= +g(N_B(t) - N_L(t))N_A(t) - AN_A(t)
\end{aligned} \tag{4.7}$$

where g is the gain coefficient and A the probability that the polariton leaves the excited region (72; 76). Fig. 4.11 shows a typical result for gain in this spectral region at 4K and with an excitation intensity of $2.66 \text{ mW}/\text{cm}^2$. It is interesting to notice that the spin memory is lost immediately after the excitation. The probe beam is absorbed only if it coincides in time with the pump pulse. When the probe pulse is delayed, it is amplified. This only slightly signifies that stimulated emission builds up from noise immediately after the excitation. In order to simulate this behavior, we have to consider rate equations connecting excitons, biexcitons, and photons, which stimulate the recombination of biexcitons to one photon and a longitudinal exciton. A fit with the given set of equations is possible but not satisfactory since the nonlinear coefficient B_{XX} has to be highly increased when compared to result from Eq. 4.6. This indicates that a much more sophisticated description of the population dynamics is needed which is beyond the scope of this thesis.

4.6 Absorption bleaching and phonon replica

In this section, we discuss about the other positive and negative transmission changes. Let us start with the positive transmission changes around 3.186eV in Fig. 4.4 for the $\sigma^+\sigma^+$ configuration which is almost absent in Fig. 4.3. To our opinion it is due to a bleaching of the absorption induced by the wings of the pump pulse. As seen in the PL spectrum, the corresponding states are ob-

served in emission. A positive transmission change is also observed in the region of the M_L biexciton emission (3.161eV) (see page 95). They are similar in the $\sigma^+\sigma^-$ and the $\sigma^+\sigma^+$ configuration. We attributed it to a stimulated emission process, which is induced by the probe beam polaritons from biexcitons to longitudinal excitons. The latter thermalize rapidly to lower polaritons, giving rise to a population inversion between biexcitons and longitudinal excitons. The strong stimulated emission ends after about 100ps, time at which the lines labeled ν_2 (around 3.179eV) and at 3.186eV grow up. The line labeled ν_2 is attributed in literature to an exciton, bound to a neutral acceptor. It shows up in emission and absorption (77; 78). The energy difference between this line and the exciton polariton population around 3.205eV, which is created by the pump pulse through strong linear absorption as well as through biexciton decay corresponds to the energy of a longitudinal phonon. Therefore we believe that these states are populated by a phonon replica of the exciton like polaritons (75). The line around 3.186eV (at half the biexciton energy) has a similar origin: longitudinal excitons created by the recombination of biexcitons around 3.212eV emit an optical phonon and reabsorb a photon from the test beam to create again biexcitons. These channels of phonon emission is in competition with the biexciton creation by two exciton-like polariton or an exciton polariton and a longitudinal exciton. Therefore, the phonon emission channel becomes important at low exciton densities, i.e. after the end of the stimulated emission.

4.7 Conclusions

In this chapter we have determined the spin polarized polariton dynamics of CuCl through induced absorption to biexcitons in non-degenerate pump-probe experiments. We have evaluated how the optical properties close to the exciton

resonance develop in time from induced absorption to gain, depending on the wavelength and the intensity of excitation. We have shown that the spin-flip time and the relaxation dynamics of exciton polaritons can be determined by non-degenerate induced-absorption measurements. This is possible in the "spin-flip region" situated just below the polariton bottleneck where the studied polaritons are quite slow and propagate freely. Under these conditions, their density of states and their mutual scattering rates are low and surface effects, to which their dynamics is very sensitive, do not perturb them. Since the polariton wave vector is small in this region, spin relaxation due to symmetry breaking effects has little influence and the polariton spin-flip time is long (of the order of 100ps for temperatures below 40K and for low intensity). Exciton-exciton collision processes and surface effects do not significantly influence these long spin-flip times. When increasing the temperature, the time constant τ_L , describing losses of the population involved, decreases. This demonstrates the importance of inelastic scattering processes with phonons.

Below the spin-flip region, however, the spin memory is rapidly destroyed when the polaritons, having a high group velocity, reach the rear surface of the sample where they are scattered. Within the bottleneck region, the spin-flip time shortens significantly due to scattering processes which become important because of the high density of states and a larger polariton wave vector which increase the spin relaxation rate. In addition, the spin polarization memory of the quasiparticles is destroyed by coupling of two polaritons and the creation of biexcitons. They undergo energy relaxation processes and recombine radiatively, leaving behind a new polariton population which is no longer spin polarized. At even lower photon energies, stimulated emission may take place at high intensities of excitation. In this case, gain builds up from the noise and the spin memory of

4.7 Conclusions

the polaritons is immediately lost after the excitation through the pump pulse.

Chapter 5

Spin relaxation and symmetry breaking effects

5.1 The invariant expansion method of an effective Hamiltonian

I wish to present here the theoretical interpretation of spin relaxation in CuCl based on the invariant expansion method of an effective Hamiltonian (79). The method of invariants allows to construct the Hamiltonian $H(Q)$ of a system having a limited number of states in a matrix representation from symmetry arguments, without explicitly calculating the numerical values of the interaction terms. The invariant method is based on group theory (29; 80). The resulting Hamiltonian contains a set of unknown constants which are usually determined from experimental data.

Let us consider the one-particle band structure of semiconductors with T_d point-group symmetry which is shown in Fig. 2.2. It has a lowest conduction band with Γ_6 -symmetry at the center of Brillouin zone and two uppermost valence band with Γ_8 and Γ_7 -symmetry, respectively, split by spin-orbit interaction. The band with Γ_8 -symmetry is fourfold degenerate. We will now give a set of basis matrices, operating on states for electrons in conduction band, holes in valence

5.1 The invariant expansion method of an effective Hamiltonian

Table 5.1: Transformation properties of different quantities in crystals with T_d point-group symmetry. K^+ and K^- denote symmetry under time reversal, see text.

Transformation properties		
Hamiltonian	Γ_1	K^+
Wavevectors	Γ_5	K^-
Pauli's spin matrix	Γ_4	K^-
Unit matrix \mathbb{I}	Γ_1	K^+
Magnetic field \mathbf{B}	Γ_4	K^-
Electric field \mathbf{E}	Γ_5	K^+

band, and excitons.

Let us first consider as an example the case of a single additional electron in the conduction band in the presence of filled valence bands. We are interested in the Hamiltonian which describes the interaction of this electron with the crystal under internal perturbations. Since the Hamiltonian has the full point-group symmetry of the crystal, it has the same transformation properties as the basis function obeying to the irreducible representation Γ_1 .

In addition, the Hamiltonian is invariant under time reversal (K^+) since we consider systems which have no time-dependent potentials. We now construct an effective Hamiltonian for the interaction terms, which remain invariant under all symmetry operations of the point group of the crystal (Γ_1) and under time reversal (K^+). Working in the Schrödinger picture and restricting the discussion to the spin degenerate conduction band only, we define a subspace of dimensionality $n=2$, in which this effective electron Hamiltonian H_e is acting. This approximation implies that all perturbations do not appreciably mix valence or higher conduction band states into the conduction band under consideration. In

5.1 The invariant expansion method of an effective Hamiltonian

the matrix representation, H_e has the most general form:

$$H_e = \begin{pmatrix} a_{11} & a_{12} \\ a_{21} & a_{22} \end{pmatrix}. \quad (5.1)$$

Eigenstates of H_e are the pseudo-Bloch functions α_e and β_e , which have s-type angular symmetry and are spin $\frac{1}{2}$ up and down states, respectively. The matrix (a_{ij}) may be decomposed into n^2 linearly independent matrices, which are called "basis matrices" of the Hamiltonian H_e . Since the transformation properties of the angular momentum are well known for every crystal, we derive from it our basis matrices. We thus obtain:

$$\begin{pmatrix} a_{11} & a_{12} \\ a_{21} & a_{22} \end{pmatrix} = \frac{1}{2}[(a_{11}+a_{22})\mathbb{I}^e + (a_{12}+a_{21})\sigma_x^e + i(a_{12}-a_{21})\sigma_y^e + (a_{11}-a_{22})\sigma_z^e] \quad (5.2)$$

where \mathbb{I}^e is the two-dimensional unit matrix and $\sigma_x^e, \sigma_y^e, \sigma_z^e$ are the Pauli's spin matrices, acting on the states of conduction band (index e). Since \mathbb{I}^e is the unit matrix, interaction terms proportional to it remain invariant under all symmetry operations of point group and under time inversion. In our notation, \mathbb{I}^e transform as Γ_1 and K^+ . The components of the effective spin operator $\sigma^e = (\sigma_x^e, \sigma_y^e, \sigma_z^e)$ transform as Γ_4 in crystals with T_d point-group symmetry. Since angular momentum operators imply first derivatives with respect to time, they change their sign with time inversion. They have therefore K^- -symmetry in our notation. We learn from Eq. 5.2 that the matrices $\mathbb{I}^e, \sigma_x^e, \sigma_y^e$ and σ_z^e are a set of basis matrices. Concerning the split-off band with Γ_7 -symmetry at the center of the Brillouin zone, the degeneracy of the valence band is the same as that of the conduction band. The effective Hamiltonian of an isolated hole in this band has the same parametrized form as that of an electron in the conduction band. Only the numerical values of the parameters would be different, due to the different coupling

5.1 The invariant expansion method of an effective Hamiltonian

Table 5.2: Multiplication table for the group T_d

Γ_1	Γ_2	Γ_3	Γ_4	Γ_5	Γ_6	Γ_7	Γ_8	
Γ_1	Γ_1	Γ_2	Γ_3	Γ_4	Γ_5	Γ_6	Γ_7	Γ_8
Γ_2	Γ_1	Γ_3	Γ_5	Γ_4	Γ_7	Γ_6	Γ_8	
Γ_3	$\Gamma_1 \oplus \Gamma_2 \oplus \Gamma_3$	$\Gamma_4 \oplus \Gamma_5$	$\Gamma_4 \oplus \Gamma_5$	Γ_8	Γ_8	$\Gamma_6 \oplus \Gamma_7 \oplus \Gamma_8$		
Γ_4	$\Gamma_1 \oplus \Gamma_3 \oplus \Gamma_4 \oplus \Gamma_5$	$\Gamma_2 \oplus \Gamma_3 \oplus \Gamma_4 \oplus \Gamma_5$	$\Gamma_6 \oplus \Gamma_8$	$\Gamma_7 \oplus \Gamma_8$	$\Gamma_6 \oplus \Gamma_7 \oplus 2\Gamma_8$			
Γ_5	$\Gamma_1 \oplus \Gamma_3 \oplus \Gamma_4 \oplus \Gamma_5$	$\Gamma_7 \oplus \Gamma_8$	$\Gamma_6 \oplus \Gamma_8$	$\Gamma_6 \oplus \Gamma_7 \oplus 2\Gamma_8$				
Γ_6	$\Gamma_1 \oplus \Gamma_4$	$\Gamma_2 \oplus \Gamma_5$	$\Gamma_3 \oplus \Gamma_4 \oplus 2\Gamma_5$					
Γ_7	$\Gamma_1 \oplus \Gamma_4$	$\Gamma_3 \oplus \Gamma_4 \oplus 2\Gamma_5$						
Γ_8	$\Gamma_1 \oplus \Gamma_2 \oplus \Gamma_3 \oplus 2\Gamma_4 \oplus 2\Gamma_5$							

strengths. Therefore, we can consider the matrices \mathbb{I}^h , σ_x^h , σ_y^h and σ_z^h as a set of basis matrices for holes in the Γ_7 valence band.

If we consider the valence band with Γ_8 -symmetry, we have to use a higher order subspace for the holes. This can be achieved when replacing $\sigma^h = 1/2$ by $J^h = 3/2$.

In semiconductors, excitons are made up from an electron excited to the conduction band, interacting with all the remaining electrons in the valence bands. In the Hartree-Fock approximation, the exciton system may be reduced to a two-particle problem and an effective two-particle Hamiltonian may be defined.

In this approximation, the interaction between the electron in the conduction band and the electrons in the valence band is replaced by an interaction between the conduction band electron and one hole in the valence band. The hole state is given by the Kramers conjugated one-electron state. Neglecting all other bands, we consider only the lowest lying conduction band and the uppermost valence band in the following, which are both only twofold degenerate in CuCl. Then, in a matrix representation of the Hamiltonian, the exciton ground states are eigenvectors of a four by four matrix, which is obtained by the direct product of the two subspaces.

5.1 The invariant expansion method of an effective Hamiltonian

Table 5.3: Multiplication scheme for the different components of irreducible representations in crystals with T_d -symmetry.

Symmetry	Resulting component			Product of components		
$\Gamma_1: S$	$UU' + VV'$			$PP' + QQ' + RR'$		$XX' + YY' + ZZ'$
$\Gamma_2: T$	$UV' - VU'$			$PX' + QY' + RZ'$		
U	$UV' + VU'$			$\sqrt{3}PP' - QQ'$	$2RZ' - PX' - QY'$	$\sqrt{3}(XX' - YY')$
$\Gamma_3:$	$UV' - VU'$			$2RR' - PP' - QQ'$	$\sqrt{3}(QY' - PX')$	$2ZZ' - XX' - YY'$
P	$(\sqrt{3}U - V)P'$	$-(\sqrt{3}V + U)X'$	$QR' - RQ'$	$QZ' - RY'$	$YZ' - ZY'$	
$\Gamma_4: Q$	$-(\sqrt{3}U + V)P'$	$(\sqrt{3}V - U)Y'$	$RP' - PR'$	$RX' - PZ'$	$ZX' - YX'$	
R	$(\sqrt{3}U - V)P'$	$2UZ'$	$PQ' - QP'$	$PY' - QX'$	$XY' - YX'$	
X	$-(\sqrt{3}V + U)P'$	$\sqrt{3}U - V)X'$	$QR' + RQ'$	$QZ' - RY'$	$YZ' + ZY'$	
$\Gamma_5: Y$	$(\sqrt{3}V - U)QP'$	$-(\sqrt{3}U + V)Y'$	$RP' + PR'$	$RX' - PZ'$	$ZX' + XZ'$	
Z	$-2UR'$	$2VZ'$	$PQ' + QP'$	$PY' - QX'$	$XY' + YX'$	

The wavevectors of electrons or holes will be denoted in this chapter by $\vec{\mathbf{k}}$ and those of excitons by \mathbf{Q} . If we have any symmetry breaking effects, the hamiltonian depends on a set of physical quantities, which can be, for example, magnetic fields, electric fields, stress, and so on, as external perturbations. It also depends on the exciton center of mass wave vector \mathbf{Q} or products of it (noted \mathbf{Q}^n in the following) as internal perturbations. In this theie we consider the effect of internal perturbations on the exciton-spin relaxation. Therefore, the invariant terms, which have to be considered in the hamiltonian, are: $(\mathbb{I}^e, \sigma^e, \mathbf{Q}^n)$ for the conduction band, $(\mathbb{I}^h, \sigma^h, \mathbf{Q}^n)$ for the valence band, and for electron - hole exchange terms $(\sigma^e, \sigma^h, \mathbf{Q}^n)$. Table 5.1 lists the transformation properties of different quantities in crystals with T_d symmetry and Table 5.2 and Table 5.3 give the multiplication tables for two different components. These basis functions transform as the following irreducible representations:

$$\Gamma_1 : S,$$

$$\begin{aligned}
\Gamma_2 & : T, \\
\Gamma_3 & : U, V, \\
\Gamma_4 & : P, Q, R, \\
\Gamma_5 & : X, Y, Z.
\end{aligned} \tag{5.3}$$

5.2 Formulation of invariant expansion

In CuCl, as explained above, in a matrix representation of the hamiltonian, the exciton ground states are eigenvectors of a four by four matrix. Let us consider the effect of internal perturbations \mathbf{Q}^n for $n=0,1,2,\geq 3$. We obtain for the Hamiltonian of the exciton ground states at the Γ point in the absence of any symmetry breaking effects due to the wave vector ($n=0$):

$$H_0 = \Delta_0 \mathbb{I}^e \otimes \mathbb{I}^h + \Delta_1 \sigma^e \cdot \sigma^h, \tag{5.4}$$

The parameters Δ_0 and Δ_1 account for the exciton binding energy as well as for the different electron-hole exchange interactions. We consider these terms for the hamiltonian because both terms have (Γ_1, K^+) symmetry. From tables 5.1 and 5.2 we find that

$$\begin{aligned}
\mathbb{I}^e \otimes \mathbb{I}^h & = (\Gamma_1, K^+) \otimes (\Gamma_1, K^+) \\
& = (\Gamma_1, K^+)
\end{aligned} \tag{5.5}$$

$$\begin{aligned}
\sigma^e \cdot \sigma^h & = (\Gamma_4, K^-)_e \otimes (\Gamma_4, K^-)_h \\
& = (\Gamma_1, K^+) \in (\Gamma_1 \oplus \Gamma_3 \oplus \Gamma_4 \oplus \Gamma_5, K^+)
\end{aligned} \tag{5.6}$$

Using table 5.3 the term with Γ_1 symmetry is constructed and turns out to be $\sigma^e \cdot \sigma^h$. A term linear in \mathbf{Q} ($n=1$) is forbidden by symmetry i.e. there exist no

5.2 Formulation of invariant expansion

terms which vary linearly with the exciton wavevector \mathbf{Q} and transform as (Γ_1, K^+) :

$$\begin{aligned}\mathbf{Q}\sigma^e\sigma^h &= (\Gamma_5, K^-) \otimes (\Gamma_4, K^-)_e \otimes (\Gamma_4, K^-)_h \\ &= (\Gamma_1, K^+) \notin (\Gamma_5 \otimes \Gamma_4 \otimes \Gamma_4, K^-)_{e,h}\end{aligned}\quad (5.7)$$

$$\begin{aligned}\mathbf{Q}\mathbb{I}^e\mathbb{I}^h &= (\Gamma_5, K^-) \otimes (\Gamma_1, K^+)_e \otimes (\Gamma_1, K^+)_h \\ &= (\Gamma_1, K^+) \notin (\Gamma_5 \otimes \Gamma_1 \otimes \Gamma_1, K^-)_{e,h}\end{aligned}\quad (5.8)$$

$$\begin{aligned}\mathbf{Q}\sigma^e\mathbb{I}^h &= (\Gamma_5, K^-) \otimes (\Gamma_4, K^-)_e \otimes (\Gamma_1, K^+)_h \\ &= (\Gamma_1, K^+) \notin (\Gamma_5 \otimes \Gamma_4 \otimes \Gamma_1, K^-)_{e,h}\end{aligned}\quad (5.9)$$

and identically for $\mathbf{Q}\mathbb{I}^e\sigma^h$.

We can find dispersive terms quadratic in \mathbf{Q} ($n=2$). One has to consider the four possible constructions $\mathbf{Q}^2\sigma^e\mathbb{I}^h$, $\mathbf{Q}^2\mathbb{I}^e\sigma^h$, $\mathbf{Q}^2\mathbb{I}^e\mathbb{I}^h$ and $\mathbf{Q}^2\sigma^e\sigma^h$. In the first expression $\mathbf{Q}^2\sigma^e\mathbb{I}^h = (\Gamma_5, K^-) \otimes (\Gamma_5, K^-) \otimes (\Gamma_4, K^-)_e \otimes (\Gamma_1, K^+)_h$ the first two terms give the different possibilities to derive components from the wave vector transforming as $\Gamma_5 \otimes \Gamma_5 = \Gamma_1 \oplus \Gamma_3 \oplus \Gamma_4 \oplus \Gamma_5$. They have to be multiplied by the exciton matrix states transforming as $\Gamma_4 \oplus \Gamma_1 = \Gamma_4$. These quantities are determined using tables 5.2 and 5.3. We see that all such interaction terms which could be constructed vanish, because they have K^- symmetry under time reversal. Following this procedure, we find that the hamiltonian can contain four interaction terms quadratic in \mathbf{Q} :

$$H_{Q^2} = H_{\Gamma_1 \otimes \Gamma_1} + H_{\Gamma_3 \otimes \Gamma_3} + H_{\Gamma_4 \otimes \Gamma_4} + H_{\Gamma_5 \otimes \Gamma_5}, \quad (5.10)$$

has the required symmetry (Γ_1, K^+) properties. $H_{\Gamma_3 \otimes \Gamma_3}$ signifies that component quadratic in \mathbf{Q} and transforming like Γ_3 have to be multiplied with exciton

5.2 Formulation of invariant expansion

electron-hole states which have the same symmetry, than, we end up with the invariant representation in the electron-hole basis:

$$\begin{aligned}
H_{Q^2} &= G_1 \mathbf{Q}^2 \mathbb{I}^e \otimes \mathbb{I}^h + \delta_1 \mathbf{Q}^2 \sigma^e \cdot \sigma^h + \delta_2 [3(\sigma_x^e \sigma_x^h - \sigma_y^e \sigma_y^h)(Q_x^2 - Q_y^2) \\
&+ (2\sigma_z^e \sigma_z^h - \sigma_x^e \sigma_x^h - \sigma_y^e \sigma_y^h)(2Q_z^2 - Q_x^2 - Q_y^2)] \\
&+ \delta_3 [(\sigma_y^e \sigma_z^h + \sigma_z^e \sigma_y^h)(Q_y Q_z + Q_z Q_y) + c.p.] \quad (5.11)
\end{aligned}$$

G_1 , δ_1 , δ_2 and δ_3 are parameters describing completely the exciton dispersion. In matrix form we obtain (15):

	$ \alpha \rangle^e \alpha \rangle^h$	$ \alpha \rangle^e \beta \rangle^h$	$ \beta \rangle^e \alpha \rangle^h$	$ \beta \rangle^e \beta \rangle^h$
$ \alpha \rangle^e \alpha \rangle^h$	$A + B + D + F$	$-iE + F$	$-iE$	$C - iG$
$ \alpha \rangle^e \beta \rangle^h$	$iE + F$	$A - B - D - F$	$2B - D$	iE
$ \beta \rangle^e \alpha \rangle^h$	iE	$2B - D$	$A - B - D - F$	$iE - F$
$ \beta \rangle^e \beta \rangle^h$	$C + iG$	$-iE$	$-iE - F$	$A + B + D + F$

(5.12)

Where $A = G_1 \mathbf{Q}^2$, $B = \delta_1 \mathbf{Q}^2$, $C = 6\delta_2(Q_x^2 + Q_y^2)$, $D = 2\delta_2(2Q_z^2 - Q_x^2 - Q_y^2)$, $E = 2\delta_3(Q_y Q_z + Q_z Q_y)$, $F = 2\delta_3(Q_z Q_x + Q_x Q_z)$ and $G = 4\delta_3(Q_x Q_y + Q_y Q_x)$

The parameter G_1 is well known as the (isotropic) effective exciton mass given by the sum of the electron and the hole effective mass and δ_1 , δ_2 and δ_3 account for the wavevector dependence of exchange interaction. The total Hamiltonian then reads in the electron-hole basis:

$$\begin{aligned}
H &= H_0 + H_{Q^2} \\
&= \Delta_0 \mathbb{I}^e \otimes \mathbb{I}^h + \Delta_1 \sigma^e \cdot \sigma^h + H_{Q^2}, \quad (5.13)
\end{aligned}$$

If the total hamiltonian in Eq. 5.13 is transformed from the electron-hole representation to the exciton basis, using Eq. 2.2 and the wave functions tabulated in

5.2 Formulation of invariant expansion

(80). We then obtain :

$$\begin{aligned}
\phi_{ex}(x) &= \frac{-i}{\sqrt{2}}(|\beta^e > \phi_5^v + | \alpha^e > \phi_6^v) \\
\phi_{ex}(y) &= \frac{1}{\sqrt{2}}(|\beta^e > \phi_5^v - | \alpha^e > \phi_6^v) \\
\phi_{ex}(z) &= \frac{-i}{\sqrt{2}}(|\alpha^e > \phi_5^v + |\beta^e > \phi_6^v) \\
\phi_{ex}(\Gamma_2) &= \frac{1}{\sqrt{2}}(|\beta^e > \phi_6^v + | \alpha^e > \phi_5^v).
\end{aligned} \tag{5.14}$$

We then obtain the matrix representation for $H(\mathbf{Q})$:

$$\begin{array}{c}
\phi_{ex}(\Gamma_2) \quad \phi_{ex}(x) \quad \phi_{ex}(y) \quad \phi_{ex}(z) \\
\left(\begin{array}{cccc}
B(Q) & 0 & 0 & 0 \\
0 & A(Q) + \Delta_{LT}\alpha_1^2 & -4\delta_3 Q_x Q_y + \Delta_{LT}\alpha_1\alpha_2 & -4\delta_3 Q_x Q_z + \Delta_{LT}\alpha_1\alpha_2 \\
0 & \Delta_{LT}\alpha_1\alpha_2 - 4\delta_3 Q_y Q_z & A(Q) + \Delta_{LT}\alpha_1^2 & -4\delta_3 Q_y Q_z + \Delta_{LT}\alpha_1\alpha_2 \\
0 & \Delta_{LT}\alpha_1\alpha_2 - 4\delta_3 Q_x Q_z & \Delta_{LT}\alpha_1\alpha_2 - 4\delta_3 Q_y Q_z & A(Q) + \Delta_{LT}\alpha_1^2
\end{array} \right)
\end{array} \tag{5.15}$$

Where $B(Q) = \Delta_0 - 3\Delta_1 + Q^2(G_1 - 3\delta_1)$ and $A = \Delta_0 + \Delta_1 + (G_1 + \delta_1)Q^2 - 4\delta_2(2Q_z^2 - Q_x^2 - Q_y^2)$. α_1, α_2 and α_3 design the direction cosine of the wavevector \mathbf{Q} with respect to the cubic axes. Δ_{LT} is the splitting between the energies of the longitudinal and transverse exciton with Γ_5 -symmetry. It is due to the nonanalytic exchange interaction and, has only an influence on states in which the exciton dipole moments are oriented parallel to the direction of propagation given by \mathbf{Q} . Analytic and nonanalytic exchange interaction can only be separated in an exciton basis, in which the center-of-mass wavevector \mathbf{Q} of the exciton is finite. Then, the dipole moment can be decomposed into components parallel and perpendicular to \mathbf{Q} .

For the terms $n \geq 3$, we can consider terms involving $\mathbf{Q}^n \mathbb{I}^e \mathbb{I}^h$, $\mathbf{Q}^n \mathbb{I}^e \sigma^h$, $\mathbf{Q}^n \sigma^e \mathbb{I}^h$, and $\mathbf{Q}^n \sigma^e \sigma^h$. Concerning higher orders of the simultaneous spin-flip of electrons and holes proportional to products $\mathbf{Q}^n \sigma^e \sigma^h$, only **even** orders of n can contribute

5.2 Formulation of invariant expansion

because of the time reversed symmetry properties (K^+) of the Hamiltonian. For the term cubic in \mathbf{Q} , we obtain from tables 5.1 and 5.2

$$\begin{aligned}
\mathbf{Q}^3 \sigma^e \mathbb{I}^h &= (\Gamma_5, K^-) \otimes (\Gamma_5, K^-) \otimes (\Gamma_5, K^-) \otimes (\Gamma_4, K^-)_e \otimes (\Gamma_1, K^+)_h \\
&= (\Gamma_5 \otimes \Gamma_5 \otimes \Gamma_5 \otimes \Gamma_4 \otimes \Gamma_1, K^+) \\
\implies (\Gamma_1, K^+) &\in [(\Gamma_4 \otimes \Gamma_5) \otimes \Gamma_4, K^+] + (\Gamma_3 \otimes \Gamma_5) \otimes \Gamma_4, K^+ \\
&\quad + (\Gamma_5 \otimes \Gamma_5) \otimes \Gamma_4, K^+ \tag{5.16}
\end{aligned}$$

$$\begin{aligned}
\mathbf{Q}^3 \mathbb{I}^e \sigma^h &= (\Gamma_5, K^-) \otimes (\Gamma_5, K^-) \otimes (\Gamma_5, K^-) \otimes (\Gamma_1, K^+)_e \otimes (\Gamma_4, K^-)_h \\
&= (\Gamma_5 \otimes \Gamma_5 \otimes \Gamma_5 \otimes \Gamma_1 \otimes \Gamma_4, K^+) \\
\implies (\Gamma_1, K^+) &\in [(\Gamma_4 \otimes \Gamma_5) \otimes \Gamma_4, K^+] + (\Gamma_3 \otimes \Gamma_5) \otimes \Gamma_4, K^+ \\
&\quad + (\Gamma_5 \otimes \Gamma_5) \otimes \Gamma_4, K^+ \tag{5.17}
\end{aligned}$$

$$\begin{aligned}
\mathbf{Q}^3 \mathbb{I}^e \mathbb{I}^h &= (\Gamma_5, K^-) \otimes (\Gamma_5, K^-) \otimes (\Gamma_5, K^-) \otimes (\Gamma_1, K^+)_e \otimes (\Gamma_1, K^+)_h \\
\implies (\Gamma_1, K^+) &\notin (\Gamma_5 \otimes \Gamma_5 \otimes \Gamma_5 \otimes \Gamma_1 \otimes \Gamma_1, K^-) \tag{5.18}
\end{aligned}$$

From Eq.5.16 and 5.17, we can find only terms which involve matrix products of $\sigma^e \mathbb{I}^h$ or $\mathbb{I}^e \sigma^h$ giving the corresponding invariant terms of the Hamiltonian. For the term cubic in \mathbf{Q} we obtain a Hamiltonian

$$H_{Q^3} = A\{[(Q_y^2 - Q_z^2)Q_x]\sigma_x^e + c.p.\} \mathbb{I}^h + B\mathbb{I}^e\{[(Q_y^2 - Q_z^2)Q_x]\sigma_x^h + c.p.\} \tag{5.19}$$

where c. p. stands for cyclic permutation. We obtain (15) the matrix representation (complex conjugate terms of the upper (lower) part have to be added to

5.3 Exciton-spin relaxation in CuCl

the lower (upper) part):

$$\begin{array}{c}
 \phi_{ex}(\Gamma_2) \quad \phi_{ex}(x) \quad \phi_{ex}(y) \quad \phi_{ex}(z) \\
 \left(\begin{array}{cccc}
 A_z(Q)+\Delta_0-3\Delta_1 & -i(A_x(Q)+B_x(Q)) & -i(A_y(Q)-B_y(Q)) & -iB_z(Q) \\
 0 & A_z(Q)+\Delta_0+\Delta_1+\Delta_{LT}\alpha_1^2 & iB_z(Q) & i(A_y(Q)+B_y(Q)) \\
 0 & \Delta_{LT}\alpha_1\alpha_2 & A_z(Q)+\Delta_0+\Delta_1+\Delta_{LT}\alpha_2^2 & -i(A_x(Q)-B_x(Q)) \\
 0 & \Delta_{LT}\alpha_1\alpha_3 & \Delta_{LT}\alpha_1\alpha_2 & A_z(Q)+\Delta_0+\Delta_1+\Delta_{LT}\alpha_3^2
 \end{array} \right)
 \end{array} \quad (5.20)$$

Where $A_x(Q) = A[(Q_y^2 - Q_z^2)Q_x]$ and $B_x(Q) = B[(Q_y^2 - Q_z^2)Q_x]$.

Since polariton wave vectors involved in our experiments are small when compared to the Brillouin zone, we will limit our discussion of the simultaneous spin-flip of electrons and holes to the term in second order in \mathbf{Q} . On the other hand, the terms $\mathbf{Q}^n \mathbb{I}_e \sigma_h$ and $\mathbf{Q}^n \sigma_e \mathbb{I}_h$ can contribute to spin-flip of electrons or holes independently. These terms are efficient when we have a change in energy (transverse exciton to longitudinal excitons), associated with the spin flip but the simultaneous spin-flip of electrons and holes (term proportional to $\mathbf{Q}^n \sigma_e \sigma_h$), needs not to involve this change in energy (transverse exciton to transverse excitons).

5.3 Exciton-spin relaxation in CuCl

We can consider two possibilities for exciton-spin relaxation in CuCl (79): first due to scattering processes, in which the direction of \mathbf{Q} is changed and second due to the exchange interaction between electrons and holes in conjunction with the center-of-mass motion of the excitons. This interaction can mix different states. In our experiment, exciton polaritons are initially propagating in the [111] direction. The exciton states are then given by

$$X' = \frac{1}{\sqrt{2}}(\phi_{ex}(x) - \phi_{ex}(y))$$

5.3 Exciton-spin relaxation in CuCl

$$\begin{aligned}
 Y' &= \frac{1}{\sqrt{6}}(\phi_{ex}(x) + \phi_{ex}(y) - 2\phi_{ex}(z)) \\
 Z' &= \frac{1}{\sqrt{3}}(\phi_{ex}(x) + \phi_{ex}(y) + \phi_{ex}(z)).
 \end{aligned} \tag{5.21}$$

We neglect the excitons $\phi_{ex}(\Gamma_2)$ with Γ_2 symmetry, which are not coupled to the dipole active states and have no influence on our discussion. Using for this direction the given wave functions, the Hamiltonian from matrix 5.15 is diagonal and reduces to (79):

$$\begin{array}{c}
 X' \qquad Y' \qquad Z' \\
 \begin{pmatrix}
 X' & A(Q) + 4\delta_3 \frac{Q^2}{3} & 0 & 0 \\
 Y' & 0 & A(Q) + 4\delta_3 \frac{Q^2}{3} & 0 \\
 Z' & 0 & 0 & A(Q) - \frac{8}{3}\delta_3 \frac{Q^2}{3} + \Delta_{LT}
 \end{pmatrix}
 \end{array} \tag{5.22}$$

With $A(Q) = \Delta_0 + \Delta_{ST} + (G_1 + \delta_1)$. In matrix 5.22, Δ_{ST} denotes the analytical exchange interaction leading to singlet and triplet splitting and Δ_{LT} the non analytical exchange interaction giving rise to the longitudinal-transverse splitting. Since in this direction $Q_x = Q_y = Q_z$, $A(Q)$ is independent of δ_2 . Matrix 5.22 indicates that the propagating polariton modes are degenerate in energy. When using circularly polarized light, the wave functions of the photoexcited excitons are given by (79)

$$\begin{aligned}
 | +1 \rangle &= \frac{1}{\sqrt{2}}(X' + iY') \\
 | -1 \rangle &= \frac{1}{\sqrt{2}}(X' - iY') \\
 Z' &= Z'
 \end{aligned} \tag{5.23}$$

Using these wave functions, the Hamiltonian in the basis of $| +1 \rangle$ and $| -1 \rangle$ is diagonal and reduces to:

5.3 Exciton-spin relaxation in CuCl

$$\begin{array}{c}
 | +1 \rangle \\
 | +1 \rangle \\
 | -1 \rangle
 \end{array}
 \begin{array}{c}
 | +1 \rangle \\
 | -1 \rangle
 \end{array}
 \begin{pmatrix}
 A(Q) + 4\delta_3 \frac{Q^2}{3} & 0 \\
 0 & A(Q) + 4\delta_3 \frac{Q^2}{3}
 \end{pmatrix}
 \quad (5.24)$$

The states $| +1 \rangle$ and $| -1 \rangle$ are **not coupled** to each other. In other words, this hamiltonian can not be looked at due to as an effective magnetic field. The transverse exciton dispersion is also degenerate in the high symmetry [100] direction. But in all other directions, the circular polarization states $| +1 \rangle$ and $| -1 \rangle$ are **coupled**. Let us, as an example, consider the [110] direction. Here, the longitudinal and transverse modes are given by

$$\begin{aligned}
 \psi(L) &= \frac{1}{\sqrt{2}}(\phi_{ex}(x) + \phi_{ex}(y)) \\
 \psi(T_1) &= \phi_{ex}(z) \\
 \psi(T_2) &= \frac{1}{\sqrt{2}}(-\phi_{ex}(x) + \phi_{ex}(y))
 \end{aligned}
 \quad (5.25)$$

Using for this direction the given wave functions, the Hamiltonian is then

$$\begin{array}{c}
 \psi(L) \\
 \psi(T_2) \\
 \psi(T_1)
 \end{array}
 \begin{pmatrix}
 A(Q) - 4\delta_3 \frac{Q^2}{3} + \Delta_{LT} & 0 & 0 \\
 0 & A(Q) + 4\delta_3 \frac{Q^2}{3} & 0 \\
 0 & 0 & A(Q)
 \end{pmatrix}
 \quad (5.26)$$

Matrix 5.26 shows that the transverse eigenstates of the Hamiltonian with linear polarization, noted by (T_1) and (T_2) , are not degenerate in energy. This leads not only to birefringence but also to spin beating. When considering circularly polarized light we obtain the matrix representation of the hamiltonian of

5.3 Exciton-spin relaxation in CuCl

transverse exciton for the [110] direction given in Eq 5.27:

$$\begin{array}{cc}
 & | +1 \rangle & | -1 \rangle \\
 \begin{array}{l} | +1 \rangle \\ | -1 \rangle \end{array} & \left(\begin{array}{cc} A(Q) + \delta_3 Q^2 & -\delta_3 Q^2 \\ -\delta_3 Q^2 & A(Q) + \delta_3 Q^2 \end{array} \right) &
 \end{array} \quad (5.27)$$

The diagonal part contains the exchange interactions and all dispersion terms, which are isotropic. In addition, the states $| +1 \rangle$ and $| -1 \rangle$ are **coupled** to each other. Similar to the D'yakonov-Perel mechanisms (see page 139) or D'yakonov-Perel-Kachorovskii mechanisms (see page 149) , the symmetry breaking part of the dispersive terms in the hamiltonian may be looked at as being induced by an transverse effective magnetic field. This effective magnetic field determines the direction, around which the total angular momentum precesses, and the speed of precession. In the motional narrowing regime the system is subject to an effective, time-dependent, randomly oriented magnetic field (see section 2.10), which changes its direction with a characteristic time that is much shorter than the precession time.

Let us now consider scattering processes in which the propagation direction of the polaritons changes. Polaritons are longitudinal or transverse with respect to the direction of propagation and the projections of their polarization components onto the directions of propagation change in the scattering process (79). Therefore changes of the propagation direction lead immediately to partial spin relaxation for circularly polarized polaritons. In addition, such quasi-elastic scattering is possible for polariton states and the exciton spin-relaxation rate is directly related to the exciton wave vector relaxation time.

One sees in matrix 5.22 that the dispersions of longitudinal and transverse excitons in the [111] direction are characterized by different effective masses, which have been measured in Ref. (81). One finds for the longitudinal exciton

5.3 Exciton-spin relaxation in CuCl

$m_L = 3.14 m_0$ and for the transverse exciton $m_T = 2.3m_0$, m_0 being the electron mass. Using these values, we obtain for the wave vector dependent exchange term

$$\delta_3 = \frac{1}{4} \left(\frac{\hbar^2}{2m_0} \right) \left(\frac{1}{m_T} - \frac{1}{m_L} \right) \quad (5.28)$$

$\delta_3 = 1.1 \times 10^{-14} \text{meVcm}^2$ from which the coupling constant of the polariton states can be estimated. From the polariton dispersion relation we find for a photon energy of about 3.2 eV just below the bottleneck region, a wave vector $Q = 6 \times 10^5 \text{cm}^{-1}$. This gives rise to a coupling matrix element between the two circularly polarized states $2\delta_3 Q^2 = 0.008 \text{meV}$.

Let us assume that a polariton has scattered from the [111] direction to a wave vector pointing into a low symmetry [110] direction and has circular polarization. Now, in the new direction, the X and Y linear polarization components (chosen perpendicular to \mathbf{Q}) have a different phase relationship since their dispersion is not degenerate. The dephasing rate is proportional to δ_3 and Q^2 . After some time, the polariton is no longer circularly polarized. A successive scattering process will then lead to an spin relaxation. We can estimate from exciton diffusion measurements Ref. (74) the mean time τ_{col} between successive collisions to of the order of $\tau_{col} = 100 \text{ps}$. This values is not very precise since it depends on several physical parameters which are not very well known. This is for example the temperature of the exciton gas which is not necessarily equal to the lattice temperature. In addition, the diffusion constant depends, through the group velocity and in a complicated way, on the photon energy of the polaritons and of the excitation intensity. We find, however, that τ_{col} is comparable to the spin - relaxation time $\tau_s = 120 \text{ps}$ at 4 K determined in our work (see page 92). Although that the matrix element $2\delta_3 Q^2$ is very small, the condition $2\delta_3 Q^2 \tau_{col} \ll 1$ (characteristic for the motional narrowing region) is not fulfilled.

When averaging over the different propagation directions possible after a first

scattering out of the [111] direction, we can estimate the mean value of the coupling matrix element between the spin eigenstates to be about $\delta_3 Q^2$. We then find $\delta_3 Q^2 \tau_{col}$ to be of the order of unity. This indicates that τ_s is not equal to τ_{col} since we are not in the motional narrowing regime. On the contrary, both processes discussed above contribute to the observed spin relaxation. Inside the bottleneck region, the situation is not clearer since here the wave vector increases but the time between successive collisions decreases because of the possibility of exciton-exciton collisions.

5.4 Conclusions

We have discussed in this chapter a possible exciton-spin relaxation scenario applicable to CuCl. Exciton polaritons with circular polarization propagating in the [111] direction are first excited by pump pulse of about 170 femtosecond duration. In this direction, the circular polarization is obtained by a superposition of fields polarized linearly along the X and Y directions which are chosen perpendicular the direction of propagation. The dispersion of these modes is degenerated, i. e. they have a fixed phase relation and the circular polarization persists during the propagation of the polariton. The time evolution of the spin state is measured by induced absorption to biexcitons by a time delayed probe pulse, having also circular polarization and propagating in the [111] direction. In time resolved induced absorption experiments, as shown in Fig. 4.7, a strong signal first shows up in the $(\sigma^+ \sigma^-)$ configuration and later in the $(\sigma^+ \sigma^+)$ configuration, indicating that a spin-relaxation has occurred. In our situation, this is already achieved if the direction of propagation of the polaritons changes due to scattering processes. In addition, in other than the [111] and [100] directions, the polariton dispersion of the two transverse linear polarizations is no longer degenerate due

to a coupling of the circularly polarized spin states. The origin of this anisotropy is the wave vector dependent electron-hole exchange interaction δ_3 , which leads to a simultaneous spin - flip. It also shows up in a difference of the effective masses of longitudinal and transverse excitons, which has been determined by hyper-Raman scattering in the [111] direction in Ref (81). Therefore, in the [110] direction or in arbitrary low symmetry directions, the field components of the circularly polarized light dephase in time (79). We can estimate the mean value of the coupling matrix element from the experimental data to be about $\delta_3 Q^2$. Since $\delta_3 Q^2 \tau_{col}$ (where τ_{col} is the time between two successive collisions) is of the order of unity, this dephasing mechanism is important and leads to spin beating and also to an additional spin relaxation after collision processes. We therefore conclude that the spin relaxation time τ_s measured in our experiment is not equal to τ_{col} but that both time constants are of the same order of magnitude with $\tau_{col} > \tau_s$.

Chapter 6

Experimental Results : CdTe quantum wells

6.1 Introduction

Carrier-spin relaxations in semiconductors have been, since the early 70's, the subject of numerous studies. Very few experimental work treat, however, the spin relaxation of individual carriers (electrons and holes) in undoped materials (82; 83). Instead, spin relaxation is generally studied in luminescence experiments using doped semiconductors (50). Doping modifies however, the optical, electrical, and magnetic properties of the semiconductor. It is thus relevant to study spin relaxation of individual carriers in undoped materials. The application of a transverse magnetic field allows also to discriminate the spin dynamics of various quasi-particles in doped as well as undoped samples (68; 84; 85): the spin of the photoinjected carriers precesses around the magnetic field and the type of the involved carrier is deduced from the precession period. But the magnetic field modifies the way the spins relax, by, for example, perturbing internal magnetic fields. Therefore the measured spin relaxation times actually depend on the value of the applied magnetic field (85). To measure the spin relaxation of holes in undoped samples without magnetic field, Hilton et al. have performed

recently a non-degenerate pump-probe experiment in bulk GaAs (82) where the absorption between split-off valence bands is probed in the infrared after an inter-band excitation by near-visible pulses. In semiconductor quantum wells, several theoretical work predict a slowing-down of the spin relaxation of holes as compared to bulk material, as a result of the energy splitting of the light and heavy hole bands due to confinement (5; 86). But to our knowledge, in quantum wells, the spin relaxation time for holes has always been measured to be shorter than that for electrons. In GaAs quantum wells, Bar-Ad et al. studied the exciton spin relaxation at low temperature using a degenerate pump-probe experiment at the heavy-hole exciton resonance (62). They attempted to separate the contribution of electrons and holes from their differential transmission data. Tackeuchi et al. performed a comparable experiment but at room temperature (63). However, these relaxation dynamics are intrinsically dependent on both carrier spin relaxation times. The attribution of the fast and slow relaxation times to holes and electrons, respectively, is therefore not entirely satisfactory. Akimoto et al. performed a non-degenerate pump-probe experiment in CdTe/CdMnTe quantum wells in which they used the light-hole and heavy-hole exciton optical transitions to extract the electron- and hole-spin relaxation times (63). However the interpretation of the experiment is delicate.

We present here a simultaneous measurement of the electron and hole spin relaxation times in an undoped piezoelectric CdTe multiple quantum well structure at low temperature (10K) (87). The built-in piezoelectric field (26) inside the wells probably modifies the carrier spin dynamics as compared to non-piezoelectric wells, but also gives, through two different heavy-hole excitonic optical transitions, a simple and direct access to the spin relaxation times of both electrons and holes.

6.2 Excitonic optical nonlinearities in multiple quantum wells

There are many possible nonlinear optical effects in quantum wells. Here we will discuss only one class of effects, namely those related to optical absorption saturation near to the band-gap energy. The physics of excitonic-absorption saturation is intrinsically a many body problem, because it depends not only on the final-state interactions of electron and hole but also on the final-state interaction with all other particles in the semiconductor. Many body effects can be divided into two categories (88): the first one comes from the Pauli exclusion principle or bandfilling effect. The second process is the carrier screening of electron-hole Coulomb attraction. In our sample we must also consider that the nonlinearity arises from screening of strain-induced electric fields by the redistribution of photogenerated charges within the quantum wells. Excitons are formed by electrons in the conduction band and holes in the valence band. In other words they are built from a combination of single-particle states, and any change in character of single-particle states will indirectly affect the excitons. Thus Coulomb interaction and exclusion-principle effects described in a single-particle band picture (band-gap renormalization and bandfilling) induce also changes in the optical response of excitons. We will consider in the following these mechanisms and recall and review the main results. The detailed study of many body problems are beyond the scope of this thesis.

6.2.1 Optical nonlinearities due to screening

In our experiments we can consider two screening effects:

- a) Screening of the attractive electron-hole Coulomb interaction:

In this case, screening simply refers to the reduction of the range of the

6.2 Excitonic optical nonlinearities in multiple quantum wells

Coulomb potential of a charge in the presence of the other charges. The existence of an exciton resonance depends on the attractive Coulomb interaction between an electron and a hole. In bulk materials, specially in the presence of an e-h plasma, screening of the attractive electron-hole Coulomb interaction leads to one of the largest optical nonlinearities. The observed effect is excitation-dependent bleaching of the exciton resonance. In 2-d quantum wells Coulomb screening is weaker than in bulk. A significant part of the electric field line of Coulomb interaction in a quantum well are outside the layer in which the carriers can move, therefore the possibilities for the carriers to modify the Coulomb interaction are very restricted.

b) Screening of the strain-induced polarization field :

As dicussed in page 57, The static piezo electric field causes a Stark shift of the excitons in the strained layer and thus decreases the transition energies. With the screening of the static piezo electric field, a blueshift of the excitonic lines is expected. These effect have been already studied (39). In our samples, the strength of the screening of the piezoelectric filed is expected to be a larger effect than the screening of the attractive electron-hole Coulomb interaction between an electron and a hole.

6.2.2 Optical nonlinearities due to the bandfilling effect

The electrons and holes, as fermions, can occupy a quantum state only once, according to the Pauli exclusion principle. Hence each k state in a semiconductor band can be occupied twice, once with a spin-up and once with a spin-down carrier. An occupied state is no longer available as a final state in an optical absorption process. The carriers in quasi-equilibrium occupy the available states from the bottom of the band, so that the energetically lowest states are occupied

6.2 Excitonic optical nonlinearities in multiple quantum wells

first. This results in filling the states near the bottom of the conduction band by electrons and the top of the valence band by holes.

In order to be more quantitative, let us compute the commutation rule of the exciton operator. One finds, as a function of the number operators for electrons, $\hat{n}_e(k) = \hat{e}_k^\dagger \hat{e}_k$ and holes, $\hat{n}_h(k) = \hat{h}_{-k}^\dagger \hat{h}_{-k}$:

$$[\hat{X}_\alpha^\dagger, \hat{X}_\alpha] = \sum_k |\phi_\alpha(k)|^2 [1 - \hat{n}_e(k) - \hat{n}_h(k)] \quad (6.1)$$

Where \hat{e}_k^\dagger , \hat{h}_{-k}^\dagger and \hat{X}_α^\dagger are the creation operators of electrons, holes and excitons, respectively. $\phi_\alpha(k)$ is the Fourier transform of the exciton wave function. We see the effect of the Pauli principle. We need the expectation values of $\hat{n}_e(k)$ and $\hat{n}_h(k)$ in the exciton state $|X_\alpha\rangle = \hat{X}_\alpha^\dagger |\emptyset\rangle$. It is easy to show that

$$n_e^{(\alpha)}(k) = \langle X_\alpha | \hat{n}_e(k) | X_\alpha \rangle = n_h^{(\alpha)}(k) = \langle X_\alpha | \hat{n}_h(k) | X_\alpha \rangle = |\phi_\alpha(k)|^2 \quad (6.2)$$

so that

$$[1 - n_e^{(\alpha)}(k) - n_h^{(\alpha)}(k)] = [1 - 2 |\phi_\alpha(k)|^2]. \quad (6.3)$$

Hence, from the point of view of quantum statistics, creating one exciton is equivalent to create a very special distribution of electrons and holes: $|\phi_\alpha(k)|^2$. For N_α , we find an occupation $N_\alpha |\phi_\alpha(k)|^2$. This result implies that the generation of excitons prevents the subsequent generation of other excitons, a behavior of fermions and not of bosons. One can consider that excitons are nonideal "composite" bosons with underlying Fermi statistics reflecting that of their constituents. In other words, excitons feel each other not only through Coulomb interaction but also through Pauli exclusion between their electrons and holes (89). Creating an exciton uses some states of the pool of fermionic states of the crystal and produces Pauli blocking. This effect is called excitonic phase space filling.

6.3 Principle of the experiment

Let us consider optical nonlinearity due to the excitonic phase space filling and the bandfilling effect in detail. This effect shows up in valence-to-conduction-band ($v \rightarrow c$) transitions: the valence-band state is filled by an electron with a probability proportional to $(\propto 1 - n_h^{(\alpha)}(k))$ and the conduction-band state is empty $(\propto 1 - n_e^{(\alpha)}(k))$, so the transition rate is proportional to the product,

$$\mathfrak{T}_{v \rightarrow c} = (1 - n_h^{(\alpha)}(k))(1 - n_e^{(\alpha)}(k)). \quad (6.4)$$

Furthermore, to obtain the net transition rate, one has to subtract the inverse process (i.e., the conduction-to-valence-band transition rate ($c \rightarrow v$) that describe carrier recombination)

$$\mathfrak{T}_{c \rightarrow v} = n_e^{(\alpha)}(k)n_h^{(\alpha)}(k). \quad (6.5)$$

since it leads to a reduction of the bandfilling. Subtracting Eq. (6.4) from (6.5) yields the simultaneous availability of an electron and a hole state with a momentum k :

$$\mathfrak{T} = \mathfrak{T}_{v \rightarrow c} - \mathfrak{T}_{c \rightarrow v} = 1 - n_e^{(\alpha)}(k) - n_h^{(\alpha)}(k). \quad (6.6)$$

A change in transmission or a change in absorption can be written as

$$\frac{\Delta T}{T} \propto -\Delta\alpha \propto n_e^{(\alpha)}(k) + n_h^{(\alpha)}(k). \quad (6.7)$$

6.3 Principle of the experiment

The principle of the experiment is simple and relies on two optical transitions that share a common energy level. As discussed in Page 54, strained zinc blende semiconductor quantum wells grown along the [111] axis present an internal piezoelectric field inducing a separation of the electron and hole wave functions. Consequently, the optical transition between the second confined hole level HH_2 and

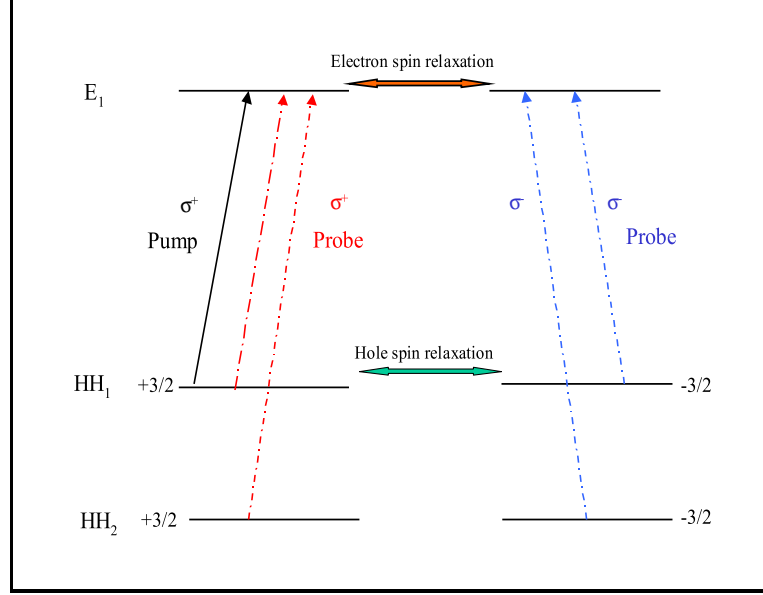


Figure 6.1: Scheme of the energy levels involved in the experiment and optical selection rules. The two lowest confined hole levels HH_1 and HH_2 of angular momentum $\pm 3/2$ and the first confined electron levels E_1 of spin $\pm 1/2$, are given. The arrows represent the optical transitions involved for the pump pulse (solid arrow, σ^+ circular polarization) or the probe pulse (dotted arrows, σ^+ and σ^- circular polarizations).

the first confined electron level E_1 , which is forbidden in symmetrical quantum wells, is made allowed by the strong built-in piezoelectric field (see Subsection 2.8.1).

We make use of this HH_2 - E_1 optical transition which shares the electron level with the HH_1 - E_1 transition (the first confined electron and hole levels) to measure directly, using a non-degenerate pump-probe experiment, the spin relaxation times of the electrons and holes in a non-degenerate pump-probe experiment (87). As an illustration, Fig.6.1 shows the level scheme excited in the pump-probe experiment in our sample. Change in transmission for $HH_1 \rightarrow E_1$ is

$$\left(\frac{\Delta T}{T}\right)_{E_1-HH_1} \propto (n_e^{(E_1)}(k) + n_h^{(HH_1)}(k)), \quad (6.8)$$

6.3 Principle of the experiment

and for transmission $HH_2 \rightarrow E_1$ is

$$\left(\frac{\Delta T}{T}\right)_{E_1-HH_2} \propto (n_e^{(E_1)}(k) + n_h^{(HH_2)}(k)). \quad (6.9)$$

If the pump pulse is resonant only with $HH_1 - E_1$ excitonic transitions, we have $n_h^{(HH_2)}(k) = 0$. The transitions involved in our experiment are excitonic transitions, but the Pauli blocking acts in the electron and hole sub-bands of both exciton components. The σ^+ circularly polarized pump pulse, resonant only with the $HH_1 - E_1$ excitonic transition, produces a population of holes and electrons in the corresponding spin states. The pump pulse produces about 10^{10} excitons/cm² per well. The ratio of the pump spectral intensities at the HH_1-E_1 and HH_2-E_1 transitions is greater than 100. The broadband linearly polarized probe pulse is resonant with both $HH_1 - E_1$ and $HH_2 - E_1$ excitonic transitions. Since the pump pulse does not produce a population of HH_2 holes and thermal excitation of HH_2 holes is not possible at 10 K, absorption saturation of the HH_2-E_1 transition reflects only the population of electrons at level E_1 . Then, the spin relaxation of electrons at level E_1 is obtained by measuring differential absorption signals for the two circular polarizations of the probe pulse and by extracting the absorption saturation component from these signals. The same measurement on the $HH_1 - E_1$ excitonic transition contains information on both, electron- and hole-spin relaxation.

Differential absorption spectra for the same and opposite circular polarizations of the probe pulse with respect to the pump circular polarization are shown in Fig. 6.2, for different time delays. A continuous signal, measured at negative delays, when the probe pulse precedes the pump pulse, is subtracted from the data. The main feature appearing for both transitions, is the absorption saturation due to the Pauli blocking of the states populated by the pump pulse. This effect appears as a positive integral of the differential absorption spectra over each transition.

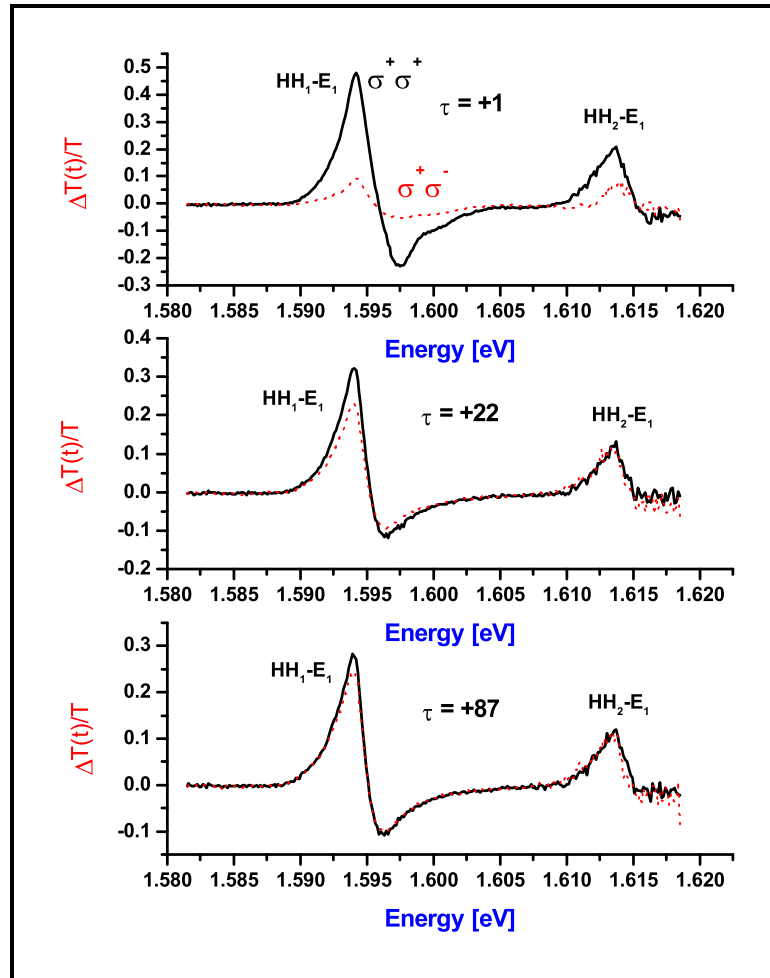


Figure 6.2: Differential transmission spectra for same (solid lines) and opposite (dotted lines) circular polarizations of the pump and probe pulses. (a) time-delay of 1ps after the excitation of the sample by the pump pulse, (b) time-delay of 22 ps after the excitation, (c) time-delay of 87 ps after the excitation. A continuous signal, measured at negative delays, is subtracted from the data.

6.3 Principle of the experiment

The second feature, clearly visible on the $HH_1 - E_1$ transition, is a blueshift of the resonance (see page 57). The screening of the static piezo electric field, by photogenerated carriers, is expected to shift it back toward the blue. This effect appears in the spectra as a signal proportional to the derivative of the absorption line.

In our piezoelectric quantum wells, the photo-excitation of an exciton population modifies the excitonic absorption lines in different ways. First, the phase space filling of the valence and conduction bands from which the excitons are built up, leads to a weakening of the oscillator strength. Next, the interaction between excitons manifests itself mainly in the line spectral position and width (88; 90). Last, the exciton-exciton interaction show up also as a screening of the static piezo-electric field which shifts the lines to the blue and increases the excitonic oscillator strength. The mentioned effects are spin-dependent: Shortly after the excitation, the phase space filling induced by the circularly polarized pump beam is observed only on the transmission of a co-polarized probe beam. Then, the relaxation of hole or electron spins gives rise to the population of dark exciton states. This leads also to an oscillator strength weakening of the bright excitons states, even if they are not populated, since they share a common electron or hole band with the dark exciton states. The Coulomb interaction between excitons is also spin-dependant: the excitation of excitons with anti-parallel momenta by contra-polarized beams can give rise to the formation of bound biexciton states. On the contrary, a larger repulsion is expected between excitons of parallel angular momenta, giving rise to a larger blue-shift of the excitonic line. The latter should be partially compensated by the screening of the Coulomb interaction which is less efficient for exciton with parallel spins (91). The screening of the static piezoelectric field is thus also spin-dependent.

6.3 Principle of the experiment

In our results, the spectral shift shown on the $E_1 - HH_1$ exciton transition depends strongly on the relative polarization of the pump and probe beams: at early time-delays, just after the excitation of the sample by the pump pulse (Fig. 6.2.a), the differential transmission signal is strong for the same circular polarization of the probe with respect to the pump, and weak for the opposite probe polarization. At a delay of 22 ps after the excitation of the sample (Fig. 6.2.b), the differential transmission signals have relaxed to the same value for the two polarization components at the $HH_2 - E_1$ transition, which is not the case at the $HH_1 - E_1$ transition. Since the transmission at the $HH_2 - E_1$ transition depends only on the population of electrons at level E_1 , we deduce that the populations of electrons for the two spin states are equilibrated i.e. the electron spin has completely relaxed. At a delay of 87ps (Fig. 6.2.c), the differential transmission signal becomes almost the same for the two polarization components at the $HH_1 - E_1$ transition, too, indicating that now the holes have also relaxed their angular momenta.

In Ref. (83), biexcitonic effects clearly show up in the differential transmission spectra but are not taken into account by the authors. In our sample, we observe a different behavior: biexcitonic effects do not show up and, in addition, the $HH_1 - E_1$ signal starts from zero for opposite circular polarization of the pump and probe pulses, clearly indicating the rise of the population of electrons of spin $\frac{1}{2}$ and at the same time the decrease of the population of electrons of spin $\frac{-1}{2}$.

Our data allow to go one step further and be more quantitative about the spin relaxation times of both carriers (87). A spectral integration of the differential transmission over each transition line (Fig. 6.3) allows us to average out the spectral shift and the broadening of the excitonic transitions, which are due to the screening of the piezoelectric field and to Coulomb interaction. Both processes

6.3 Principle of the experiment

can be supposed to modify only slightly the oscillator strength of the excitonic transitions and we will analyze our results in terms of phase space filling of the electron and hole bands from which the excitons are made up. In order to model these results, we assume that the population dynamics is determined by the exciton recombination τ_R and by the electron τ_e and hole spin flips τ_h (including the transfer to and from ± 2 dark states). We suppose that the exciton spin flip is strongly reduced in our piezo-electric QWs because the spatial separation of electrons and holes reduces the electron-hole exchange interaction (5; 44), as shown for a variable electric field in reference (43) (see Subsection 2.8.1). Since no $E_1 - HH_2$ exciton population is created by the pump beam, only the rate equations for $E_1 - HH_1$ excitons has to be considered. Moreover, the low temperature of the sample prevents the thermal excitation of the $E_1 - HH_2$ excitons from $E_1 - HH_1$ excitons. From $(e \pm 1/2, h \pm 3/2)$ electron and hole spins one can build $E_1 - HH_1$ excitons with four different spin states: ± 1 , which are dipole-active, and ± 2 . Excitons with ± 2 spin, as well as those with ± 1 spin but with a wavevector larger than the photon wavevector, are dark states.

The corresponding rate equations are given by:

$$\begin{aligned}
 \frac{dN_{+1}(t)}{dt} &= -\frac{N_{+1}(t)}{\tau_R} - \frac{N_{+1}(t)}{\tau_h^-} - \frac{N_{+1}(t)}{\tau_e^-} + \frac{N_{+2}(t)}{\tau_e^+} + \frac{N_{-2}(t)}{\tau_h^+} \\
 \frac{dN_{-1}(t)}{dt} &= -\frac{N_{-1}(t)}{\tau_R} - \frac{N_{-1}(t)}{\tau_h^-} - \frac{N_{-1}(t)}{\tau_e^-} + \frac{N_{-2}(t)}{\tau_e^+} + \frac{N_{+2}(t)}{\tau_h^+} \\
 \frac{dN_{+2}(t)}{dt} &= -\frac{N_{+2}(t)}{\tau_h^+} - \frac{N_{+2}(t)}{\tau_e^+} + \frac{N_{+1}(t)}{\tau_e^-} + \frac{N_{-1}(t)}{\tau_h^-} \\
 \frac{dN_{-2}(t)}{dt} &= -\frac{N_{-2}(t)}{\tau_h^+} - \frac{N_{-2}(t)}{\tau_e^+} + \frac{N_{-1}(t)}{\tau_e^-} + \frac{N_{+1}(t)}{\tau_h^-}
 \end{aligned} \tag{6.10}$$

with

$$\begin{aligned}
 \tau_e^\pm &= \tau_e(1 + e^{\pm \frac{\Delta}{kT}}) \\
 \tau_h^\pm &= \tau_h(1 + e^{\pm \frac{\Delta}{kT}})
 \end{aligned} \tag{6.11}$$

6.3 Principle of the experiment

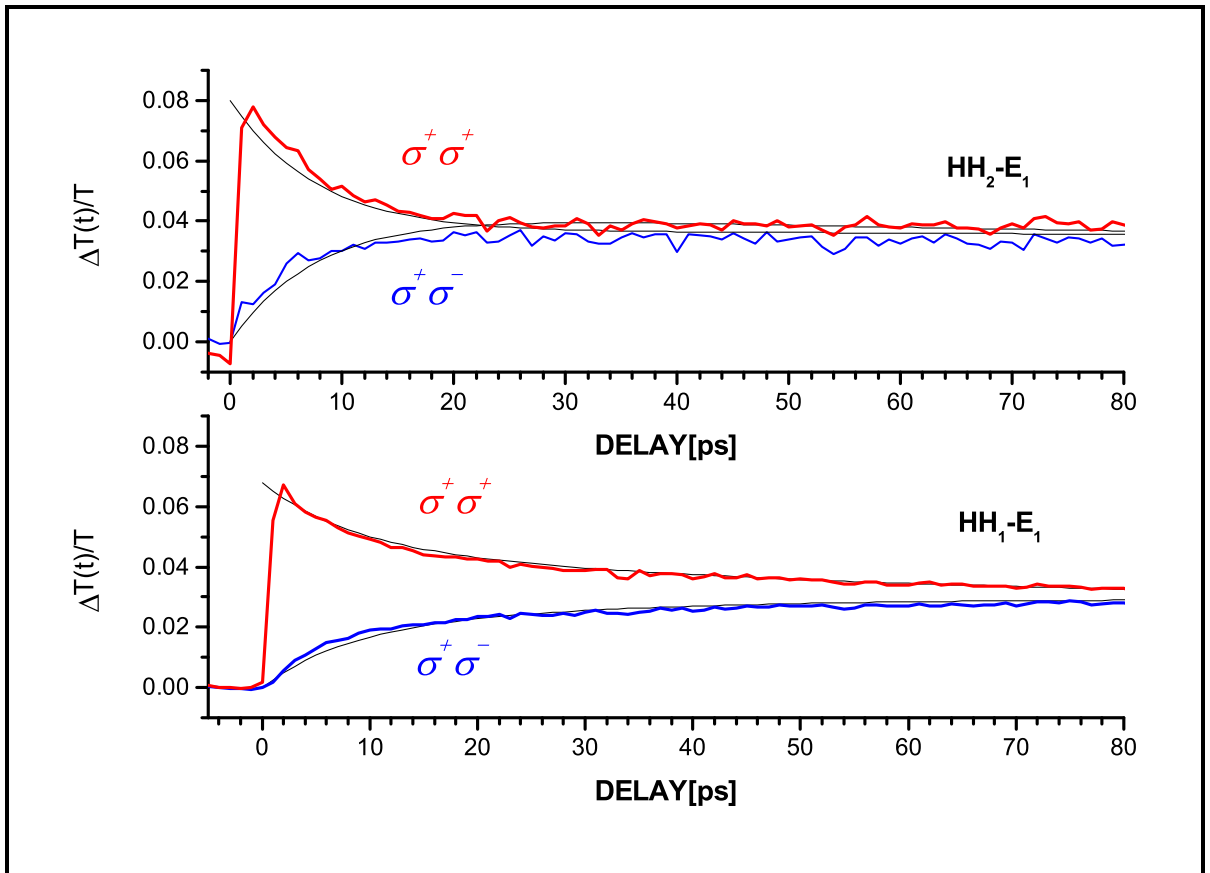


Figure 6.3: Differential transmission signal after spectral integration of the $HH_1 - E_1$ and $HH_2 - E_1$ transitions as a function of the pump-probe time-delay. Fits of data are shown as thin lines.

6.3 Principle of the experiment

Where $\Delta=0.15$ meV is the energy of the optically active states above the dark states (68). The differential transmission signal, which originates from the electron- and hole-state filling, has to be determined from the electron and hole occupation numbers, (f_e, f_h) which, in turn, depend on the $E_1 - HH_1$ exciton populations $N_{\pm 1}$ and $N_{\pm 2}$. Contrarily to photo-luminescence experiments, dark-state excitons contribute to the signal because their electrons and holes fill the states involved in the transitions which are probed. Considering a σ^+ pump, the differential transmission for $HH_1 - E_1$ transitions is then given by (87):

$$\left(\frac{\Delta T}{T}\right)_{E_1-HH_1}(\sigma^+\sigma^\pm) \propto (f_{E_1}(\mp\frac{1}{2}) + f_{HH_1}(\pm\frac{3}{2})) \propto (2n(\pm 1) + n(-2) + n(+2)). \quad (6.12)$$

And for $HH_2 - E_1$ transitions, it is given by:

$$\left(\frac{\Delta T}{T}\right)_{E_1-HH_2}(\sigma^+\sigma^\pm) \propto f_{E_1}(\mp\frac{1}{2}) \propto (n(\pm 1) + n(\mp 2)). \quad (6.13)$$

When fitting the experimental results (shown on Fig. 6.3), we determine an exciton recombination time τ_R of 400 ps, an electron spin relaxation time τ_e of 8 ps, and a heavy-hole relaxation time τ_h of 40 ps. In contrast with previous experimental studies in undoped quantum wells (62; 63; 83), we find that holes relax their spin more slowly than electrons. This could be explained first by the strain and the confinement in a piezoelectric quantum well acting on the light and heavy hole bands by lifting their degeneracy (see Section 2.7). These effects quench the main hole spin-flip mechanism (86). Secondly, as previously mentioned (see page 65), if the electron wave functions penetrate into the barrier, the s-d exchange scattering rate is important and we can consider this s-d exchange scattering as a source for electron spin relaxation which is reduced from 30ps in symmetrical quantum wells (83) down to 8 ps in our piezoelectrical quantum wells. As a result of the strong splitting between HH and LH bands, p-d exchange scattering rate is

negligible (92).

In other words, heavy hole-spin relaxation is less influenced by the interaction with the Mn spins (83).

6.4 Conclusions

We have presented experimental studies of spin relaxation in an undoped piezoelectric CdTe multiple quantum well structure at low temperature by using a non-degenerate pump-probe experiment. We have exploited the presence of two heavy-hole excitonic transitions in a piezoelectric undoped CdTe quantum well sample to determine the spin relaxation times of the photoexcited heavy-holes and electrons in the first confined energy level of the quantum wells.

After a spectral integration of the differential transmission over each transition line, we can average out the spectral shift and the broadening of the excitonic transitions. As a result, we can analyze our results in terms of phase space filling of the electron and hole bands from which the excitons are made up. The considered model and sample allows us to find a simultaneous measurement of the electron and hole spin relaxation times in an undoped sample and without application of a transverse magnetic field. We demonstrate experimentally that in our undoped piezoelectric quantum well, the heavy-holes relax their spin ($\tau_h = 40$ ps) more slowly than the electrons ($\tau_e = 8$ ps).

Chapter 7

Conclusions

In this thesis, we have determined the spin relaxation dynamics of excitons from induced absorption measurements. This is possible if transitions from degenerate states to other states are mutually allowed and forbidden for circularly polarized light with different helicities. We have applied this technique to two types of semiconductors: bulk CuCl and CdTe /CdMnTe quantum wells.

In CuCl our study gives us an insight into the role, which different scattering and dephasing mechanisms play. We discuss the importance of scattering with crystal defects and surfaces, with acoustical and optical phonons and with other excitonic polaritons which lead to spin relaxation. In addition, we have shown that the wavevector dependent exchange interaction leads to spin beating which implies that spin relaxation times become different from collision times in bulk semiconductors. The importance of these different effects depends largely on the photon energy via the density of the polariton states and their group velocity :

We have studied the dynamics of a system consisting of exciton polaritons in CuCl (which are the propagating, dipole active modes in the sample), and biexcitons in bulk semiconductors. The polariton dispersion curve is scanned in a pump and probe experiment by looking at different excitation and detection wavelengths. We have performed these studies at low temperatures on monocrys-

talline samples on a subpicosecond time scale. We have evaluated how the optical properties close to the exciton resonance develop in time from induced absorption to gain, depending on the wavelength and the intensity of excitation.

Biexcitons may be excited from the crystal ground state by two circularly polarized polaritons. This absorption process can be performed either simultaneously as in a two-photon absorption or in a two-step process where first a population of polaritons of a well defined helicity and energy is created. It is then probed by absorption of polaritons from a second pulse which induce the transition to the biexciton state obeying to energy and momentum conservation. Our measurements have been concentrated on this second process.

The induced transmission changes measure the probability that polaritons, created by the pump pulse at a given photon energy with σ^+ helicity undergo a transition to biexcitons by absorption of a polariton from the probe pulse. For collinearly propagating polaritons, due to the selection rules, this is only possible if the probe pulse has σ^- helicity. If, however, polaritons from the pump pulse perform a spin flip to σ^- helicity, their transition to the biexciton state can be induced with polaritons from a probe pulse with σ^+ helicity. Spin-flip processes are influenced by propagation effects, biexciton formation, collision processes with crystal imperfections and surfaces, mutual polariton-polariton scattering processes and scattering with acoustical or optical phonons. These scattering processes have a different importance in different spectral regions since the density of states and the group velocity are strongly dependent and the photon energy.

We have studied the time evolution of the total angular momentum (or pseudo spin) of polaritons in the "spin-flip region" situated just below the polariton bottleneck where the polaritons are quite slow and propagate freely. In this spectral region, the same number of spin flip processes occurs, if the polaritons

have run through the same distance in the sample, independent of their photon energy and their time of flight. It remains constant at higher temperatures, where only the loss rate of polaritons increases. This indicates that mainly collisions with crystal defects are responsible for the spin flip.

Besides electron-electron or hole-hole exchange between colliding particles, spin relaxation can be due to collision processes in which the polariton wave vector changes its direction. Since the transverse dipole moment is defined with respect to the direction of the wave vector, the spin-polarisation is partly lost.

Below the spin-flip region, however, the spin memory of the polaritons is rapidly destroyed when the polaritons, having a high group velocity, reach the rear surface of the sample where they are either transmitted through the surface or backscattered. In our samples the backscattered polaritons have completely lost their spin-memory. Within the bottleneck region, the spin-flip time shortens significantly due to different scattering processes which become important because of the high density of states which favours exciton-exciton scattering. In addition, the spin polarization memory of the quasiparticles is destroyed by coupling of two polaritons and the creation of biexcitons. They undergo energy relaxation processes and recombine radiatively, leaving behind a new polariton population which is no longer spin polarized.

At lower photon energies, stimulated emission takes place. In this case, gain builds up from the noise and the spin memory of the polaritons is immediately lost after the excitation through the pump pulse.

In addition, in other directions than the [111] and [100], the polariton dispersion of the two transverse linear polarizations is no longer degenerate, giving rise to a coupling of the circularly polarized spin states. The origin of this anisotropy is the wave vector dependent electron-hole exchange interaction δ_3 , which is known

experimentally. Therefore, in the [110] direction or an arbitrary low symmetry directions, the field components of the circularly polarized light dephase in time leading to spin beating.

In CdTe /CdMnTe quantum wells, we have studied the dynamics of spin relaxation at low temperature by using a non-degenerate pump-probe experiment. The principle of the experiment relies on two optical transitions that share a common energy level. We demonstrate experimentally that in our undoped piezoelectric quantum well, the heavy-holes relax their spin ($\tau_h = 40$ ps) more slowly than the electrons ($\tau_e = 8$ ps).

We have explained our results in terms of phase space filling of the electron and hole bands from which the excitons are made up. The considered model for the piezoelectric sample allows us to measure simultaneously the electron and hole spin relaxation times. In brief, we have shown that non degenerate pump and probe experiments allow to follow the spin-memory of exciton polaritons. Our technique is very promising for the study of other systems which obey to the same type of selection rules for two exciton transitions.

As an outlook, a detailed study of spin beating in CuCl would be interesting. This is possible, for example, when studying directly the induced absorption properties of the electromagnetic fields for polaritons propagating in the [110] direction. In this case it should be possible to separate the contributions of the spin flip due to the beating of the electromagnetic field and of the change in wave vector due to scattering. Such an experiment would lead to further insight into the role of intrinsic and extrinsic processes leading to spin relaxation.

For CdTe quantum wells, as we have seen that the physics of excitonic-absorption saturation is intrinsically a many body problem. With such studies we not only learn about spin relaxation dynamics, but also this study can help

for better understanding of spin dependent exciton saturation and spin dependent carrier screening of the Coulomb interaction and screening of strain-induced electric fields. Very recently, Kato *et al.* (93), observed spin splitting arising from strain in semiconductor films. The observed effect provides a flexible approach permitting electrical control of electron spins using strain engineering. In our sample, because of screening, we can change the internal electric field optically without application of an external electric field. A study of this effect in strained piezoelectric quantum wells would be interesting.

Appendix A

D'yakonov-Perel mechanisms

Quite generally, as a result of time-reversal symmetry, the energy eigenvalues of electronic states have to fulfill

$$E(k, \uparrow) = E(-k, \downarrow) \qquad E(k, \downarrow) = E(-k, \uparrow) \qquad (\text{A.1})$$

where k is the electron wave vector and \uparrow, \downarrow denote the spin states. In crystals like germanium or silicon (group-IV semiconductors), which additionally have space-inversion symmetry, ($E(k, \uparrow) = E(-k, \uparrow)$) must hold and therefore with Eq. (A.1) ($E(k, \uparrow) = E(k, \downarrow)$); i.e., all states are at least doubly degenerate (94; 95). However, in the zinc-blende structure, which does not have this inversion symmetry, a spin splitting of the energy bands arises. The classical works of Dresselhaus (96), Parameter (97) and Kane (98) discuss how this splitting due to spin-orbit interaction occurs.

An effective mechanism of spin relaxation of electrons associated with the spin-orbit splitting of the conduction band is the D'yakonov-Perel mechanism (51). The zero-field spin splitting of electron energy levels at wave vector k in the conduction band, which can be described by $H_{eff}(k)$ and added to the isotropic

effective-mass Hamiltonian, can be written as :

$$H_{eff}(k) = \frac{\hbar}{2} \vec{\Omega}_{eff}(k) \cdot \vec{\sigma} \quad (\text{A.2})$$

and

$$\vec{\Omega}_{eff}(k) = \frac{\alpha \hbar^2}{m \sqrt{2mE_g}} \vec{\chi} \quad (\text{A.3})$$

Where

$$\chi_x = k_x(k_x^2 - k_z^2) \quad \chi_y = k_y(k_y^2 - k_x^2) \quad \chi_z = k_y(k_y^2 - k_x^2) \quad (\text{A.4})$$

α is a numerical coefficient governing the spin splitting of the conduction band, m is the effective electron mass, k is the electron wave vector, E_g is the energy separation between the lowest lying conduction band and the uppermost valence band at the Γ point. This spin splitting, induced by lack of inversion symmetry, can be considered as an intrinsic k -dependent magnetic field $\vec{B}_i(k)$ around which electron spins precess with a Larmor frequency $\vec{\Omega}_{eff}(k) = (e/m) \vec{B}_i(k)$. Of course, because the crystal is cubic, in general the magnitude of the fluctuating field along each of the three cubic axes are equivalent, thus $T_1 \simeq T_2$. We can write Eq.(A.2) in matrix form:

$$H_{eff}(k) = \begin{pmatrix} k_z^2(k_x^2 - k_y^2) & k_x^2(k_y^2 - k_z^2) - i[k_y^2(k_z^2 - k_x^2)] \\ k_x^2(k_y^2 - k_z^2) + i[k_y^2(k_z^2 - k_x^2)] & -k_z^2(k_x^2 - k_y^2) \end{pmatrix}, \quad (\text{A.5})$$

after diagonalization, we can find the eigenvalues or the zero-field spin splitting of electron energy levels in the conduction band (96)

$$\Delta E_c = \pm [k^2(k_x^2 k_y^2 + k_y^2 k_z^2 + k_z^2 k_x^2) - 9k_x^2 k_y^2 k_z^2]^{\frac{1}{2}}. \quad (\text{A.6})$$

The average steady-state spin polarization along the i direction \overline{S}_i is found by solving the corresponding Boltzmann equation and averaging over all possible

directions of k ,

$$\overline{S_i} = \langle S_i \rangle_k. \quad (\text{A.7})$$

This procedure is simplified by assuming :

- 1) The momentum scattering time is much shorter than the spin life time.
- 2) The electron scattering is elastic, the electron energy spectrum is isotropic and the scattering cross section depends only on the scattering angle.

Under these conditions the H_{eff} (Eq.(A.3)) can be treated as a small perturbation.

After some algebraic manipulations, one finds (see (47) page 88)

$$\left[\frac{\partial \overline{S_i}}{\partial t} \right]_{DP} = -4 \frac{\tau_p}{\gamma_3} [\overline{S_i}(\overline{\Omega_j^2} + \overline{\Omega_k^2}) - \overline{S_j}(\overline{\Omega_j \Omega_i}) - \overline{S_k}(\overline{\Omega_k \Omega_i})]. \quad (\text{A.8})$$

$$\left[\frac{\partial \overline{S_i}}{\partial t} \right]_{DP} = -\frac{\overline{S_i}}{\tau_{s,ii}} + \frac{\overline{S_j}}{\tau_{s,ij}} + \frac{\overline{S_k}}{\tau_{s,ik}} \quad (\text{A.9})$$

The first term in Eq. (A.9) describes the relaxation of the mean spin $\overline{S_i}$ along the i direction, the other two the spin scattering from the j, k to the i direction. These terms can be estimated to be small compared the first one. γ_3 is a geometrical factor which depends on the scattering mechanism. From Eqs. (A.9) and (A.8) one finds, for the spin relaxation time τ_s

$$\frac{1}{\tau_s(\varepsilon)} = \frac{8}{3} \frac{\tau_p}{\gamma_3} (\overline{\Omega_x^2} + \overline{\Omega_y^2} + \overline{\Omega_z^2}) = \frac{8}{3} \frac{\tau_p}{\gamma_3} \overline{\Omega^2} \quad (\text{A.10})$$

Equation (A.10) can be decomposed into two factors. the factor $\tau_p(\frac{2}{3}\Omega^2)^{1/2}$ can be interpreted as the "precession angle" between two momentum-changing collisions (τ_p). For large $\tau_p(\frac{2}{3}\Omega^2)^{1/2}$ the spin component perpendicular to k is lost within the time τ_p . If $\tau_p(\frac{2}{3}\Omega^2)^{1/2}$ is small, however, Eq. (A.10), that which implies motional narrowing, applies. After averaging ¹ over the Maxwell distribution, the spin

¹When the spin relaxation time depends explicitly on the momentum relaxation τ_p , the average is not so simple because of the variation of τ_p as a function of energy ε is not well known.

relaxation rate is given by (47; 51)

$$\frac{1}{\tau_s(T)} = Q\alpha^2 \frac{(k_b T)^3}{\hbar^2 E_g} \tau_p \quad (\text{A.11})$$

Where Q is a dimensionless factor and ranges from 0.8 to 2.7 depending on the dominant momentum relaxation process. E_g is the band gap and α is the parameter characterizing the k^3 term for conduction band electron, and is approximately given by

$$\alpha \simeq \frac{4\eta}{\sqrt{3-\eta}} \frac{m_c}{m_o} \quad \eta = \frac{\Delta}{(E_g + \Delta)} \quad (\text{A.12})$$

Where Δ is the spin-orbit splitting of the valence band. It turns out that the DP spin relaxation time increases with decreasing scattering time τ_p . This indicates that the spin precession can not follow the fluctuating magnetic field, which changes its direction after each scattering process.

Appendix B

Elliott-Yafet mechanisms

Due to the spin-orbit interaction, the Bloch functions are generally not pure spin states. They should be more properly labeled as "pseudospin" eigenstates. This pseudospin nature emerges due to the inability to disentangle the spin component of the wavefunction from the orbital component; the wavefunction does not *factorize* into the product of a pure spin component and pure orbital component. The lack of factorization in the wavefunction constructing a spin eigenstates along an arbitrary direction from a linear combination of the two degenerate states (1). As a result the spin quantum state of the electrons is not preserved if elastic scattering occurs, even via **spin-independent scattering** such as scattering from potential fluctuations. This fact has been pointed out by Elliott(52; 53) for the electron scattering by the Coulomb potential of ionized impurities and by Yafet for the scattering by phonons(54).

In general an eigenstate at momentum \mathbf{K} and spin \uparrow has a nonzero amplitude of scattering via spin-independent processes into one of the two eigenstates $(\mathbf{K}', \downarrow)$ (spin-flip transition) and (\mathbf{K}'', \uparrow) (non-spin-flip transition). Several authors have analyzed the spin relaxation due to the Elliott-Yafet mechanisms. Chazalviel (99)

and Boguslawski (100) studied this mechanisms mediated by electron-impurity and electron-electron scattering, respectively. If spintronic devices are ever to work routinely at room temperature, polar-optical phonon scattering are likely to be the dominant source of spin relaxation. With this motivation Dyson and Ridley (101) have examined the Elliott-Yafet mechanisms involving polar-optical phonon scattering. The spin-flip and non-spin-flip transition probabilities are related to the matrix elements (50; 102)

$$|M_{\vec{K}_{\uparrow\downarrow}, \vec{K}'_{\uparrow\downarrow}}|^2 = |\langle \psi_{\vec{K}'_{\uparrow\downarrow}} | U(\vec{r}) | \psi_{\vec{K}_{\uparrow\downarrow}} \rangle|^2, \quad (\text{B.1})$$

where $U(\vec{r})$ is the perturbing potential and $\psi_{\vec{K}_{\uparrow\downarrow}}$ are the Bloch functions which are generally nonpure spin states. Spin relaxation $\frac{1}{\tau_s(\epsilon)}$ is given by:

$$\frac{1}{\tau_s(\epsilon)} = \frac{2\pi}{\hbar} \rho(\epsilon) \int \frac{d\Omega_{\vec{K}}}{4\pi} \int \frac{d\Omega_{\vec{K}'}}{4\pi} (|M_{\vec{K}_{\uparrow}, \vec{K}'_{\downarrow}}|^2 + |M_{\vec{K}_{\downarrow}, \vec{K}'_{\uparrow}}|^2) \quad (\text{B.2})$$

While momentum relaxation time is given by:

$$\frac{1}{\tau_p(\epsilon)} = \frac{2\pi}{\hbar} \rho(\epsilon) \int \frac{d\Omega_{\vec{K}}}{4\pi} \int \frac{d\Omega_{\vec{K}'}}{4\pi} (|M_{\vec{K}_{\uparrow}, \vec{K}'_{\uparrow}}|^2 + |M_{\vec{K}_{\downarrow}, \vec{K}'_{\downarrow}}|^2) (1 - \cos\theta') \quad (\text{B.3})$$

Where $\rho(\epsilon)$ is the density of states at energy $\epsilon = \hbar^2 k^2 / 2m^*$ and θ' is the angle between \vec{K} and \vec{K}' . For the usual scattering processes where $\epsilon \ll E_G$

$$|M_{\vec{K}_{\uparrow}, \vec{K}'_{\downarrow}}|^2 \ll |M_{\vec{K}_{\uparrow}, \vec{K}'_{\uparrow}}|^2 \quad (\text{B.4})$$

The ratio $\tau_p(\epsilon)/\tau_s(\epsilon)$ is readily evaluated when the potential $U(r)$ varies slowly on the scale of a unit cell since the Fourier transform of the potential can be factorized in the matrix elements. After averaging over the Maxwell distribution of electrons, the general expression for the rate of spin relaxation due to the Elliott-Yafet mechanism can be written in the form:

$$\frac{1}{\tau_s} = A \left(\frac{k_b T}{E_g} \right)^2 \eta^2 \left(\frac{1 - \eta/2}{1 - \eta/3} \right)^2 \frac{1}{\tau_p} \quad (\text{B.5})$$

Where E_g is the band gap, $\eta = \Delta/(E_g + \Delta)$, where Δ is the spin orbit splitting of the valence band. A is a dimensionless constant and varies from 2 to 6 depending on the dominant scattering mechanism for momentum relaxation.

The most important difference between the Elliott-Yafet mechanisms and D'yakonov-Perel (or D'yakonov-Perel-Kachorovskii mechanisms) is dependence on τ_p . While increased scattering intensity makes the Elliott-Yafet mechanisms more effective, it decreases the effectiveness of the D'yakonov-Perel processes. In the Elliott-Yafet process the precession frequency is conserved between collision and loss of phase occurs only in the short time during collision. The more collisions there are, the greater is loss of phase memory. On the other hand, in D'yakonov-Perel spin dephasing, spin phases are randomized between collisions, since electrons precess with different frequencies depending on their momenta. Spin-independent collisions with impurities or phonons do not lead to phase randomization (or spin relaxation) during the collision itself, but help to establish the random-walk-like evolution of the phase, leading to motional narrowing. These two mechanisms coexist in systems lacking inversion symmetry.

Appendix C

Bir-Aronov-Pikus mechanism

Electron scattering on holes can lead to spin-flip transitions due exchange interaction. Naturally, the Elliott-Yafet process also can cause spin-flip transitions in this case. For electron-hole scattering the Elliott-Yafet mechanism is much less efficient than the Bir-Aronov-Pikus mechanism caused by exchange interaction (55). Exchange interaction may also dominate in the case of electron scattering on paramagnetic impurities.

The Bir-Aronov-Pikus mechanism spin-flip mechanism (55), in p-doped samples, is due to the scattering of the electrons by the depolarized-spin hole population via these exchange terms. The spin-flip scattering probability depends on the state of the holes: degenerate or nondegenerate, bound on acceptors or free, fast or slow. The electron spin-flip rate $1/\tau_s$ is obtained by considering an electron with a momentum K and spin $+1/2(\uparrow)$ being scattered to a conduction state with spin $-1/2(\downarrow)$, such that

$$\begin{aligned} \frac{1}{2\tau_s(K)} &= \frac{2\pi}{\hbar} \sum_{P,P';k'} \sum_{M,M'} \sum_{s,s'} f_{p,M_s} (1 - f_{p',M's'}) \\ &\times |\langle \psi_{k'}^\downarrow \varphi_{p',M'}^{s'} | V_{exch} | \psi_k^\uparrow \varphi_{p,M}^s \rangle|^2 \end{aligned}$$

$$\times \delta(E_{K\uparrow}^e + E_{P,Ms}^M - E_{K'\downarrow}^e - E_{P',M's'}^M) \quad (\text{C.1})$$

Where E_P^M (E_K^e) is the energy of the hole (electron) with momentum P (K), and M and M' are the possible hole *mixed-spin* state. The Fermi distribution function of the degenerate hole is written as $f_{p,Ms}$. In A_3B_5 compounds, as a rule, $m_e \ll m_h$, so that the transferred momentum $\hbar(P - K)$ and electron momentum $\hbar K$ are much smaller than that of a hole $\hbar P$. As a result, the momentum of an electron-hole pair, $\hbar K$, is practically equal to $\hbar P$, and V_{exch} depends only on the direction of P.

τ_s is given by several different expressions depending on the given external parameters. In the case of a nondegenerate semiconductor $N_A < N_c$ (47; 103)

$$\frac{1}{\tau_s(\epsilon)} = \frac{2a_B^3}{\tau_o \nu_B} \left(\frac{2\epsilon}{m_c}\right)^{1/2} [n_{a,f} |\psi(0)|^4 + \frac{5}{3} n_{a,b}] \quad (\text{C.2})$$

Where $n_{a,f}$ ($n_{a,b}$) is the concentration of free (bound) holes and N_c is the critical hole concentration at which a nondegenerate hole gas becomes degenerate. ϵ is the conduction electron energy, and τ_o is given by the relation

$$\frac{1}{\tau_o} = \frac{3\pi}{64} \frac{\Delta_{exch}^2}{E_B \hbar} \quad (\text{C.3})$$

Where Δ_{exch} is the exchange splitting of the ground state. a_B , ν_B and E_B are defined as

$$a_B = \frac{\hbar^2 \epsilon_o}{e^2 m_R} = \frac{m_o}{m_R} \epsilon_o a_o \quad \nu_B = \frac{\hbar}{m_R a_B} \quad \frac{\hbar^2}{2m_R a_B^2} = \left(\frac{m_R}{m_o}\right) \frac{R}{\epsilon_o^2} \quad (\text{C.4})$$

Where m_R is the reduced mass of electron and hole, a_o the Bohr radius ($\simeq 0.53A$), and R the Rydberg constant ($\simeq 13.6eV$). $\psi(r)$ represents the wavefunction describing the relative motion of electron and hole and $|\psi(0)|^2$ is the Sommerfeld factor given by

$$|\psi(0)|^2 = \frac{2\pi}{\kappa} (1 - e^{-2\pi/\kappa})^{-1}, \quad \kappa = \sqrt{\frac{\epsilon}{E_B}}. \quad (\text{C.5})$$

For the degenerate case ($N_A > N_c$), the result is

$$\frac{1}{\tau_s(\epsilon)} = \frac{2a_B^3}{\tau_o \nu_B} \left(\frac{\epsilon}{\epsilon_f}\right) N_a |\psi(0)|^4 \times A \quad (\text{C.6})$$

A is given by the relation

$$\left(\frac{2\epsilon}{m_c}\right)^{1/2} \quad \text{if} \quad \epsilon_f < \epsilon \frac{m_\nu}{m_c} \quad (\text{C.7})$$

$$\left(\frac{2\epsilon_f}{m_\nu}\right)^{1/2} \quad \text{if} \quad \epsilon_f > \epsilon \frac{m_\nu}{m_c} \quad (\text{C.8})$$

Where m_ν is the hole effective mass and ϵ_f the hole Fermi energy, $(\hbar^2/2m_h)(3\pi^2 N_A)^{2/3}$.

To calculate τ_s , we first need to identify the adequate regime for a given parameter set. N_c is determined by the Mott criterion $N_c \approx (0.26/a_h)^3$ where $a_H = a_o \epsilon_o / (m_\nu / m_o)$. The thermal averaged value of $1/\tau_s$ is obtained as

$$\left\langle \frac{1}{\tau_s} \right\rangle = \frac{2}{\sqrt{2}(k_B T)^{3/2}} \int_0^\infty \frac{1}{\tau_s(\epsilon)} \sqrt{\epsilon} e^{-\epsilon/k_B T} d\epsilon \quad (\text{C.9})$$

assuming a classical Boltzmann distribution for conduction electron.

Appendix D

Spin relaxation mechanisms in quantum wells

D.1 Symmetric quantum well

Quantum phenomena in semiconductors are highly sensitive to details of the carrier energy spectrum so that even a small spin splitting of energy bands may result in measurable effects. Spin dependent terms linear in the wavevector k in the effective Hamiltonian remove the spin degeneracy in k -space of the carrier spectrum. In the present case of low dimensional heterostructures and quantum wells, the spatial inversion symmetry is broken. The zero-field spin splitting of electron energy levels in a quantum well can be caused by :

- 1) The lack of inversion symmetry in the host semiconductor bulk crystal potential, in other words, bulk inversion asymmetry (BIA)
- 2) The lack of macroscopic inversion symmetry in the interface confinement potential, in other words, structure inversion asymmetry (SIA)
- 3) Interface inversion asymmetry (IIA) or native interface asymmetry (NIA) may

D.1 Symmetric quantum well

yield k-linear terms caused by non-inversion symmetric bonding of atoms at heterostructure interfaces(104; 105; 106). IIA yields BIA-like terms in the effective Hamiltonian, thus on a phenomenological level a separation between BIA and IIA or NIA is not necessary.

D'yakonov-Perel-Kachorovskii mechanisms for spin relaxation times is built on the first case: bulk inversion asymmetry (107). The spin splitting of the Γ_6 conduction band in a bulk zinc-blende semiconductor has been ascribed to a k^3 contribution in the conduction-band Hamiltonian. When a quantum well is built with this type of semiconductor, the electron wave vector perpendicular to the layer is quantized. In other words, the projection K_{\perp} of the electron momentum along the normal to the plane of the quantum well is much greater than the two-dimensional momentum K_{\parallel} in this plan. An averaging of the spin-orbit splitting along the motion of an electron in the direction perpendicular to the plan of the quantum well has the effect that the splitting of a two-dimensional size-quantized band is proportional to $K_{\perp}K_{\parallel}$. Therefore, in contrast to the three-dimensional case, the splitting is a linear function of the momentum K_{\parallel} . For a given electron energy ϵ the splitting in the two-dimensional case is greater than in three dimensions and the difference is given by a factor of $\hbar^2/ma^2\epsilon \gg 1$, where m is the effective mass. This splitting of the conduction band can be described as the result of action on the electron spin of an effective magnetic field of intensity and direction governed by the magnitude and direction of the momentum. Going over to the two-dimensional case, the zero-field spin splitting of electrons in the conduction band can be described by the Hamiltonian $H_{eff}(k)$ which adds to the isotropic effective-mass Hamiltonian:

$$H_{eff}(k) = \frac{\hbar}{2}\vec{\omega}_{eff}(k) \cdot \vec{\sigma} \tag{D.1}$$

D.1 Symmetric quantum well

The smallness of the spin-orbit term in the Hamiltonian (A.2) makes it possible to obtain an expression for $\vec{\omega}_{eff}$ if we average $\vec{\Omega}$ (see Appendix A) along the motion of an electron in a direction perpendicular to the plan. Therefore the effective magnetic field acting on an electron spin can be written as (107).

$$\langle \chi_x \rangle = \langle k_{\perp}^2 \rangle [2n_x(n_y k_y - n_z k_z) + (n_y^2 - n_z^2)k_x] \quad (D.2)$$

Where \hat{n} is unit vector along the normal to the plan of the quantum well. The quantities $\langle \chi_y \rangle$ and $\langle \chi_z \rangle$ are obtained from Eq. (D.2) by cyclic transposition of the indices. For quasi-2D systems in a quantum well grown in the crystallographic direction [001] the hamiltonian $H_{eff}(k)$ becomes

$$H_{eff}(k) = \beta(\sigma_y k_y - \sigma_x k_x) \quad (D.3)$$

with a material-specific coefficient β . An equation describing spin relaxation can be derived in a manner fully analogous to that used in the three-dimensional case. This equation is

$$\frac{dS_i}{dt} = - \sum_j \Gamma_{ij} S_j \quad (D.4)$$

Where S is the average spin of an electron. The relaxation tensor Γ_{ij} is given by (107)

$$\Gamma_{ij} = \tau_{s0}^{-1}(\epsilon_{ij} Tr B - B_{ij}) \quad (D.5)$$

where τ_{s0} is the spin relaxation time for (100) quantum wells. The symmetric tensor B is a function of n and defined as

$$B_{xx} = (n_y^2 - n_z^2)^2 + 4n_x^2(n_y^2 + n_z^2) - 9n_x^2(n_y^2 - n_z^2) \quad (D.6)$$

$$B_{xy} = -n_x n_y (n_x^2 + n_y^2) - 9n_x n_y (n_y^2 - n_z^2)(n_z^2 - n_x^2) \quad (D.7)$$

Other components are obtained by cyclic transposition of x, y, and z. In the case of nondegenerate the electrons spin relaxation time is given by (107)

$$\frac{1}{\tau_s} = \frac{\alpha^2 \langle k_{\perp}^2 \rangle^2 \tau}{2\hbar^2 m^2 E_g} T \quad (D.8)$$

D.1 Symmetric quantum well

Where τ is the average relaxation time governing the mobility $\mu = e\tau/m$ and T is temperature.

We shall consider the most interesting special cases:

A) Quantum wells grown on (001) substrates:

Substituting $n_x = n_y = 0$ and $n_z = 1$ into Eq. (D.5) leads to

$$\Gamma_{xx} = \Gamma_{yy} = \Gamma_{zz}/2 = \tau_s^{-1} \quad (\text{D.9})$$

Therefore, the relaxation rate of the spin components parallel to the plan of the quantum well is given by the time $\tau_{\parallel} = \tau_s$.

The rate of relaxation perpendicular to the plan of the quantum wells is twice as fast: $\tau_{\perp} = \tau_s/2$. This difference between the relaxation rates is due to the fact that, for a given orientation of the quantum wells, we can see from Eq. (D.3) that $\langle \chi_z \rangle = 0$, i.e., the effective magnetic field varying randomly with time remains parallel to the plan of the quantum well.

B) Quantum wells grown on (111) substrates:

In this case we have $n_x = n_y = n_z = 3^{-1/2}$ and

$$\Gamma_{xx} = \Gamma_{yy} = \Gamma_{zz} = \frac{16}{9\tau_s} \quad \Gamma_{xy} = \Gamma_{xz} = \frac{4}{9\tau_s} \quad (\text{D.10})$$

As in the preceding case, the effective field is in the plane of the quantum well.

C) Quantum wells grown on (110) substrates:

We now have $n_x = n_y = 2^{-1/2}, n_z = 0$

$$\Gamma_{xx} = \Gamma_{yy} = \Gamma_{zz}/2 = -\Gamma_{xy}(8\tau_s)^{-1} \quad \Gamma_{xz} = \Gamma_{yz} = 0 \quad (\text{D.11})$$

Hence, we find that $\tau_{\parallel} = 4\tau_s$ and $\tau_{\perp} = \infty$. Therefore, the spin components perpendicular to the quantum well do not relax. This result is explained by the fact that (as it can be seen from Eq. (D.3)) the effective magnetic field is always parallel to \hat{n} . When the electron momentum changes because of collisions, only

the intensity and sign of this field are affected. In fact, a slow relaxation of the perpendicular component of spins does occur. In other words, spin splitting is absent (small) for quantum wells grown on (110) substrates. Experiments show spin relaxation times in this type of quantum wells, which are more than an order of magnitude longer than that of their (001) counterpart (108; 109). However, Wu *et al* (110) pointed out that this is no longer true when the many-body inhomogeneous broadening effect is taken into account.

D.2 Asymmetric quantum well

In contrast to spin-orbit coupling due to the inversion asymmetry of microscopic crystal potentials, a splitting of conduction band energy levels can also be induced by inversion asymmetry of a macroscopic potential as was pointed out by Rashba (111; 112; 113). The "Rashba effect" has attracted much attention in recent year due to the rapidly developing spintronic dealing with manipulation of spins in electronic devices. One of the problems in the field of spintronic is to build a source of spin-polarized electrons. Several devices based on the Rashba effect have been proposed in the last decade. They start from the pioneering work of Datta and Das (114), who proposed a spin field-effect transistor. Their work is based on a change of the Rashba field in semiconductor heterostructures, caused by structure inversion asymmetry (SIA).

We consider the quantum well grown along the z direction parallel to [001] and choose x and y directions coinciding with crystallographic axes. For an asymmetric quantum well the spin splitting, for electrons in the conduction band, is characterized by the Rashba hamiltonian

$$H_{eff} = \alpha(\sigma_x k_y - \sigma_y k_x) \quad (D.12)$$

D.2 Asymmetric quantum well

Here $\sigma = (\sigma_x, \sigma_y)$ denotes the Pauli spin matrices, α is a material-specific prefactor which is determined by the heterointerface properties (115). It is possible to change the value of α by varying a gate voltage applied to the system or by other changes of the structure symmetry. Using explicit matrix notation for the total Hamiltonian we have

$$H_{total} = H_0 + H_{eff} \begin{pmatrix} H_0 & k_- \\ k_+ & H_0 \end{pmatrix}, \quad (\text{D.13})$$

where $k_{\pm} = k_x \pm ik_y$. The function with the effective spin components ”+” and ”-” because the position of k_{\pm} terms automatically couple. Model spin dephasing calculation based on structure inversion asymmetry were carried out by Pareek and Bruno (116). Calculations of spin relaxation times based on the D’yakonov-Perel mechanism, with structural asymmetry due to doping fluctuations in the hetrostructure interface, were performed by Sherman (117). Interpretation of experimental data based on structure inversion asymmetry is difficult, especially to determine the zero magnetic field spin splitting, which is masked by Zeeman splitting at finite fields. In addition, the splittings are small, typically less than 1 meV.

Appendix E

Hyperfine interaction

The Hamiltonian describing this interaction in the lowest-order relativistic correction was derived by Fermi (118). For S-type electrons (there is no orbital contribution), the interaction between an electronic spin \vec{S} and a nuclear spin \vec{I} is the contact interaction ((119) page 172)

$$H_{cont} = \frac{16\pi}{3} \mu_B \sum_j \frac{\mu_j}{I_j} (\vec{S} \cdot \vec{I}_j) \delta(\vec{r} - \vec{R}_j), \quad (\text{E.1})$$

Where μ_B is the Bohr magneton, \vec{S} and \vec{r} are the spin and position of the electron, μ_j , \vec{I}_j and \vec{R}_j are the magnetic moment, spin, and position of the j th nucleus, and the sum runs over all the nuclei in the lattice. For localized electrons the distance between their energy levels is much larger than the energy of the hyperfine interaction with the nuclei. As a result this spin-spin interaction can be described in the lowest order by the Hamiltonian

$$H_{hyf} = \frac{V_0}{2} \sum_j A^j |\psi(\vec{R}_j)|^2 (I_x^j \sigma_x + I_y^j \sigma_y + I_z^j \sigma_z), \quad (\text{E.2})$$

Here V_0 is the volume of the unit cell, $\psi(\vec{R}_j)$ is the electron envelope wave function at the j th nucleus, I_α and σ_α are the spin projections on the coordinate axes,

and $A^j = 16\pi\mu_B\mu_j/3I^j |u_c(\vec{R}_j)|^2$, where $u_c(\vec{R}_j)$ is the electron Bloch function at the nucleus. One can neglect the interaction of holes with the nuclei because the hole Bloch function vanishes at the positions of the nuclei. In addition, one can neglect the nuclear dipole-dipole interaction, which does not conserve the total spin of the electron-nuclear system. They become important only at times longer than 10^{-4} s (120).

The effective nuclear hyperfine magnetic field B_N , acting on a localized electron spin can be obtained from Eq. (E.2) taking the expectation value of the Hamiltonian H_{hyf} over the ensemble of nuclear wave functions. It is the sum of contributions from a large number of nuclei

$$B_N = \frac{V_0}{\mu_B g_e} \langle \sum_j A^j |\psi(\vec{R}_j)|^2 I^j \rangle_N, \quad (\text{E.3})$$

where $\langle \dots \rangle_N$ denotes a quantum mechanical average over the ensemble of nuclear wave functions and g_e is the electron g factor. The magnitude and direction of this field are randomly distributed.

The electronic relaxation time due to this interaction has been calculated in the case of metals (Fermi statistics), and we give here a description valid for non-degenerate semiconductors where Boltzmann statistics can be applied. Ensemble spin dephasing due to the hyperfine interaction mechanism in an external magnetic field has been studied by D'yakonov and Perel (121). Recently, calculations of spin relaxation time using this mechanism were performed for electron spins in quantum dots (120; 122). Spin relaxation processes due to phonon-assisted hyperfine interactions were investigated in GaAs quantum dots (123; 124; 125).

Bibliography

- [1] D. D. Awschalom, D. Loss, and N. Samarth, editors. *Semiconductor Spintronics and Quantum Computation*. Springer, Berlin, 2002. [1](#), [2.10](#), [B](#)
- [2] I. Žutić, J. Fabian, and S. Das Sarma. *Rev. Mod. Phys*, 76:323, 2004. [1](#), [2.10](#)
- [3] J F Gregg, I Petej, E Jouguelet, and C Dennis. *J. Phys. D: Appl. Phys*, 35:R121–R155, 2002. [1](#)
- [4] A. Steane. *Rep. Prog. Phys*, 61:117, 1998. [1](#)
- [5] M. Z. Maialle, E. A. de Andrada e Silva, and L. J. Sham. *Phys. Rev. B*, 47:15776, 1993. [1](#), [2.8.1](#), [6.1](#), [6.3](#)
- [6] K. Reimann and St. Rübenacke. *Phys. Rev. B*, 49:11021, 1994. [2.1](#), [2.2](#)
- [7] A. Goldmann. *Phys. Status Solidi (b)*, 81:9, 1977. [2.1](#)
- [8] W. Staude. *Phys. Status Solidi (b)*, 43:367, 1971. [2.1](#)
- [9] M. Cardona. *Phys. Rev*, 129:69, 1963. [2.1](#), [2.2](#)
- [10] J. F. Koster, J.O. Dimmock, R. G. Wheeler, and H. Statz. *Properties of the Thirty-two Point Groups*. MIT Press, Cambridge, Mass, 1963. [2.2](#), [2.2](#)

- [11] T. H. K. Barron, J. A. Birch, and G. K. White. *J. Phys. C*, 10:1617, 1977. [2.2](#)
- [12] R. Kleim F. Raga, A. Mysyrowicz, J. B. Grun, and S. Nikitine. *J. Phys. (Paris) Colloq*, 28:C3–116, 1967. [2.2](#)
- [13] A. Göbel, T. Ruf, Ch. T. Lin, M. Cardona, J-C. Merle, and M. Joucla. *Phys. Rev. B*, 56:210, 1997. [2.2](#), [4.5](#)
- [14] J. C. Phillips. *Rev. Mod. Phys*, 42:317, 1970. [2.2](#)
- [15] B. Hönerlage, R. Lévy, J. B. Grun, C. Klingshirn, and K. Bohnert. *Phys. Rep*, 124:161–253, 1985. [2.2](#), [5.2](#), [5.2](#)
- [16] R. Ranvaud, H. R. Trebin, U. Rössler, and F. H. Pollak. *Phys. Rev. B*, 20:701, 1979. [2.2](#)
- [17] B. Hönerlage, A. Bivas, and Vu Duy. Phach. *Phys. Rev. Lett*, 41:49, 1978. [2.2](#)
- [18] E.I. Rashba and M. D. Sturge, editors. *Excitons*, volume 2 of *Modern Problems in Condensed Matter Sciences*. North-Holland, Amsterdam, 1982. [2.3](#)
- [19] L. C. Andreani and F. Bassani. *Phys. Rev. B*, 41:7536, 1990. [2.3.1](#)
- [20] E. Hanamura. *Phys. Rev. B*, 38:1228, 1988. [2.3.1](#)
- [21] L. C. Andreani, F. Tassone, and F. Bassani. *Solid State Commun.*, 77:641, 1991. [2.3.1](#)
- [22] D. S. Citrin. *Solid State Commun.*, 84:281, 1992. [2.3.1](#)

BIBLIOGRAPHY

- [23] A. Göbel, T. Ruf, Ch. T. Lin, M. Cardona, J-C. Merle, and M. Joucla. *Phys. Rev. B*, 56:210, 1997. [2.4.2](#), [3.5](#)
- [24] D. J. Thomas. *J. Appl. Phys*, 32:2298, 1961. [2.5](#)
- [25] A. Twardowski, Rokita F, and A. J. Gaj. *Solid State Commun.*, 36:927, 1980. [2.5](#)
- [26] R. André. *Effet piézo-électrique dans les puits quantiques CdTe-CdMnTe et CdTe-CdZnTe*. PhD thesis, Université Joseph Fourier-Gronoble 1, 1994. [2.9](#), [2.7](#), [6.1](#)
- [27] G. Fishman. *Phys. Rev. B*, 52:11132, 1995. [2.7](#), [2.7](#)
- [28] E. Pikus and G. L. Bir. *Sov. Phys. Solid State*, 1:1502, 1960. [2.7](#)
- [29] E. Pikus and G. L. Bir. *Symmetry and Strain Induced Effects in Semiconductors*. Wiley, New York, 1974. [2.7](#), [5.1](#)
- [30] H. Hasegawa. *Phys. Rev*, 129:1029, 1963. [2.7](#)
- [31] H. Pollak and M. Cardona. *Phys. Rev. B*, 172:816, 1968. [2.7](#)
- [32] J. M. Luttinger. *Phys. Rev*, 102:1030, 1956. [2.7](#)
- [33] D. L. Smith. *Solid State Commun.*, 57:919, 1986. [2.8](#)
- [34] E. A. Caridi, T. Y. Chang, K. W. Goosen, and L. F. Eastman. *Appl. Phys. Lett*, 56:659, 1990. [2.8](#)
- [35] C. Mailhot and D. L. Smith. *Phys. Rev. B*, 35:1242, 1987. [2.8](#)
- [36] C. Mailhot and D. L. Smith. *Phys. Rev. B*, 37:10415, 1988. [2.8](#)

BIBLIOGRAPHY

- [37] C. Mailhot and D. L. Smith. *Solid State Commun.*, 66:859, 1988. 2.8
- [38] M. Ilg, Klaus H. Ploog, and A. Trampert. *Phys. Rev. B*, 50:17111, 1994. 2.10
- [39] I. Sela, D. E. Watkins, B. K. Laurich, D. L. Smith, S. Subbanna, and H. Kroemer. *Appl. Phys. Lett*, 58:684, 1991. 2.8, 6.2.1
- [40] G. Duggan, K. J. Moore, A. Raukema, G. T. Jaarsma, and K. Woodbridge. *Phys. Rev. B*, 45:4494, 1992. 2.8
- [41] T. S. Moise, L. J. Guido, R. C. Barker, J. O. White, and A. R. Kost. *Appl. Phys. Lett*, 60:2637, 1992. 2.8
- [42] W. F. Cady. *Piezoelectricity*. McGraw-Hill, New York, 1946. 2.8, 2.8
- [43] A. Vinattieri, J. Shah, T. C. Damen, K. W. Goossen, L. N. Pfeiffer, M. Z. Maialle, and L. J. Sham. *Appl. Phys. Lett*, 63:3194, 1993. 2.8.1, 6.3
- [44] M. Julier, A. Vinattieri, M. Colocci, P. Lefebvre, B. Gil, D. Scalbert, C. A. Tran, Jr. R. F. Karlicek, and J.-P. Lascaray. *Phys. stat. sol. (b)*, 216:341, 1999. 2.8.1, 6.3
- [45] D. A. B. Miller, D. S. Chemla, T. C. Damen, A. C. Gossard, W. Wiegmann, T. H. Wood, and C. A. Burrus. *Phys. Rev. Lett*, 53:2173, 1984. 2.8.1
- [46] D. A. B. Miller, D. S. Chemla, T. C. Damen, A. C. Gossard, W. Wiegmann, T. H. Wood, and C. A. Burrus. *Phys. Rev. B*, 32:1043, 1985. 2.8.1
- [47] B. Meier and B. P. Zachachrenya, editors. *Optical Orientation*. North-Holland, Amsterdam, 1984. 2.9, A, A, C
- [48] M. I. D'yakonov. *cond-mat*, page 0401369, 2004. 2.9

BIBLIOGRAPHY

- [49] J. Fabian and S. Das Sarma. *J. Vac. Sci. Technol. B*, 17(4):1708, 1999. [2.9](#)
- [50] G. Fishman and G. Lampel. *Phys. Rev. B*, 16:820, 1977. [2.10](#), [6.1](#), [B](#)
- [51] M. I. D'yakonov and V. I. Perel. *Sov. Phys. JETP*, 33:1053, 1971. [2.11](#), [A](#),
[A](#)
- [52] R. J. Elliott. *Phys. Rev.*, 96:266, 1954. [2.11](#), [B](#)
- [53] J. N. Chazalviel. *Phys. Rev. B*, 11:1555, 1975. [2.11](#), [B](#)
- [54] F. Seitz and D. Turbull, editors. *Solid State Physics*, volume 14. Academic Press, New York, 1963. [2.11](#), [B](#)
- [55] G. L. Bir, A. G. Aronov, and G. E. Pikus. *Sov. Phys. JETP*, 42:705, 1976. [2.11](#), [C](#)
- [56] G. Bastard and L. L. Chang. *Phys. Rev. B*, 41:7899, 1991. [2.11.1](#)
- [57] N. Linder and L. J. Sham. *Physica E*, 2:412, 1998. [2.11.1](#), [2.11.1](#)
- [58] C. Camilleri, F. Teppe, D. Scalbert, Y. G. Semenov, M. Nawrocki, M. Dyakonov, J. Cibert, S. Tatarenko, and T. Wojtowicz. *Phys. Rev. B*, 46:085331, 2001. [2.11.1](#)
- [59] S. H. Cho, F. X. Kärtner, U. Morgner, E. P. Ippen, J. G. Fujimoto, J.E. Cunningham, and W. H. Knox. *Opt. Lett.*, 26:560, 2001. [3.1](#), [3.2.2](#)
- [60] H. Rahimpour Soleimani, S. Cronenberger, O. Crègut, J.-P. Likforman, M. Gallart, T. Ostatnický, P. Gilliot, and B. Hönerlage. *Appl. Phys. Lett.*, 85:5263, 2004. [3.5](#), [4.1](#), [4.1](#), [4.3.1](#), [4.3.1](#)

- [61] J. Cibert, R. André, C. Deshayes, Le Si Dang, H. Okumura, S. Tatarenko, G. Feuillet, P. H. Jouneau, R. Mallard, and K. Saminadaya. *J. Cryst. Growth*, 117:424, 1992. [3.6](#)
- [62] S. Bar-Ad and I. Bar-Joseph. *Phys. Rev. Lett*, 68:349, 1992. [4.1](#), [6.1](#), [6.3](#)
- [63] A. Tackeuchi, Y. Nishikawa, and O. Wada. *Appl. Phys. Lett*, 68:797, 1996. [4.1](#), [6.1](#), [6.3](#)
- [64] T F. Boggess, J. T. Olesberg, C. Yu, M. E. Flatt, and W. H. Lau. *Appl. Phys. Lett*, 77:1333, 2000. [4.1](#)
- [65] J. J. A. Gupta, D. D. Awschalom, Al. L. Efros, and A. V. Rodina. *Phys. Rev. B*, 66:125307, 2002. [4.1](#)
- [66] B. Beschoten, E. Johnston-Halperin, D. K. Young, M. Poggio, J. E. Grimaldi, S. Keller, U. K. Mishra S. P. DenBaars, E. L. Hu, and D. D. Awschalom. *Phys. Rev. B*, 63:121202, 2001. [4.1](#)
- [67] A. Vinatieri, J. Shah, T. C. Damen, D. S. Kim, L. N. Pfeiffer, M. Z. Maialle, and L. J. Sham. *Phys. Rev. B*, 50:10868, 1994. [4.1](#)
- [68] E. Vanelle, M. Paillard, X. Marie, T. Amand, P. Gilliot, D. Brinkmann, R. Lévy, J. Cibert, and S. Tatarenko. *Phys. Rev. B*, 62:2696, 2000. [4.1](#), [6.1](#), [6.3](#)
- [69] S. Cortez, O. Krebs, S. Laurent, M. Senes, X. Marie, P. Voisin, R. Ferreira, G. Bastard, J-M. Gérard, and T. Amand. *Phys. Rev. Lett*, 89:207401, 2002. [4.1](#)
- [70] Y. Masumoto, Y. Unuma, Y. Tanaka, and S. Shionoya. *J. Phys. Soc. Japan*, 47:1844, 1979. [4.2.1](#)

- [71] H. Rahimpour Soleimani, S. Cronenberger, O. Crègut, J.-P. Likforman, M. Gallart, T. Ostatnický, P. Gilliot, and B. Hönerlage. *E-MRS 2004 Spring Meeting, Strasbourg (24-28 mai 2004), to be published in Applied Surface Science*, 2005. [4.3.1](#), [4.4](#), [4.4.1](#)
- [72] R. Lévy, B. Hönerlage, and J. B. Grun. *Phys. Rev. B*, 19:2326, 1979. [4.4.1](#), [4.5](#)
- [73] R. Lévy, B. Hönerlage, and J. B. Grun. *Solid State Commun.*, 29:103, 1979. [4.4.1](#)
- [74] M. J. M. Gomes, R. Lévy, and B. Hönerlage. *J. Lumin*, 48-49:83, 1991. [4.4.1](#), [5.3](#)
- [75] S. Cronenberger, H. Rahimpour Soleimani, T. Ostatnický, O. Crègut, M. Gallart, P. Gilliot, and B. Hönerlage. *Submitted to Phys. Rev. B*. [4.4.1](#), [4.5](#), [4.6](#)
- [76] R. S. Knox, S. Nikitine, and A. Mysyrowicz. *Optics Commun.*, 1:19, 1969. [4.5](#)
- [77] R. Lévy and J. B. Grun. *Phys. Status Solidi (a)*, 22:11, 1974. [4.6](#)
- [78] M. Certier, C. Wecker, and S. Nikitine. *J. Phys. Chem. Sol*, 30:1281, 1969. [4.6](#)
- [79] H. Rahimpour Soleimani, T. Ostatnický, S. Cronenberger, M. Gallart, P. Gilliot, and B. Hönerlage. *Submitted to Phys. Rev. B*. [5.1](#), [5.3](#), [5.3](#), [5.3](#), [5.3](#), [5.4](#)
- [80] K. Cho. *Phys. Rev. B*, 14:4463, 1976. [5.1](#), [5.2](#)

BIBLIOGRAPHY

- [81] T. Mita, K. Satomé, and M. Ueta. *Solid State Commun.*, 33:1135, 1980. [5.3](#), [5.4](#)
- [82] D.J. Hilton and C.L. Tang. *Phys. Rev. Lett*, 89:146601, 2002. [6.1](#)
- [83] R. Akimoto, K. Ando, F. Sasaki, S. Kobayashi, and T. Tani. *Phys. Rev. B*, 56:9726, 1997. [6.1](#), [6.3](#), [6.3](#)
- [84] A. P. Heberle, W. W. Rühle, and K. Ploog. *Phys. Rev. Lett*, 72:3887, 1994. [6.1](#)
- [85] J. M. Kikkawa and D. D. Awschalom. *Phys. Rev. Lett*, 80:4313, 1998. [6.1](#)
- [86] R. Ferreira and G. Bastard. *Phys. Rev. B*, 43:9687, 1991. [6.1](#), [6.3](#)
- [87] H. Rahimpour Soleimani, S. Cronenberger, M. Gallart, P. Gilliot, J. Cibert, O. Crègut, B. Hönerlage, and J.-P. Likforman. *Submitted to Appl. Phys. Lett.* [6.1](#), [6.3](#), [6.3](#), [6.3](#)
- [88] S. Schmitt-Rink, D. S. Chemla, and D. A. B. Miller. *Phys. Rev. B*, 32:6601, 1985. [6.2](#), [6.3](#)
- [89] M. Combescot and R. Combescot. *Phys. Rev. Lett*, 61:117, 1988. [6.2.2](#)
- [90] N. Peyghambarian, H. M. Gibbs, J. L. Jewell, A. Antonetti, A. Migus, D. Hulin, and A. Mysyrowicz. *Phys. Rev. Lett*, 53:2433, 1984. [6.3](#)
- [91] P. Plochocka, P. Kossacki, W. Maslana, J. Cibert, S. Tatarenko, C. Radzewicz, and J. Gaj. *Phys. Rev. Lett*, 92:177402, 2004. [6.3](#)
- [92] G. Bastard and R. Ferreira. *Surface Science*, 267:335, 1992. [6.3](#)

BIBLIOGRAPHY

- [93] Y. Kato, R. C. Myers, A. C. Gossard, and D. D. Awschalom. *Nature*, 427:50, 2004. [7](#)
- [94] C. Kittel. *Quantum Theory of Solids*. Wiley, New York, 1963. [A](#)
- [95] O. Madelung. *Introduction to Solid-State Theory*. Springer series in Solid-State Sciences 2, 1981. [A](#)
- [96] G. Dresselhaus. *Phys. Rev*, 100:580, 1955. [A](#), [A](#)
- [97] R. H. Parmenter. *Phys. Rev*, 100:573, 1955. [A](#)
- [98] E. O. Kane. *J. Phys. Chem. Solids*, 1:249, 1957. [A](#)
- [99] J.-N. Chazalviel. *Phys. Rev. B*, 11:1555, 1975. [B](#)
- [100] P. Boguslawski. *Solid State Commun.*, 33:389, 1980. [B](#)
- [101] A. Dyson and B. K. Ridley. *Phys. Rev. B*, 69:125211, 2004. [B](#)
- [102] W. Zawadzki and W. Szymanska. *Phys. Status Solidi B*, 45:415, 1971. [B](#)
- [103] P. H. Song and K. W. Kim. *Phys. Rev. B*, 66:035207, 2002. [C](#)
- [104] S. Cortez, O. Krebs, and P. Voisin. *J. Vac. Sci. Technol. B*, 18:2232, 2000. [D.1](#)
- [105] U. Rössler and J. Kainz. *Solid State Commun.*, 121:313, 2002. [D.1](#)
- [106] L. E. Golub. *Phys. Rev. B*, 67:235320, 2003. [D.1](#)
- [107] M. I. D'yakonov and V.Y. Kachorovskii. *Sov. Phys. Semicond*, 20:110, 1986. [D.1](#), [D.1](#), [D.1](#), [D.1](#)

BIBLIOGRAPHY

- [108] Y. Ohno, R. Terauchi, T. Adachi, F. Matsukura, and N. Ohno. *Phys. Rev. Lett*, 83:1986, 1975. [D.1](#)
- [109] M. Henini, O. Z. Karimov, G. H. John, R. T. Harley, and R. J. Airey. *Physica E: Low-dimensional Systems and Nanostructures*, 23:309, 2004. [D.1](#)
- [110] M. W. Wu and M. Kuwata-Gonokami. *Solid State Commun.*, 121:509, 2002. [D.1](#)
- [111] Yu. A. Bychkov and E. I. Rashba. *JETP Lett*, 39:78, 1984. [D.2](#)
- [112] E.I. Rashba. *Sov. Phys. Solid State*, 2:1109, 1960. [D.2](#)
- [113] Yu. A. Bychkov and E. I. Rashba. *J. Phys. C*, 17:6039, 1984. [D.2](#)
- [114] S. Datta and B. Das. *Appl. Phys. Lett*, 56:665, 1990. [D.2](#)
- [115] G. Lommer, F. Malcher, and U. Rössler. *Phys. Rev. B*, 32:6965, 1985. [D.2](#)
- [116] T. P. Pareek and P. Brun. *Phys. Rev. B*, 65:241305, 2001. [D.2](#)
- [117] E. Ya. Shermana. *Appl. Phys. Lett*, 82:209, 2003. [D.2](#)
- [118] E. Fermi. *Z. Phys*, 60:320, 1930. [E](#)
- [119] A. Abragam. *Principles of Nuclear Magnetism*. Clarendon Press. Oxford, 1996. [E](#)
- [120] I.A. Merkulov. *Phys. Rev. B*, 65:205309, 2002. [E](#), [E](#)
- [121] M. I. D'yakonov and V. I. Perel. *Sov. Phys. JETP*, 38:177, 1973. [E](#)
- [122] Y. G. Semenov and K. W. Kim. *Phys. Rev. B*, 67:073301, 2003. [E](#)

BIBLIOGRAPHY

- [123] S. I. Erlingsson, Y. V. Nazarov, and V. I. Fal'ko. *Phys. Rev. B*, 64:195306, 2001. [E](#)
- [124] S. I. Erlingsson, Y. V. Nazarov, and Vladimir I. Fal'ko. *Physica E*, 12:823, 2002. [E](#)
- [125] S. I. Erlingsson and Y. V. Nazarov. *Phys. Rev. B*, 70:205327, 2004. [E](#)